

**The Effect of Degassing of H₂O on Crystallization and Oxidation in Highly-Evolved
Magmas: Implications for the Origins of Rhyolite Liquids**

by

Laura E. Waters

A dissertation submitted in partial fulfillment
of the requirements for the degree of
Doctor of Philosophy
(Geology)
in the University of Michigan
2013

Doctoral Committee:

Professor Rebecca Ann Lange, Chair
Research Scientist Gordon Moore
Professor Sally Oey
Associate Professor Adam Charles Simon
Professor Youxue Zhang

© Laura Elizabeth Waters
2013

ACKNOWLEDGMENTS

I would like to sincerely thank my advisor, Rebecca Lange, for her mentorship and guidance, which have helped me view igneous geochemistry on a variety of scales, from the effect of H₂O on activities of melt components to the tectonic scale. I am deeply appreciative of her continuous financial support and numerous opportunities that I received to present my research. I would also like to extend my gratitude to Benjamin Andrews for his collaboration in research, for his willingness to teach the experimental techniques required for phase equilibrium and decompression experiments, and for his help with gaining access to facilities at the National Museum of Natural History. I would like to thank Gordon Moore for his instruction on the use of piston cylinders at Arizona State University, for his help with the electron microprobe in EMAL at the University of Michigan, and for frequent, thorough discussions of CO₂ and H₂O solubility in the melt and vapor phases in large volumes of rhyolite liquids. Thanks to my committee, Youxue Zhang, Adam Simon, and Sally Oey, for providing me with hours of their time for discussion of my work. I also owe a second thanks to Carl Henderson, Leslie Hayden and Yang Chen, for their assistance and expertise with the Electron Microprobe Analyzer.

Thanks to Tom Hudgins for many open discussions, which challenged my scientific arguments and perspectives, and ultimately bolstered my understanding of the fundamentals of geochemistry; to Nathan Sheldon, who first introduced me to Benjamin Andrews, and who has provided me with extensive advice regarding pathways for careers

and funding in academia; to the past and current members of my research group members and cohort of 2008 for their support and encouragement in my success in my degree: Stephen, Mary Catherine, Xuan, Xiaofei, Marissa, Sean, James, Meghan, Jen, Nora, Louise, Steph, Rohit, Karthik; to the staff in the main office, who have made funding possible, facilitated overrides, reimbursements, and stipends: Anne, Stacy, Brandi, Nancy, Julie, Brenda.

A very special thanks to my father, mother, brothers, Paige Walker, John Naliboff, and Amy Ruddle for being available every moment of every year with unending support. I am especially grateful to the founding members of the Bird Watching Club of the Department of Earth and Environmental Science; to my roommates throughout the years (Lydia, Jen, Ethan, Mark); to my running partners; and to the wonderful group of friends I have made while at Michigan for their camaraderie and emotional and mental support.

TABLE OF CONTENTS

ACKNOWLEDGMENTS.....ii

LIST OF TABLES.....vi

LIST OF FIGURES.....viii

LIST OF APPENDICES.....xiii

CHAPTER I INTRODUCTION..... 1

CHAPTER II CRYSTAL-POOR, MULTIPLY SATURATED RHYOLITES (OBSIDIANS) FROM THE CASCADE AND MEXICAN ARCS: EVIDENCE OF DEGASSING-INDUCED CRYSTALLIZATION OF PHENOCRYSTS..... 19

2.1 ABSTRACT19

2.2 INTRODUCTION.....20

2.3 GEOLOGIC SETTING.....22

2.4 WHOLE ROCK GEOCHEMISTRY AND PETROGRAPHY.....23

2.5 MINERAL COMPOSITIONS.....26

2.6 TESTS TO DISTINGUISH PHENOCRYSTS VS. XENOCRYSTS.....37

2.7 BSE IMAGES OF XENOCRYSTS VS PHENOCRYSTS..... 43

2.8 DEGASSING-INDUCED CRYSTALLIZATION OF PHENOCRYSTS?.....49

2.9 CONCLUSIONS.....64

2.10 REFERENCES.....66

CHAPTER III NO EFFECT OF DEGASSING OF H₂O ON THE FE³⁺/FE²⁺ OF RHYOLITE OBSIDIANS 73

3.1 ABSTRACT.....73

3.2 INTRODUCTION.....74

3.3 SAMPLE DESCRIPTION.....77

3.4 METHODOLOGY77

3.5 RESULTS.....81

3.6 DISCUSSION: PRE-ERUPTIVE V. POST-ERUPTIVE Fe^{2+}	84
3.7 CONCLUSIONS.....	88
3.8 REFERENCES.....	88

CHAPTER IV DEGASSING INDUCED CRYSTALLIATION OF PLAGIOCLASE IN RHYOLITE AND RHYODACITE OBSIDIANS: PHASE EQUILIBRIUM AND DECOMPRESSION EXPERIMENTS.....93

4.1 ABSTRACT.....	93
4.2 INTRODUCTION.....	94
4.3 EXPERIMENTAL METHODS.....	99
4.4 RESULTS.....	106
4.5 DISCUSSION.....	119
4.6 CONCLUSIONS.....	136
4.7 REFERENCES.....	137

CHAPTER V RECALIBRATION OF THE PLAGIOCLASE-LIQUID HYGROMETER FOR RHYOLITES.....142

5.1 ABSTRACT.....	142
5.2 INTRODUCTION.....	143
5.3 PLAGIOCLASE-LIQUID EQUILIBRIUM DATA.....	149
5.4 RESULTS OF THE HYGROMETER REGRESSION.....	152
5.5 APPLICATION OF THE HYGROMETER TO NATURAL RHYOLITES.....	155
5.6 CONCLUSIONS.....	160
5.7 REFERENCES.....	161

CHAPTER VI CONCLUSIONS.....167

APPENDICES.....171

LIST OF TABLES

CHAPTER II

Table 2.1 Whole-rock major element compositions and point counts.....	24
Table 2.2 Average Compositions of Fe-Ti Oxides.....	28
Table 2.3 Analyses of Minimum and Maximum % An Plagioclase.....	29
Table 2.4 Analyses of minimum and maximum Mg-number orthopyroxene.....	32
Table 2.5 Sr and Ba analyses in plagioclase.....	35

CHAPTER III

Table 3.1 Whole-rock major element compositions.....	78
Table 3.2 Average Fe-Ti oxide compositions.....	82
Table 3.3 Measurements of wt% FeO and Δ NNO by different techniques.....	83
Table 3.4 Free energy of hydration reactions.....	87

CHAPTER IV

Table 4.1 Bulk Compositions.....	97
Table 4.2 Phase equilibrium experiments: Run conditions and products.....	101
Table 4.3 MLV36 Decompression Experiments: Run Conditions and Products.....	104
Table 4.4 Phase Equilibrium Experiments Glass Compositions.....	107
Table 4.5 Phase Equilibrium Experiments Plagioclase Compositions.....	108
Table 4.6 MLV36 Decompression Experiment Glass and Plagioclase Compositions ..	116

CHAPTER V

Table 5.1 Summary of albite (a) and anorthite (b) thermodynamic data used in the hygrometer model.....	148
Table 5.2 Model Parameters.....	153

APPENDIX A

Table A1 Whole rock trace element concentrations.....	171
Table A2 Titanomagnetite Compositions.....	172
Table A3 Ilmenite Compositions	173
Table A4 Plagioclase Compositions	175
Table A5 Orthopyroxene Compositions.....	235
Table A6 Sr and Ba Partitioning.....	250
Table A7 Plagioclase Major and Trace Element Data.....	253
Table A8 Calibration of Rhyolite Hygrometer (Lange et al., 2012).....	255
Table A9 Free energy of hydration reactions.....	256

APPENDIX B

Table B1 S contents in rhyolite groundmass.....	264
Table B2 Recalibration of the plagioclase hygrometer by Lange et al. (2012).....	265
Table B3 Cl contents in apatites and groundmass and Cl solubility estimates in rhyolites using Webster and De'vivo (2002).....	266

APPENDIX C

Table C1 MLV44 Plagioclase Analyses.....	271
Table C2 MLV44 Ilmenite and Titanomagnetite Analyses.....	272
Table C3 FTIR Analyses of selected hydrous glasses.....	273
Table C4 Experimental Glass Analyses.....	274
Table C5 Experimental Plagioclase Analyses.....	297
Table C6 Experimental Orthopyroxene Analyses.....	303
Table C7 Experimental Clinopyroxene Analyses.....	304
Table C8 Plagioclase Analyses from Decompression Experiments.....	307
Table C9 Glass Analyses from the Decompression Experiments.....	309

APPENDIX D

Table D1 Plagioclase and liquid compositions used to calibrate the rhyolite hygrometer.....	313
--	-----

LIST OF FIGURES

CHAPTER II

- Figure 2.1** Crossed polar photomicrographs (shown on the left) and corresponding aluminum element maps of groundmass (shown on the right) for JAL-10, TEQ-21 and COMP-3. The area of the aluminum element map is shown in the photomicrograph as a white box..... 26
- Figure 2.2** Plots of plagioclase length (long axis) by range in mol% An for all measured grains in each rhyolite.....30
- Figure 2.3** Histograms of plagioclase phenocrysts (in grey), microlites (in black), and possible xenocrysts (in hatched pattern) as a function of mol% An.....31
- Figure 2.4** Histograms of orthopyroxene phenocryst (grey) compositions, as a function of Mg# with corresponding $^{Fe-Mg}K_D$ values between orthopyroxene and liquid33
- Figure 2.5** A plot of analyzed plagioclase compositions (mol% An) in the six obsidian samples as a function of the An# of the liquid (defined in Table 2.1) with a range of possible xenocrysts shown as a dashed grey line (see text for criteria for distinguishing xenocrysts) with phase equilibrium experiments from the literature.....38
- Figure 2.6** A plot of the range of $^{Fe-Mg}K_D$ values between orthopyroxene and liquid for the six obsidian samples with $^{Fe-Mg}K_D$ values between orthopyroxene and liquid from experiments where the oxygen fugacity was controlled or known.....40
- Figure 2.7** (A) Plot of $RT \ln D_{Ba}$ vs An (mol%) and (B) Plot of $RT \ln D_{Sr}$ vs An (mol%), where temperatures are those obtained from Fe-Ti oxides and D_{Ba} and D_{Sr} values are those calculated using the ppm Ba and Sr in plagioclase with the changing liquid Ba and Sr concentrations modeled by fractional crystallization.....42
- Figure 2.8** BSE images of plagioclase and orthopyroxene crystals (A-F) in MLV-37.....47
- Figure 2.9** BSE images of plagioclase and orthopyroxene crystals (A-D) in MLV-45.....48
- Figure 2.10** Schematic plot of the plagioclase binary loop projected from a magmatic liquid.....49

Figure 2.11 Phase diagram for H₂O fluid-saturated, low-K rhyolite from the experiments of Tomiya et al. (2010) and superimposed is an ascent path for rhyolite MLV-45 at the temperature obtained by two Fe-Ti oxide thermometry. The ascent path is modeled as adiabatic (rapid transport along a fracture), $(dT/dP)_S = TVa/C_p$, where T is temperature in Kelvin, V is molar volume, a is the coefficient of thermal expansion (calculated from Lange, 1997 and Ochs and Lange, 1999) and C_p is the molar heat capacity (calculated from Lange and Navrotsky, 1993, with partial molar C_p of the H₂O component from Spera, 2000).....53

Figure 2.12 Schematic fluid-saturated plagioclase liquidus curve on a pressure v. temperature plot. After an ascending magma crosses the plagioclase-in curve, it passes through three zones, where ΔT (=temperature of plagioclase liquidus- temperature of magma) progressively increases. (B) Schematic plot of crystal growth rate and nucleation rate with degree of under cooling (ΔT); modified from the experiments of Meiling and Uhlmann (1967).....55

Figure 2.13 (A) A multistep (MD) decompression path for experiment 236 of Couch et al. (2003b) is shown as a dashed line at a constant temperature of 875°C. Melt viscosities (\log_{10} Pa s) are shown beneath the decompression path in italicized font and are calculated with the water solubility model of Liu et al. (2005) and the viscosity model of Zhang and Hui (2007) and the equilibrium plagioclase composition reported by Couch et al. (2003a, b). The mean plagioclase composition grown in experiment 236 is shown above the decompression path with a hollow circle, along with a 1 σ (solid black line) and ~2 σ (dashed line) standard deviation. Experiment 236 ceased nucleation and growth at ~An44-An47, which corresponds to melt viscosities of 4.88-5.35 \log_{10} Pa s. (B) A schematic plot of nucleation and growth curves as a function of undercooling (ΔT) is drawn based on rates observed in the experiments of Couch et al. (2003b) (and shown as Figure 15 in Couch et al., 2003b).....58

Figure 2.14 A plot of melt viscosity during plagioclase growth for each sample as a function of wt% SiO₂.....60

Figure 2.15 A plot of wt% H₂O and ^{Fe-Mg}K_D values between orthopyroxene and liquid for water-saturated phase equilibrium experiments on Mg-rich andesite (a) (Grove et al. 2003), (b) dacite (Gardner et al. 1995), (c) rhyolite (Tomiya et al. 2010 and Coombs and Gardner 2001) and (d) high-Mg basalt (Gaetani and Grove 1998). The effect of dissolved water on the ^{Fe-Mg}K_D values is greater in more evolved liquids (i.e., lower MgO).....62

CHAPTER III

Figure 3.1 A plot of pre-eruptive wt% FeO (derived from Fe-Ti oxides and the geothermometer/ barometer of Ghiorso & Evans 2008) and post-eruptive wt% FeO (from titrations; Wilson 1960) with a 1:1 correspondence line.....85

CHAPTER IV

- Figure 4.1** Photomicrographs of the three obsidians illustrate the phenocryst-poor glassy nature of the obsidians with little to no microlite crystallization.....97
- Figure 4.2** The range of plagioclase observed in the natural samples as a function of mol% An v. number of analyses from microprobe analyses for MLV44 (a), MLV36 (b), and TEQ34 (c).....99
- Figure 4.3** Plots of liquid An-number vs. time (a) and mol% An vs. time (b) as a test of equilibrium.....102
- Figure 4.4** Phase equilibrium diagram for TEQ-34.....111
- Figure 4.5** Phase equilibrium diagram for MLV-36.....112
- Figure 4.6** Phase equilibrium diagram for MLV-44.....114
- Figure 4.7** Scanning electron microscope (SEM) and element maps for BSE imaging standard (a) MLV36 isothermal (850°C) decompression experiment from 150 to 89 MPa (c-d) and from 150 to 58 MPa (d-e) at 0.8 MPa/hr118
- Figure 4.8** Panels a-d show the effects of degassing on crystal nucleation and growth.....126
- Figure 4.9** The high pressure decompression experiments of Martel & Schmidt (2003) are shown as a function of pressure (MPa) v. time (hours) and viscosity (\log_{10} Pa s) v. time (hours).....132
- Figure 4.10** The experiments of Martel & Schmidt (2003) that correspond to the suppression of plagioclase nucleation and growth (outlined in black in Fig. 10) are shown as a function of their experimental viscosity (\log_{10} Pa s) and the rate of change of viscosity (\log_{10} Pa s/hr).....135

CHAPTER V

- Figure 5.1** Two histogram of the liquid compositions (a) and plagioclase compositions (b) used in the calibrations of Lange et al. (2009) and the rhyolite hygrometer.....149
- Figure 5.2** A plot of the liquid An-number v. mol% An of the plagioclase grown in the phase equilibrium experiments used in the hygrometer of Lange et al. (2009) and the rhyolite hygrometer.....151
- Figure 5.3** (a) A plot of calculated wt% H₂O by the rhyolite hygrometer and measured wt% H₂O with a 1:1 correspondence line (solid lines) and the standard error (± 0.38) (dashed lines) of the model. (b) A plot of wt% H₂O calculated with the rhyolite hygrometer and the residuals with the standard error (± 0.38) shown as dashed lines. There are no patterns in the residuals as a function of wt% H₂O.....154
- Figure 5.4** Phase diagram for the Toba Tuff from Gardner et al. (2002). Isopleths of dissolved melt water are calculated using the water solubility model of Liu et al. (2005) and the bulk composition used in the phase equilibrium experiments of Gardner et al. (2002). The rhyolite hygrometer predicts a dissolved melt H₂O content of 7.1 wt%

(shown as a star) for the bulk composition of the Older Toba Tuff, most calcic plagioclase composition (An₃₀), and pre-eruptive temperature (722°C) presented in Chesner (1998). The water content derived from the hygrometer corresponds to a pressure of 2700 bars using the H₂O solubility model of Liu et al. (2005). Also shown are the wt% H₂O values from FTIR analyses of quartz hosted melt inclusions reported by Chesner and Luhr (2010) (as hollow circles) plotted at the pre-eruptive temperature of the older Toba Tuff reported by Chesner (1998).....156

Figure 5.5 Melt H₂O concentrations derived from the plagioclase-liquid hygrometer (noted as –Plag) for the Huckleberry Ridge, Mesa Falls, and Lava Creek Tuffs plotted with the respective pre-eruptive temperatures reported by Gansecki (1998). Also shown are the wt% H₂O concentrations measured in melt inclusions in Gansecki (1998). The dissolved melt H₂O contents derived from the plagioclase hygrometer match those measured in melt inclusions.....158

Figure 5.6 (a) Melt H₂O contents calculated for the Bishop Tuff using the bulk compositions from Hildreth (1977), pre-eruptive temperatures, calculated using the iron oxide compositions from Hildreth (1977) and the geo-thermometer of Ghiorso and Evans (2008), and the maximum and minimum mol% An in plagioclase, where the mol% Ab in plagioclase is equal to 1-mol% An. The error bars reflect the range of H₂O contents in a given sample. (b) Melt H₂O contents calculated for the Bishop Tuff using the same conditions as in (a), except the plagioclase compositions incorporated into the hygrometer in (b) are calculated using the mol% Ab in plagioclase, where mol% An is defined as 1-mol% Ab. The error bars reflect the range of H₂O contents in a given sample. Also shown in (a) and (b) are the melt water contents measures in melt inclusions from the Bishop Tuff from the studies of Anderson et al. (2000) and Wallace et al. (1999). The symbols are the average temperature and H₂O content measured in the melt inclusions and the X error bars show the range of temperature and spread of wt% H₂O in melt inclusions from the early, middle, and late Bishop Tuff.....160

APPENDIX A

Figure A1 Location maps for the samples featured in this study.....257

Figure A2 Plagioclase and orthopyroxene grains with inclusions of titanomagnetite, ilmenite and plagioclase.....258

Figure A3 A plot of XMg/XMn_{ilmenite} v. XMg/XMn_{titanomagnetite} for all possible pairs of ilmenite and titanomagnetite and the test of equilibrium proposed by Bacon and Hirschmann (1988).....259

Figure A4 Compositional traverses of plagioclase (mol% An) and orthopyroxene (Mg#) phenocrysts in MLV-36, as a function of rim to rim distance across a grain.....260

Figure A5 Plot of NNO v. temperature results for all possible pairings of iron oxide...261

Figure A6 BSE images of plagioclase crystals in COMP-3.....	262
Figure A7 BSE images of chromian spinel growth textures from experiments of Roeder et al. (2001), where a basaltic liquid was held at 1225°C, then cooled slowly over eight hours to 1147°C and then quenched.....	263

APPENDIX B

Figure B1 Photograph of glassy obsidians that show no sign of secondary alteration...	267
Figure B2 All possible pairings of ilmenite and titanomagnetite for each sample shown with the Bacon and Hirschmann (1988) test of equilibrium. No pairs deviate strongly from the proposed equilibrium.....	268
Figure B3 The range of temperatures and Δ NNO values that result from all possible pairings of ilmenite and titanomagnetite and the geo-thermometer of Ghiorso and Evans (2008). All possible pairings of oxides span a small range in temperature and Δ NNO values.....	269
Figure B4 The range of wt% FeO values that result from the range of Δ NNO values obtained from the iron oxides. The concentration of FeO does not deviate strongly when accounting for the range of Δ NNO values in each sample.....	270

APPENDIX C

Figure C1 (a) Plots of $\log(X_{Mg}/X_{Mn})_{\text{ilmenite}}$ v. $\log(X_{Mg}/X_{Mn})_{\text{magnetite}}$ with the equilibrium proposed by Bacon & Hirschmann (1988). (b) Plots of the temperature and fO_2 (as a function of the nickel-nickel oxide buffer) results from the geo-thermometer and oxygen barometer of Ghiorso & Evans (2008) for all possible pairings of ilmenite and titanomagnetite.....	310
Figure C2 Plot of experiment duration (hours) v. the pressure of the decompression experiment conducted at 2.9 MPa/hr (a) and 0.8 MPa/hr.....	311
Figure C3: H ₂ O contents measured in selected experiments (presented in Table C3) by Fourier transform infrared (FTIR) spectroscopy versus H ₂ O contents modeled with the solubility model of Liu et al. (2005).....	312

APPENDIX D

Figure D1 A plot of measured wt% H ₂ O versus calculated wt% H ₂ O using the rhyolite hygrometer and the hygrometer of Lange et al. (2009).....	315
--	-----

LIST OF APPENDICIES

APPENDIX A.....171

APPENDIX B.....264

APPENDIX C.....271

APPENDIX D.....313

CHAPTER I INTRODUCTION

Rhyolites (lavas with ≥ 70 wt% SiO₂ on the dry basis hereafter) are the most differentiated lavas on earth, and known for their voluminous, explosive eruptions (e.g., Bishop Tuff, 600 km³; Hildreth and Wilson, 2007). Rhyolites commonly occur in continental settings where basalts (~50 wt% SiO₂) are erupting coevally and are emplaced in the upper crust, like regions undergoing extension (e.g., Long Valley Caldera; Bailey, 2004) or regions undergoing intraplate volcanism (e.g., Yellowstone Caldera; Christiansen, 2001). Rhyolites, however, are not restricted to these settings, as they also erupt in low frequency with large volumes of intermediate lavas (e.g., andesites and dacites; 58-70 wt% SiO₂) from volcanic arcs above subduction zones (e.g., Toba, Sumatra; Chesner, 1998).

Rhyolite lavas that erupt bimodally with basalts have significant compositional differences from rhyolites that erupt from volcanic arcs. Moreover, the rhyolite lavas can be divided into two groups: highly evolved and less evolved. The highly evolved rhyolites have slightly higher concentrations of SiO₂ (>73 wt%), low concentrations of CaO (<0.6 wt%), MgO (<0.3 wt%), Sr (<50 ppm) and Ba (<400 ppm). The less evolved rhyolites have lower concentrations of SiO₂ and greater concentrations of CaO, MgO, Sr and Ba than the highly evolved rhyolites. The difference in the compositions of the less evolved and the highly evolved rhyolites is reflected in the mineralogy of each rhyolite. Quartz and sanidine are often observed in the highly evolved rhyolites, but are rarely

observed in the less evolved rhyolites. Rhyolites that erupt bimodally with basalts are typically highly evolved, whereas rhyolites that erupt with andesites and dacites tend to be less evolved.

The highly evolved rhyolites are paradoxical as they frequently erupt with basalt (the least differentiated lavas) in the absence of large volumes of intermediate volcanics (e.g., Long Valley Caldera; Bailey, 2004). Thus the mechanism of differentiation by which rhyolite magmas are produced should account for their large volumes, patterns of major and trace elements, diversity of phenocryst phases, and geologic record of the volcanic fields that feature the eruptions of rhyolites. Additionally, the evolution of rhyolite magmas is of particular interest as their formation must fundamentally re-constitute and differentiate continental crust.

A commonly accepted mechanism of differentiation in igneous systems is the theory of crystal fractionation, which was demonstrated by Bowen (1928) in a series of anhydrous phase-diagrams and crystal settling experiments. Bowen (1928) hypothesized that silica-enriched, evolved liquids (>53 wt% SiO₂) are the residual liquids that result from the crystallization and removal of silica-poor phenocrysts from a parental liquid (e.g., basalt). As part of the theory of crystal fractionation, Bowen (1928) also suggested that the most evolved liquids (e.g., rhyolites) form at slower cooling rates that allow the parental material to reach a greater degree of crystallinity and crystal settling, which causes the interstitial, residual liquid to become more silica-rich. The hypothesis that differentiation occurs by crystal fractionation was hailed by a majority of the scientific community as the most satisfactory mechanism to explain the formation of intermediate magmas and rhyolites. While crystal fractionation provides an excellent explanation for

compositional trends observed in large volumes of mafic magmas (e.g., Skarrgard, Greenland), it fails to explain trends observed in the geologic record. Crystal fractionation cannot account for why regions that erupt volumes of lavas that are overwhelmingly basaltic in composition (e.g., Hawaii) fail to produce voluminous rhyolites, and it cannot explain why basalt and rhyolite occur together, in the absence of intermediate volcanics, in regions of extension (e.g., Long Valley Caldera; Bailey, 2004). While the theory of crystal fractionation explains how silica enriched liquids are produced during crystallization of large volumes of basalt, the experiments on which the theory was based were anhydrous, and crystal fractionation as presented by Bowen (1928) does not account for any effect of the H₂O component.

Since the publication of Bowen (1928), water has been identified as a critical component in generating basaltic melts in mantle in subduction zone systems (Gaetani and Grove, 1998, 2003), shifting the equilibrium compositions of minerals (Sisson and Grove, 1993), and as a driving mechanism for explosive eruptions (Sparks, 1978; Gardner et al., 1996; Papale et al., 1999). Water is incorporated into differentiation models by altering the compositions of phenocrysts that are growing from parental liquids so that compositions of phenocrysts reflect water-saturated conditions. While the H₂O component is accounted for in the phenocryst composition, the proposed mechanism of differentiation is still the separation of crystals from melt by cooling and crystal settling (e.g., Grove et al., 2005).

It has also been proposed that intermediate to silicic magmas (>58 wt% SiO₂) may be formed during partial melting of preexisting continental (granitoid) crust by underplating of high temperature, hydrous basaltic liquids (Smith and Leeman, 1987;

Huppert and Sparks, 1988; Atherton and Petford, 1993; Rapp and Watson, 1995; Chappell and White, 2001; Petford and Gallagher, 2001; Annen et al., 2006; Ownby and Lange, 2012). In an experimental test of the origins of granite, Tuttle and Bowen (1958) demonstrated that partial melts of haplogranites (quartz-albite-orthoclase system) in the presence of a hydrous vapor (e.g., H₂O saturated melting) have rhyolitic compositions. Extending the conclusions of Tuttle and Bowen (1958) to natural systems implies that partial melts plutonic rocks that are saturated with quartz, albite, and orthoclase (e.g., granitoids: granite, grannodiorite, and tonalite) will have a eutectic, rhyolitic compositions.

There is no consensus on which mechanism is more likely in the creation of voluminous rhyolites and different mechanisms are favored based on geochemical and isotopic evidence unique to the individual volcanic field. For example, Halliday et al. (1991) suggested that crystal fractionation is the only way to account for Sr and Rb concentrations in the Bishop Tuff, and Davies and Halliday (1998) support the conclusions of Halliday et al. (1991) with evidence from the Sr isotope system (Sr-Rb) that demonstrates the Bishop Tuff can be derived from crystal fractionation of mantle derived basalt. In contrast, Bindeman and Valley (2000, 2001) propose that nearly entire partial melting of the upper crust beneath Yellowstone is the only way to account for the oxygen isotopes in the Lava Creek Tuff. Regardless of the mechanism of differentiation, it is conceivable that water plays an essential role in formation of rhyolite liquids and the differentiation process, as earth is the only planet with both liquid water and granitoid crust. To determine the role of H₂O in the differentiation process, the concentrations of

H₂O in rhyolites and effects of H₂O on the phenocryst assemblage and intensive variables must be documented.

Direct measurement of H₂O contents is only possible in rapidly quenched groundmass glasses if H₂O concentration is low (e.g. Wysoczanski et al., 2005; Saal et al., 2008) or quenched glasses in melt inclusions (e.g., Anderson et al., 1989; Lowenstern, 1994; Wallace et al., 1999; Métrich and Wallace, 2008). Groundmass glasses that retain their dissolved volatiles, however, are unusual and form under very specific conditions (e.g., subaqueous eruption and low H₂O concentration). Quartz-hosted melt inclusions, however, have been used to determine pre-eruptive water contents of 3.5-6.5 wt% for the Bishop Tuff (Anderson et al., 1989; Skirius et al., 1990; Dunbar and Hervig, 1992; Wallace et al., 1994, 1999), 4.3-5.9 wt% for the Taupo Tuffs (Dunbar et al., 1989; Chesner, 2010), and 6-8 wt% for the Pine Grove Tuff (Lowenstern, 1994). While quartz hosted melt inclusions are useful in determining water contents for rhyolites, as discussed above not all rhyolites contain quartz phenocrysts.

H₂O concentrations can also be calculated with hygrometers and phenocryst phases. The mineral plagioclase, a solid solution between anorthite (CaAl₂Si₂O₈) and albite (NaAlSi₃O₈), is often a basis for hygrometers (e.g., Housh and Luhr, 1991; Putirka, 2005; Lange et al., 2009) as its composition is dependent on melt composition, temperature and pressure. H₂O is dissolved in the melt as molecular H₂O (H₂O_m) and OH⁻ groups (Stolper 1982a, b), and there is evidence in the JANAF thermodynamic tables that OH⁻ groups preferentially bond with Na⁺, and bond to a lesser extent to Ca²⁺. Experiments have shown that plagioclase becomes enriched in anorthite component at high temperatures and high melt water contents for a given melt composition (e.g., basalt

or rhyolite) (Sisson and Grove, 1993). An effect of melt composition on plagioclase composition is observed, where by calcium-rich plagioclase is observed in calcium rich melts, silica poor melts (e.g., basalts), and sodium-rich plagioclase is observed in calcium-poor, silica rich melts (e.g., rhyolites). In general, to apply a hygrometer to plagioclase crystals in a magma, the pre-eruptive temperature must also be known (e.g. Lange et al., 2009). Rhyolites are often saturated in multiple phenocryst phases, which allow for the calculation of pre-eruptive intensive variables (e.g., temperature). For example, even the most crystal poor (<2%) units of the Bishop Tuff are saturated in nine phenocrysts phases (Hildreth and Wilson, 2007). Rhyolites are often minimally saturated in two iron oxides, ilmenite and titanomagnetite (Carmichael, 1967), which can be used with geo-thermometers/oxygen barometers (e.g., Buddington and Lindsley, 1964; Ghiorso and Evans, 2008) to calculate pre-eruptive temperatures and oxidation states. Because rhyolites cooled rapidly, these pre-eruptive temperatures apply to all minerals, including plagioclase. Hence, application of the hygrometer of Lange et al. (2009) to rhyolites to determine melt water contents should be relatively straightforward, as they are often saturated in ilmenite, titanomagnetite and plagioclase.

In this study, the effects of H₂O on the phenocryst assemblages, intrinsic variables, and melt viscosity are evaluated in phenocryst-poor rhyolite obsidians from western Mexico and Medicine Lake Volcano, CA. The origin of the phenocryst assemblage was evaluated with a detailed electron microprobe study, the plagioclase liquid hygrometer of Lange et al. (2009), the water solubility model of Liu et al., (2005), the viscosity model of Hui and Zhang (2007), crystal nucleation and growth studies (Couch et al., 2003a, b; Martel and Schmidt, 2003; Brugger and Hammer, 2010), and

phase diagrams from the literature (Tomiya et al., 2010), as well as a phase diagrams produced from a series of phase equilibrium experiments conducted in cold seal pressure vessels at the National Museum of Natural History, Smithsonian Institute, Washington, D.C.

In Chapter II of this study, the hygrometer of Lange et al. (2009) is applied to the plagioclase phenocrysts found in six crystal-poor rhyolite obsidians, where the temperatures used with the hygrometer are those calculated with the geo-thermometer of Ghiorso and Evans (2008). Surprisingly, plagioclase and orthopyroxene compositions in all six obsidians spanned a wide range composition. For example, plagioclase and orthopyroxene in MLV-45 spanned a range of 30-68 mol% An and 50-65 mol% En, respectively, despite low phenocryst abundances (<4.5%). To further investigate the wide range of plagioclase and orthopyroxene compositions, back-scatter electron (BSE) images of plagioclase and orthopyroxene textures were collected and compared with the compositions of individual crystals and the range of compositions observed in each sample. In general, textures of plagioclase and orthopyroxene grains ranged from euhedral, to lobate and rounded, to vermiform, suggesting a diffusion-limited growth regime. When the hygrometer of Lange et al. (2009) was applied to the range of plagioclase compositions, the result was a range higher than most H₂O contents recorded by most melt inclusions from quartz >6 wt% H₂O (e.g., Wallace et al., 1999). It was found that the calibration of Lange et al. (2009) does not adequately cover the entire range of rhyolite liquids, even though ~10% of the calibration is composed of phase equilibrium experiments on low-silica (≤ 73 wt% SiO₂) rhyolite liquids, and application of the hygrometer to highly differentiated magmas is an extrapolation in terms of the liquid

composition (discussed in Chapter IV). To address this issue in Chapter II, a version of the plagioclase liquid hygrometer, with more plagioclase rhyolite liquid pairs in the dataset used for calibration, was applied to the obsidians calibrated on the dataset of Lange et al. (2009) as well as new phase-equilibrium experiments on rhyolite liquid that were published since 2009 (Lange et al., 2012). Maximum water contents determined with the modified calibration of the Lange et al. (2009) hygrometer and the plagioclase from the six rhyolites range from 2.3 to 6.8 wt% H₂O, and minimum water contents range from 2.1 to 4.0 wt% H₂O. These results require that the rhyolites were water saturated at upper crustal pressures (100-300 MPa).

When phenocrysts with wide ranges in composition and complex textures are observed in melts of intermediate compositions they are often attributed to magma mixing or mingling (Murphy et al., 2000; Tepley et al., 2000; Kent et al., 2010). However, because the six rhyolites are an end-member composition and there is no obvious evidence of mixing, it is likely that the phenocrysts grew due to degassing induced crystallization, owing to loss of melt water upon eruption. As H₂O is continuously lost from the melt, the activities of melt components (e.g., SiO₂, Al₂O₃) change, which causes a change in phenocrysts compositions to reflect lower melt water contents. That is, the phenocrysts record decreasing melt water contents. Because both plagioclase and orthopyroxene from Chapter II span a range in compositions with complex textures, with little crystallization and no trend of cooling recorded by the iron-oxides in the six rhyolites, it is likely that the phenocryst assemblages grew as a result of degassing induced crystallization. This work was recently published in *Contributions to Mineralogy and Petrology* (Waters and Lange, 2013).

Chapter III investigates the effect of the dissolved H₂O on the activities of Fe²⁺ and Fe³⁺ in the rhyolite melts. Testing the effect of degassing of H₂O on rhyolite liquids is ideal as they have the lowest total iron concentrations, which makes them the most sensitive indicators of any changes to the ferric-ferrous ratio. The effect of H₂O on the activities of ferrous and ferric iron is the subject of much debate in the literature, and it is postulated that dissolved H₂O affects the ferric-ferrous ratio in two ways: (1) by altering the activities of ferrous and/or ferric iron (Baker & Rutherford, 1996; Gaillard et al., 2001; Wilke et al., 2002; Gaillard et al., 2003), and (2) or by the loss of Fe²⁺ and Fe³⁺ to the fluid phases during degassing (Sisson and Grove, 2003). Baker & Rutherford (1996), Gaillard et al. (2001), Wilke et al. (2002) and Gaillard et al. (2003) experimentally demonstrate that water does exert some effect on the activities of ferric and ferrous iron at conditions more reducing than the Ni-NiO buffer where fO₂ is low, however, the experimental study of Moore et al. (1995) shows that H₂O does not exert control over the ferric-ferrous ratio (i.e., the activity of Fe²⁺ and Fe³⁺) at fO₂ conditions ~Ni-NiO buffer.

To resolve the discrepancy surrounding the debate in the literature, the pre-eruptive (H₂O-saturated conditions) wt% FeO is compared with the post-eruptive (degassed) wt% FeO in the rhyolites from Chapter II. The water contents of the rhyolites are known from Chapter II and the rhyolites must have been water saturated at upper crustal pressures (100-300 MPa). Nearly complete degassing of the rhyolites occurred based on low loss on ignition (LOI) values (<0.7 wt%). Pre-eruptive wt% FeO was calculated by incorporating the temperatures and oxygen fugacities calculated with the two iron oxide geo-thermometer and oxygen barometer of Ghiorso and Evans (2008) into the empirically calibrated model of Kress and Carmichael (1991). Crabtree and Lange

(2012) demonstrate that even though the model of Kress and Carmichael (1991) is calibrated on anhydrous glasses it accurately predicts ferric-ferrous ratios in H₂O-saturated liquids. The post-eruptive wt% FeO is measured by back titration using the Wilson method (1960). It was found that H₂O exerts no measurable effect on the ferric-ferrous ratio in rhyolites. These results suggest that the degassing of H₂O from rhyolite liquids at fO₂ conditions ranging from $\Delta\text{NNO} -0.4$ to $\Delta\text{NNO} 1.4$ has no resolvable effect on the ferric-ferrous ratio of rhyolites with low total iron concentrations. This work will be submitted to Science.

The effect of H₂O on mineral-liquid equilibrium is a common theme in the literature, and phase equilibrium experiments provide significant benchmarks to evaluate the effect of melt water contents on phenocrysts in natural liquids (Gardner et al., 1995; Couch et al., 2003; Martel and Schmidt, 2003; Tomiya et al. 2010). The exsolution of volatiles from melt has also been proposed to be the driving mechanism for crystallization of phenocrysts in Chapter II and is supported by melt inclusions (e.g., Métrich and Wallace, 2008) and observations from crystal-poor andesites and dacites from western Mexico (Crabtree and Lange, 2011). The vast majority of phase equilibrium studies target the pressure and temperature conditions at which all the phases documented in natural samples coexist, which are often equated to a depth of pre-eruptive storage conditions (i.e., magma chamber). In this study, phenocryst growth at pre-eruptive storage conditions is challenged with an evaluation of the effect of changing melt water concentrations on phenocryst compositions and nucleation and growth rates during decompression and ascent.

In Chapter IV, phase equilibrium experiments are conducted on one less

differentiated rhyolite from Chapter II, a highly differentiated rhyolite from Medicine Lake Volcano, and a rhyodacite from western Mexico, to test the effect of dissolved water on the phenocryst phases and to provide experimental data to extend the calibration of the Lange et al. (2009) hygrometer (Chapter V). The phase equilibrium experiments were conducted in Ni-rich (Waspaloy) cold-seal pressure vessels at the Department of Mineral Sciences, National Museum of Natural History, Smithsonian Institute in Washington D.C. in collaboration with Benjamin Andrews. Phase diagrams were produced for each of the three obsidians, and decompression experiments were conducted on the less differentiated rhyolite to document whether or not it is possible for crystallization of phenocrysts to occur during decompression. Decompression experiments on the low silica rhyolite were conducted at continuous rates of 2.9 MPa/hr and 0.8 MPa/hr. Experiments that were decompressed at 2.9 MPa/hr did not nucleate or grow any phenocryst phase. The 0.8 MPa/hr decompression experiments crystallized phenocrysts with compositions that are consistent with the phase equilibrium experiments and match the natural sample, which suggest that degassing induced crystallization of phenocrysts is a plausible hypothesis to explain the compositional variability in plagioclase in phenocryst-poor obsidians.

From comparison of the range of plagioclase compositions observed in the natural sample with the plagioclase compositions grown at the eruptive temperature in the phase equilibrium experiments, it was determined that plagioclase nucleation and growth in the natural sample ceases after ~20 MPa of decompression, even though plagioclase is stable at increasingly lower pressures. Additionally, plagioclase nucleation and growth in the natural sample ceases before nucleation and growth rates reach their reported maximums

based on comparison with Couch et al. (2003b) and Hammer and Rutherford (2002). The decompression experiments of Martel and Schmidt (2003) demonstrate that as decompression rate increases, the pressure at which plagioclase nucleation and growth ceases becomes increasingly higher. The decompression rates of the experiments of Martel and Schmidt (2003) were investigated with respect to the rate of loss of H₂O and the rate of change of viscosity. Based on the results of Martel and Schmidt (2003), it appears that rapidly changing melt viscosity, due to degassing upon ascent, is the most plausible mechanism to suppress of plagioclase nucleation and growth, by effectively retarding the diffusivity of plagioclase forming components. This work will be submitted to Journal of Petrology.

By comparing the water contents derived for the rhyolites in Chapter II from the hygrometer of Lange et al. (2009) with the results of the phase equilibrium experiments in Chapter IV, it was observed that the hygrometer of Lange et al. (2009) over predicted melt H₂O contents for rhyolite liquids. Further investigation of the calibration of the model of Lange et al. (2009) revealed that application of the hygrometer to a majority of rhyolites is an extrapolation in terms of the liquid composition. The calibration of Lange et al. (2009) was limited to melt compositions ≤ 73 wt% SiO₂, due to a lack of high quality H₂O saturated rhyolite phase equilibrium experiments (e.g., glass totals >97% including the H₂O component). Since 2009, several phase equilibrium studies on rhyolite liquid have been published in the literature (Tomiya et al., 2010; Martel et al., 2012; Castro et al., 2013) and those data, combined with the 22 plagioclase-liquid equilibrium pairs presented in Chapter IV, and phase equilibrium experiments from Larsen (2005, 2006) and Martel (2006) were used in a new calibration for the model of Lange et al.

(2009) to calculate melt water contents for rhyolite liquids in Chapter V. In total the dataset for the calibration of the rhyolite hygrometer consists of 73 experiments that span a range of liquid compositions (68.9-79.7 wt% SiO₂), plagioclase compositions (17-64 mol% An), temperatures (750-1040°C), pressures (30-300 MPa), and water contents (0.9-7.3 wt%). The backwards stepwise multiple linear regression of the dataset for calibration for the rhyolite hygrometer yields eight significant terms, five of which are fitted terms for the mole fraction of melt components: SiO₂, Al₂O₃, FeO^T, Na₂O, K₂O. The regression has a standard error estimate of ± 0.38 wt% H₂O and an adjusted R² value of 0.92. The maximum residual from the regression is 0.84 wt% H₂O.

The rhyolite hygrometer is applied to the oldest eruptive unit of the Toba Tuff, the three Tuffs erupted from Yellowstone Caldera (Huckleberry Ridge, Mesa Falls and Lava Creek), and the Bishop Tuff where available whole rock compositions, corresponding plagioclase compositions, and pre-eruptive temperatures and H₂O contents in melt inclusions can be found in the literature (Hildreth, 1977; Gansecki, 1998; Chesner, 1998; Wallace et al., 1999; Anderson et al., 2000; Chesner and Luhr, 2010). The rhyolite hygrometer predicts a dissolved melt water content that is consistent with the phase diagram for the Toba Tuff present in Gardner et al. (2002) and ~1 wt% H₂O greater than H₂O contents recorded by melt inclusions. The discrepancy between the H₂O contents from the rhyolite hygrometer and the melt inclusions can be accounted for by the saturation of plagioclase at higher P_{H₂O}, at upper crustal pressures (100-300 MPa at ~725°C) and H₂O fluid saturated conditions. The H₂O contents derived from the plagioclase hygrometer for the Yellowstone and Bishop Tuffs match those measured in melt inclusions. This work will be submitted to American Mineralogist.

A final assessment of the origin of rhyolites and phenocryst assemblages in rhyolite is made in Chapter VI. Because degassing induced crystallization can account for the variability in phenocryst compositions, the rhyolites in this study must have existed as aphyric, water-saturated liquids at depth, which then ascended, degassed, crystallized and erupted. Possible sources of the rhyolites, implications of degassing induced crystallization, and the possible applications of plagioclase speedometry are discussed.

REFERENCES

- Anderson, A.T., Davis, A.M., and Lu, F. (2000) Evolution of Bishop Tuff Rhyolitic Magma based on Melt and Magnetite Inclusions and Zoned Phenocrysts. *Journal of Petrology* 41, 449-473
- Annen, C., Blundy, J.D., and Sparks, R.S.J. (2006) The genesis of intermediate and silicic magmas in deep crustal hot zones. *Journal of Petrology* 47, 505-539.
- Ardia, P., Giordano, D., and Schmidt, M.W. (2008) A model for the viscosity of rhyolite as a function of H₂O-content and pressure: A calibration based on centrifuge piston cylinder experiments. *Geochimica et Cosmochimica Acta* 72, 6103-6123.
- Atherton, M. P. & Petford, N. (1993). Generation of sodium rich magmas from newly underplated basaltic crust. *Nature* 362, 144–146.
- Baker, L.L. & Rutherford, M.J. (1996). The effect of dissolved water on the oxidation state of silicic melts. *Geochimica et Cosmochimica Acta* 60, 2179-2187.
- Bailey, R.A. (2004) *Eruptive History and Chemical Evolution of the Precaldera and Postcaldera Basalt-Dacite Sequences, Long Valley, California: Implications for Magma Sources, Current Seismic Unrest, and Future Volcanism*. U.S. Geological Survey Professional Paper 1692, p.86
- Bindeman, I.N., and Valley, J.W. (2000) The formation of low- $\delta^{18}\text{O}$ rhyolites after caldera collapse at Yellowstone, Wyoming, USA. *Geology* 28, 719-722.
- Bindeman, I.N., and Valley, J.W. (2001) Low- $\delta^{18}\text{O}$ Rhyolites from Yellowstone: magmatic evolution based on analyses of zircons and individual phenocrysts. *Journal of Petrology* 42, 1491-1517
- Bowen, N.L. (1928) *Evolution of the Igneous Rocks*, Princeton University Press, Princeton
- Brugger, C.R. and Hammer, J.E. (2010) Crystallization kinetics in continuous decompression experiments: implications for interpreting natural magma ascent processes. *Journal of Petrology* 51, 1941-1965
- Buddington, A. F., and D. H., Lindsley. (1964) Iron-titanium oxide minerals and synthetic equivalents. *Journal of Petrology* 5, 310-357

- Carmichael, I.S.E. (1967) The iron-titanium oxides of salic volcanic rocks and their associated ferromagnesian silicates. *Contributions to Mineralogy and Petrology* 14, 36-64.
- Castro, J.M., Schipper, I.C., Mueller, S.P., Militzer, A. S., Amigo, A., Parejas, C.S., and Jacob, D. (2013) Storage and eruption of near-liquidus rhyolite at Cordón Caulle, Chile. *Bulletin of Volcanology* 75, 701-718
- Chappell, B. W. & White, J. R. (2001). Two contrasting granite types: 25 years later: *Australian Journal of Earth Sciences* 48, 489-499
- Chesner, C.A. (1998) Petrogenesis of the Toba Tuffs, Sumatra, Indonesia. *Journal of Petrology* 39, 397-438
- Chesner, C.A. and Luhr, J.F. (2010) A melt inclusion study of the Toba Tuffs, Sumatra, Indonesia. *Journal of Volcanology and Geothermal Research* 197:SI, 259-278
- Christiansen, R. L. (2001). The Quaternary and Pliocene Yellowstone Plateau Volcanic Field of Wyoming, Idaho, and Montana. U.S. Geological Survey Professional Paper, 729-G, 145 p. 3 plates
- Clemente, B., Scaillet, B., and Pichavant, M. (2004). The solubility of sulphur in hydrous rhyolitic melts. *Journal of Petrology* 45, 2171-2196
- Coombs M.L. and Gardner J.E. (2001) Shallow-storage conditions for the rhyolite of the 1912 eruption at Novarupta, Alaska. *Geology* 29, 775-778
- Couch S., Harford, C.L., Sparks, R.S.J., and Carroll, M.R. (2003a) Experimental constraints on the conditions of formation of highly calcic plagioclase microlites at the Soufriere Hills Volcano, Montserrat. *Journal of Petrology* 44, 1455-1475
- Couch S., Sparks, R.S.J., and Carroll, M.R. (2003b) The kinetics of degassing-induced crystallization at Soufriere Hills Volcano, Montserrat. *J Petrol* 44:1477-1502
- Crabtree, S.M., and Lange, R.A. (2011) Complex Phenocryst Textures and Zoning Patterns in Andesites and Dacites: Evidence of Degassing-Induced Rapid Crystallization? *Journal of Petrology* 52, 3-38
- Crabtree, S.M., and Lange, R.A. (2012) An evaluation of the effect of degassing on the oxidation state of hydrous andesite and dacite magmas: a comparison of pre- and post-eruptive Fe²⁺ concentrations. *Contributions to Mineralogy and Petrology* 163, 209-224
- Davies, G.R. and Halliday, A.N. (1998) Development of the Long Valley rhyolite magma system: strontium and neodymium isotope evidence from glasses and individual phenocrysts. *Geochimica et Cosmochimica Acta* 62, 3561-3574
- Dunbar, N.W. and Hervig, R.L. (1992) Petrogenesis and volatile stratigraphy of the Bishop Tuff: Evidence from melt inclusions and analyses. *Journal of Geophysical Research* 97, 15129-15150.
- Dunbar, N.W., Hervig, R.L., and Kyle, P.R. (1989) Determination of pre-eruptive H₂O, F and Cl contents of silicic magmas using melt inclusions: examples from Taupo volcanic center, New Zealand. *Bulletin of Volcanology* 51, 177-184
- Gaetani, G. A. and Grove, T.L. (1998) The influence of water on melting of mantle peridotite. *Contributions to Mineralogy and Petrology* 131, 323-346.

- Gaetani, G.A., Grove, T.L. (2003) Experimental constraints on melt generation in the mantle wedge. In **Inside the Subduction Factory**, J. Eiler, ed., American Geophysical Monograph, 138, 107-133
- Gaillard, F., Scaillet, B., Pichavant, M., and Beny, J.M. (2001) The effect of water and fO₂ on the ferric-ferrous ratio of silicic melts. *Chemical Geology* 174, 255-273.
- Gaillard, F., Pichavant, M., and Scaillet, B. (2003) Experimental determination of activities of FeO and Fe₂O₃ components in hydrous silicic melts under oxidizing conditions. *Geochimica et Cosmochimica Acta* 67, 4389-4409
- Ganseccki, C.A. (1998) ⁴⁰Ar/³⁹Ar geochronology and pre-eruptive geochemistry of the Yellowstone Plateau volcanic field rhyolites Ph.D. thesis, Stanford University
- Gardner, J.E., Thomas, R.M.E., Jaupart, C., and Tait, S. (1996) Fragmentation of magma during Plinian volcanic eruptions. *Bulletin of Volcanology* 58, 144-162
- Ghiorso, M. and Evans, B.W. (2008) Thermodynamics of rhombohedral oxide solid solutions and a revision of the Fe-Ti two-oxide geothermometer and oxygen barometer. *Am J Sci* 308:957-1039
- Grove, T.L., Baker, M.B., Price, R.C., Parman, S.W., Elkins-Tanton, L.T., Chatterjee, N., and Müntener, O. (2005) Magnesian andesite and dacite lavas from Mt. Shasta, northern California: products of fractional crystallization of H₂O-rich mantle melts. *Contributions to Mineralogy and Petrology* 148, 542-565
- Halliday, A.N., Davidson, J.P., Hildreth, W., and Holden, P. (1991) Modeling the petrogenesis of high Rb/Sr silicic magmas. *Chemical Geology* 92, 107-114.
- Hammer J.E., and Rutherford, M.J. (2002) An experimental study of the kinetics of decompression induced crystallization in silicic melt. *Journal of Geophysical Research* 107(B1): 2021
- Hildreth, W. (1977) The magma chamber of the Bishop Tuff: gradients in temperature, pressure, and composition. Ph.D. thesis, University of California, Berkeley
- Hildreth, W. and Wilson, C.J.N. (2007) Compositional zoning of the Bishop Tuff. *Journal of Petrology* 48, 951-999.
- Housh, T.B. and Luhr, J.F. (1991) Plagioclase-melt equilibria in hydrous systems. *American Mineralogist*, 76, 477-492
- Hui J., and Zhang, Y. (2007) Toward a general viscosity equation for natural anhydrous and hydrous silicate melts. *Geochim Cosmochim Acta* 71:403-416
- Hui, H., Zhang, Y., Xu, Z., Gaudio, P.D., and Behrens, H. (2009) Pressure dependence of viscosity of rhyolitic melts. *Geochimica et Cosmochimica Acta* 73, 3680-3693
- Huppert, H. E. & Sparks, S. J. (1988). The generation of granitic magma by intrusion of basalt into continental crust. *Journal of Petrology* 29, 599-624
- Kent, A.J.R., Darr, C., Koleszar, A.M., Salisbury, M.F., and Cooper, K.M. (2010) Preferential eruption of andesitic magmas through recharge filtering. *Nature Geoscience* 3, 631-636
- Kress V, Carmichael ISE (1991) The compressibility of silicate liquids containing Fe₂O₃ and the effect of composition, temperature, oxygen fugacity and pressure on their redox states. *Contributions to Mineralogy and Petrology* 108, 82-92
- Larsen JF (2005) Experimental study of plagioclase rim growths around anorthite seed crystals in rhyodacite melt. *American Mineralogist* 90, 417-427

- Larsen, JF (2006) Rhyodacite magma storage conditions prior to the 3430 yBP caldera-forming eruption of Aniakchak volcano, Alaska. *Contributions to Mineralogy and Petrology* 152, 523-540
- Lange RA, Frey HM, Hector J (2009) A thermodynamic model for the plagioclase-liquid hygrometer/thermometer. *Am Mineral* 94:494-506
- Liu Y, Zhang Y, Behrens H (2005) Solubility of H₂O in rhyolitic melts at low pressure and a new empirical model for mixed H₂O CO₂ solubility in rhyolitic melts. *J Volcanol Geothermal Research* 143, 219-235
- Lowenstern, J.B. (1994b) Dissolved volatile concentrations in an ore-forming magma. *Geology* 22, 893-896
- Martel, C. (2012) Eruption Dynamics Inferred from Microlite Crystallization Experiments: Application to Plinian and Dome-forming Eruptions of Mt. Pelee (Martinique, Lesser Antilles). *Journal of Petrology* 53, 699-725
- Martel, C., Schmidt, B.C. (2003) Decompression experiments as an insight into ascent rates of silicic magmas. *Contributions to Mineralogy and Petrology* 144, 397-415
- Métrich, N. and Wallace, P., (2008) Volatile Abundances in Basaltic Magmas and Their Degassing Paths Tracked by Melt Inclusions. Eds., Putirka, K.D. and Tepley III, F.J. *Reviews in Mineralogy and Geochemistry* 69, 363-402.
- Moore, G., Righter, K., & Carmichael, I.S.E. (1995). The effect of dissolved water on the oxidation state of iron in natural silicate liquids. *Contributions to Mineralogy and Petrology* 120, 170-179
- Murphy, M.D., Sparks, R.S.J., Barclay, J., Carroll, M.R., and Brewer, T.S. (2000) Remobilization of Andesite Magma by Intrusion of Mafic Magma at the Soufriere Hills Volcano, Montserrat, West Indies. *Journal of Petrology* 41, 21-42
- Newman S, Lowenstern JB (2002) VOLATILECALC: a silicate melt-H₂O-CO₂ solution model written in Visual Basic for excel. *Comp and Geosci* 28, 597-604
- Papale, P, Neri, A., and Macedonio, G. (1999) The role of water content and magma composition on explosive eruption dynamics. *Physical Chemistry of the Earth* 24, 969-975
- Petford, N. & Gallagher, K. (2001). Partial melting of mafic (amphibolitic) lower crust by periodic influx of basaltic magma. *Earth and Planetary Science Letters* 193, 483–489
- Putirka KD (2005) Igneous thermometers and barometers based on plagioclase + liquids equilibria: Tests of some existing models and new calibrations. *American Mineralogy* 90, 336-346
- Rapp, R. P. & Watson, E. B. (1995). Dehydration melting of metabasalt at 8-32 kbar-implications for continental growth and crust–mantle recycling. *Journal of Petrology* 36, 891–931
- Saal, A.E., Hauri, E.H., Cascio, M. L., Van Orman, J. A., Rutherford, M.C., and Cooper, R.F. (2008) Volatile content of lunar volcanic glasses and the presence of water in the Moon's interior. *Nature* 454, 192-195
- Sisson, T. W. & Grove, T. L. (1993). Experimental investigations of the role of H₂O in calc-alkaline differentiation and subduction zone magmatism. *Contributions to Mineralogy and Petrology* 113, 143–166

- Skirius, C.M. (1990) Pre-eruptive H₂O and CO₂ content of the plinian and ash-flow Bishop Tuff Magma. Ph.D. thesis, University of Chicago, Chicago, Illinois.
- Smith, D. R. & Leeman, W. P. (1987). Petrogenesis of Mount St. Helens dacitic magmas. *Journal of Geophysical Research* 92, 10313–10334
- Sparks, R.S.J. (1976) The dynamics of bubble formation and growth in magmas: A review and analysis. *Journal of Volcanology and Geothermal Research* 3, 1-37
- Steele-Macinnis, M., Esposito, R., and Bodnar, R.J. (2011) Thermodynamic model for the effect of post-entrapment crystallization on the H₂O-CO₂ systematics of vapor-saturated silicate melt inclusions. *Journal of Petrology* 52, 2461-2482
- Stolper, E. (1982a) The speciation of water in silicate melts. *Geochemica et Cosmochemica Acta* 46, 2609-2620
- Stolper, E. (1982b) Water in silicate-glasses-an infrared spectroscopic study. *Contribution to Mineralogy and Petrology* 81, 1-17
- Tepley III, F.J., Davidson, J.P., Tilling, R.I., and Arth, J.G. (2000) Magma mixing, recharge and eruption histories recorded in plagioclase phenocrysts from El Chichón Volcano, Mexico. *Journal of Petrology* 41, 1397-1411.
- Tomiyama, A., Takahashi, E., Furukawa, N., and Suzuki, T. (2010) Depth and Evolution of a Silicic Magma Chamber: Melting Experiments of a Low-K Rhyolite from Usu Volcano, Japan. *Journal of Petrology* 51, 1333-1354
- Tuttle, O.F. and Bowe, N.L. (1958) Origin of granite in the light of experimental studies in the system NaAlSi₃O₈-KAlSi₃O₈-SiO₂-H₂O. *Geological Society of America Memoirs* 74
- Wallace, P.J. Anderson, A.T., and Davis, A.M. (1994) Preeruptive gradients in H₂O, CO₂, and exsolved gas in the magma body of the Bishop tuff. *EOS, Trans. Am. Geophys. Union* 75, 718.
- Wallace P.J., Anderson A.T., and Davis A.M. (1999) Gradients in H₂O, CO₂, and exsolved gas in a large-volume silicic magma system: Interpreting the record preserved in melt inclusions from the Bishop Tuff. *J Geophys Res-Sol Earth* 104, 20097-20122
- Wilke, M., Behrens H., Burkhard, D.J.M., and Rossano, S. (2002) The oxidation state of iron in silicic melt at 500 MPa water pressure. *Chemical Geology* 189, 55-67
- Wyszczanski, R.J., Wright, I.C., Gamble, J.A., Hauri, E.H., Luhr, J.F., Eggins, S.M., Handler, M.R. (2005) Volatile contents of Kermadec Arc havre Trough pillow glasses: Fingerprinting slab-derived aqueous fluids in the mantle sources of arc and back-arc lavas. *Journal of Volcanology and Geothermal Research* 152, 51-73

CHAPTER II

CRYSTAL-POOR, MULTIPLY SATURATED RHYOLITES (OBSIDIANS) FROM THE CASCADE AND MEXICAN ARCS: EVIDENCE OF DEGASSING- INDUCED CRYSTALLIZATION OF PHENOCRYSTS¹

2.1 ABSTRACT

A detailed petrological study is presented for six phenocryst-poor obsidian samples (73-75 wt% SiO₂) erupted as small-volume, monogenetic domes in the Mexican and Cascade arcs. Despite low phenocryst (+ microphenocryst) abundances (2-6%), these rhyolites are each multiply-saturated with five to eight mineral phases (plagioclase + orthopyroxene + titanomagnetite + ilmenite + apatite ± zircon ± hornblende ± clinopyroxene ± sanidine ± pyrrhotite). Plagioclase and orthopyroxene phenocrysts (identified using phase-equilibrium constraints) span ≤ 30 mol% An and ≤ 15% Mg#, respectively. Eruptive temperatures (±1σ), on the basis of Fe-Ti two oxide thermometry, range from 779 (±25) to 940 (±18)°C. Oxygen fugacities (±1σ) range from -0.4 to 1.4 (± 0.1) log units relative to those along the Ni-NiO buffer. With temperature known, the plagioclase-liquid hygrometer was applied; maximum water concentrations calculated for the most calcic plagioclase phenocryst in each sample range from 2.6-6.5 wt%. This requires that the rhyolites were fluid-saturated at depths ≥ 2-7 km. It is proposed that the wide compositional range in plagioclase and orthopyroxene phenocrysts, despite their low abundance, can be attributed to changing melt water concentrations owing to

¹ Citation: Waters, LE. And Lange, R.A. (2013) Crystal-poor, multiply saturated rhyolite (obsidians) from the Cascade and Mexican arcs: Evidence of degassing-induced crystallization of phenocrysts. Contributions to Mineralogy and Petrology 166, 731-754

degassing during magma ascent. Phase-equilibrium experiments from the literature show that higher dissolved water concentrations lead to more Fe-rich orthopyroxene, as well as more calcic plagioclase. Loss of dissolved water leads to a progressive increase in melt viscosity, and phenocrysts often display diffusion-limited growth textures (e.g. dendritic and vermiform), consistent with large undercoolings caused by degassing. A kinetic barrier to microlite crystallization occurred at viscosities from 4.5 to 5.0 log₁₀ Pa s for these rhyolites, presumably because the rate at which melt viscosity changed was high owing to rapid loss of dissolved water during magma ascent.

2.2 INTRODUCTION

Fresh obsidian samples of rhyolite composition (73-75 wt% SiO₂) with sparse crystals (2-6 vol%) provide a unique opportunity to resolve the effects of degassing-induced crystallization vs. magma mixing in producing compositional and textural complexity in phenocrysts, particularly plagioclase and orthopyroxene. It has long been recognized that the effects of magma mixing and/or the incorporation of xenocrysts can lead to a broad compositional spread in crystal populations and a variety of disequilibrium textures, notably in intermediate magmas (e.g., Sakuyima 1978; Eichelberger 1981; Pallister et al. 1992; Wallace and Carmichael 1994; Tepley et al. 1999; Watts et al. 1999; Salisbury et al. 2008; Smith et al. 2009; Ruprecht et al. 2012). However, it is also understood that degassing-induced crystallization can also produce a range of compositions and textures during phenocryst growth (e.g., Lofgren 1974; Anderson 1984; Moore and Carmichael 1998; Brophy et al. 1999; Cashman and Blundy 2000; McCanta et al. 2007; Crabbtree and Lange 2011; Frey and Lange 2011).

For example, the loss of dissolved water during ascent of fluid-saturated magma is expected to change the equilibrium plagioclase to more sodic compositions (e.g., Sisson and Grove 1993; Putirka, 2005) and cause a large undercooling as the liquidus temperature increases, which in turn can promote diffusion-limited crystal growth mechanisms and complex textures (e.g., Lofgren 1974; Kirkpatrick 1975; Roeder et al. 2001; Hammer and Rutherford 2002; Couch et al. 2003; Martel and Schmidt 2003; Szramek et al. 2006; Suzuki et al. 2007). Similarly, there is evidence from phase-equilibrium experiments in the literature and thermodynamic data reported in the JANAF tables that changes in melt water concentration also affect orthopyroxene compositions, with higher water contents favoring Fe-rich compositions (Crabtree and Lange 2011; Frey and Lange 2011). Thus reverse zoning of orthopyroxene (i.e., Mg-rich rims) can sometimes occur because of degassing and is not always a sign of magma mixing.

It is not only intermediate magmas that display a broad range of plagioclase and orthopyroxene compositions and textures, but also rhyolites with 72-76 wt% SiO₂ and with > 1 wt % CaO (i.e., not highly evolved), which have been documented at several locations, including New Zealand, Japan, Indonesia, and Mexico (e.g., Harris 1986; Chesner 1998; Smith et al. 2010; Tomiya et al. 2010). For example, the ~530 km³ caldera-forming Oruanui eruption of zoned rhyolite (dominantly 74-76 wt% SiO₂; 1.5-2.0 wt% CaO) from Taupo Volcano, New Zealand contains plagioclase and orthopyroxene crystals that range continuously from ~An₅₀ to An₃₀ and ~En₅₅ to En₄₅, respectively, regardless of silica content (Wilson et al. 2006). An outstanding question is whether such a wide range of crystal compositions in rhyolite requires open-system processes, or whether degassing-induced crystallization of phenocrysts also plays a role.

In this study, the role of degassing-induced crystallization of plagioclase and orthopyroxene phenocrysts in rhyolites is evaluated through a detailed petrological study of six obsidian samples from the Mexican and Cascades volcanic arcs. The rhyolite samples contain sparse crystals (2-6 vol%) of five to eight different mineral phases in a glassy groundmass and were erupted from small, monogenetic vents. The occurrence of both titanomagnetite and ilmenite permits magmatic temperatures to be calculated (Ghiorso and Evans 2008), and the occurrence of sparse plagioclase allows application of the plagioclase-liquid hygrometer (Lange et al. 2009), with a calibration extended to rhyolite liquids (Lange et al. 2012; Waters et al. 2012), to obtain pre-eruptive water concentrations. The goal of this study is to examine the compositional and textural features of the crystalline assemblage, along with information on pre-eruptive temperatures and water concentrations, as well as comparisons with phase-equilibrium results from the literature, to evaluate the relative contributions of magma mixing, the incorporation of xenocrysts, and degassing-induced crystallization.

2.3 GEOLOGIC SETTING

The six obsidian samples featured in this study are from the southern Cascades arc and western Mexican Volcanic Belt, two areas where rifting is superimposed upon subduction. A location map for all six samples is provided in the Appendix (Figure A1). Each of the samples erupted from a monogenetic vent. Three samples are from western Mexico; COMP-3 and JAL-10 are both from the volcanic field surrounding Volcán Tepitiltic (Frey et al. 2004; 2013). TEQ-21 is peripheral to Volcán Tequila (Lewis-Kenedi et al. 2005). An overview of the tectonic setting of the western Trans-Mexican Volcanic Belt is given in Frey et al. (2007). The other three samples (MLV-36, MLV-37,

and MLV-45) are from the Medicine Lake volcanic complex, in the southern Cascades. Medicine Lake features coeval eruptions of basalt through rhyolite and is located in a geologically complex area where Basin and Range extension overprints the southern Cascades Arc (Grove et al. 1997; Donnelly-Nolan et al. 2008). An extensive eruptive history of Medicine Lake volcanic complex is presented in Donnelly-Nolan et al. (2008).

2.4 WHOLE ROCK GEOCHEMISTRY AND PETROGRAPHY

Six samples were crushed in a steel jaw crusher and powdered in a porcelain shatter box and then analyzed for a suite of major and trace elements at Activation Laboratories, Ltd. in Ancaster, Ontario. The ferrous iron concentration in five samples and two standards (SY-4 and QLO-1) was measured by the Wilson (1960) titration method; the titrated values of wt% FeO for SY-4 (3.03 ± 0.07) and QLO-1 (2.98 ± 0.08) are close to certified values (2.86 ± 0.09 , and 2.97 ± 0.05 , respectively). The whole-rock major elements are presented in Table 2.1, along with Ba and Sr concentrations. Analyses of all trace elements are presented in the Appendix (Table A1). In Table 2.1, the compositional difference between the highly-evolved rhyolite (TEQ-21) and the five less-evolved rhyolites is apparent, with much lower concentrations of CaO, MgO, Ba and Sr in TEQ-21, despite an overlap in concentration of SiO₂.

All six rhyolites share five mineral phases (plagioclase + orthopyroxene + titanomagnetite + ilmenite + apatite). The five less-evolved rhyolites contain up to three additional mineral phases (\pm hornblende \pm zircon \pm pyrrhotite), whereas the highly-evolved rhyolite (TEQ-21) also contains zircon along with two additional phenocrysts (sanidine + clinopyroxene). Quartz was not found in any of the six obsidian samples. Phenocryst ($>200 \mu\text{m}$) and microphenocryst ($>50 \mu\text{m}$) abundances were determined by

point counts of 2000 to 3000 points across a standard petrographic slide, in triplicate. For this study, no distinction between phenocryst and microphenocryst is made due to the low total crystallinity, and the term phenocryst refers to all grains > 50 μm .

Table 2.1: Whole-rock major element compositions and point counts

Sample	TEQ-21	COMP-3	JAL-10	MLV36	MLV37	MLV45
Lat. (N):	20°51.26'	21°09.79'	21°16.68'	41°36.97'	41°34.28'	41°32.20'
Long. (W):	103°51.86'	104°42.39'	104°41.03'	121°38.48'	121°41.96'	121°43.51'
SiO ₂	74.1	75.2	74.3	73.8	74.5	73.4
TiO ₂	0.15	0.20	0.26	0.27	0.28	0.23
Al ₂ O ₃	13.3	13.5	14.2	13.2	13.6	14.5
FeO ¹	1.62	1.13	1.50	2.08	2.12	1.75
MnO	0.06	0.05	0.06	0.04	0.04	0.04
MgO	0.11	0.30	0.38	0.27	0.28	0.38
CaO	0.51	1.30	1.40	1.23	1.25	1.76
Na ₂ O	4.61	4.55	4.86	3.99	4.00	3.87
K ₂ O	4.83	3.36	3.04	4.18	4.21	3.58
P ₂ O ₅	0.03	0.06	0.07	0.06	0.05	0.04
LOI	0.00	0.70	0.00	0.31	0.40	0.51
Total	99.4	99.7	100.1	99.4	100.7	100.0
Sr (ppm)	24	253	256	105	107	241
Ba (ppm)	132	1141	1134	838	841	851
An-no _{liq}	3.2	7.7	8.3	7.9	8.0	11.6
Mg-no _{liq}	13.0	36.7	40.6	23.3	24.0	35.3
FeO _{FeTi}	1.31	0.95	0.99	1.58	1.58	1.24
FeO _{Titr}	1.30	0.94	0.99	1.55	1.57	-
Plag ph(%)	2.0	1.7	5.4	1.9	2.5	2.4
Opx ph(%)	<0.1	0.3	0.4	0.6	0.8	0.3
Cpx ph(%)	0.1	0.0	0.0	<0.1	0.0	<0.1
Hbl (%)	0.0	0.2	0.2	0.0	0.1	1.3
Fe-Ti Ox (%)	0.6	0.5	0.5	0.3	0.3	0.5
gdms (%)	97.1	97.1	93.6	97.1	96.3	93.8

An-number_{liq} = $[X_{\text{An}} / (X_{\text{An}} + X_{\text{Ab}})] \times 100$, where $X_{\text{An}} = 64.0(X_{\text{CaO}}^{\text{liq}})(X_{\text{Al}_2\text{O}_3}^{\text{liq}})(X_{\text{SiO}_2}^{\text{liq}})^2$ and $X_{\text{Ab}} = 18.963(X_{\text{Na}_2\text{O}}^{\text{liq}})^5(X_{\text{Al}_2\text{O}_3}^{\text{liq}})^5(X_{\text{SiO}_2}^{\text{liq}})^3$ (Lange *et al.*, 2009).

Mg-number_{liq} = $\text{Mg} / (\text{Mg} + \text{Fe}^{2+})_{\text{molar}}$.

¹FeO calculated on basis of ΔNNO value obtained from two Fe-Ti oxides.

²FeO obtained by titration.

ph, phenocrysts (>50 μm); plag, plagioclase; opx, orthopyroxene; cpx, clinopyroxene; hbl, hornblende; Fe-Ti Ox, oxides; gdms, groundmass

Overall, phenocryst abundances are low, ranging from 1.4-6.4%. In all samples, plagioclase is the dominant phase, making up 61-81% of the total phenocryst assemblage. Orthopyroxene is the next most abundant phase in all samples, making up 4-27% of the phenocryst assemblage. Titanomagnetite and ilmenite are ubiquitous and tabulated as

“iron-oxides” without considering size; they occur as mineral inclusions in plagioclase and orthopyroxene (Appendix Fig. A2). Apatite is also ubiquitous and a common mineral inclusion; it is consistently $<50\mu\text{m}$. Hornblende and zircon were each identified in four rhyolites (Table 2.1). Pyrrhotite ($<50\mu\text{m}$ in size) is a trace mineral in COMP-3.

To illustrate the glassy nature of the obsidian samples, with minor amounts of microlites, photomicrographs of three obsidian samples are featured in Fig. 2.1. Next to each photomicrograph is an aluminum element map of an area of groundmass ($600\ \mu\text{m} \times 600\ \mu\text{m}$) within each sample. The Al-element maps show the extent of plagioclase microlite crystallization. JAL-10 has the most microlites, whereas TEQ-21 and MLV-36 have the least.

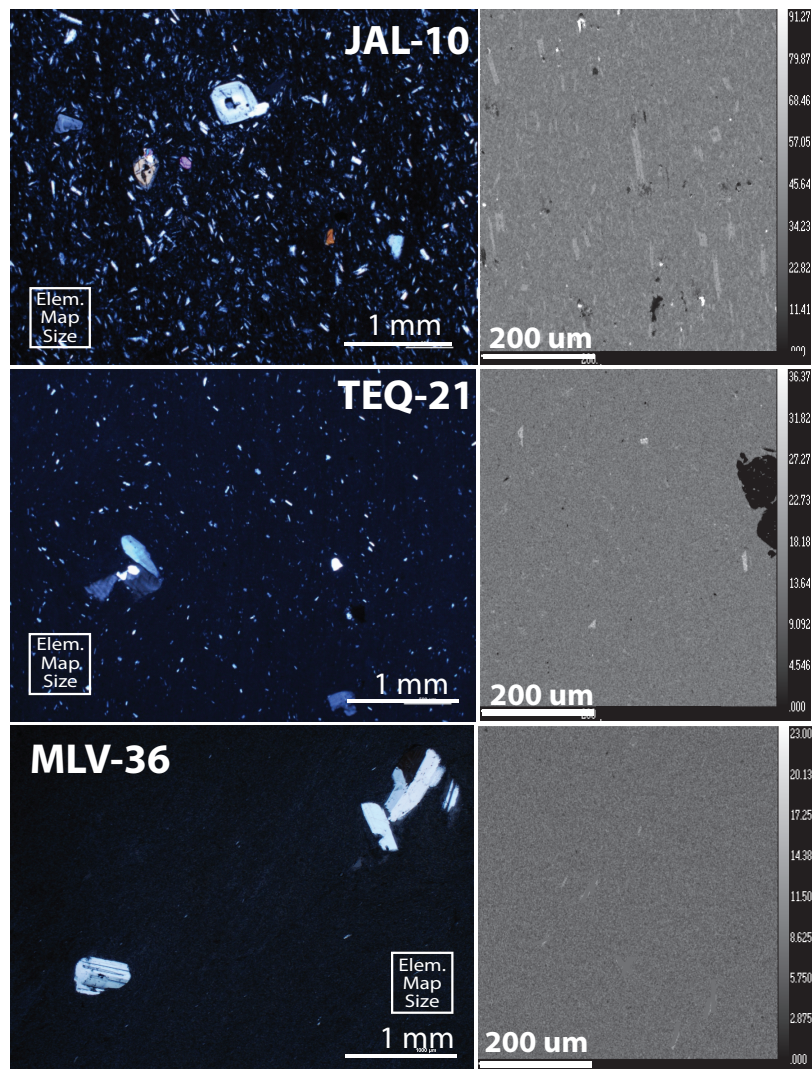


Figure 2.1: Crossed polar photomicrographs (shown on the left) and corresponding aluminum element maps of groundmass (shown on the right) for JAL-10, TEQ-21 and COMP-3. The area of the aluminum element map is shown in the photomicrograph as a white box.

2.5 MINERAL COMPOSITIONS

Analytical Methods

Plagioclase, pyroxene, ilmenite and magnetite were analyzed in each sample with the Cameca SX-100 Electron Microprobe at the University of Michigan. An accelerating voltage of 15 kV was used in all analyses, along with a beam current of 4 nA for

plagioclase and 15 nA for pyroxene, ilmenite, and titanomagnetite. The small size of the ilmenite and titanomagnetite crystals generally limited their analyses to a single point. Rim to rim transects were taken along the long axis of each plagioclase and orthopyroxene phenocryst and microphenocryst. The spacing interval between each analysis along the transects ranged from 5 to 30 μm , depending on the observed zoning and size of each grain. Plagioclase crystals were also analyzed for concentrations of Ba and Sr, using laser ablation inductively coupled plasma mass spectroscopy (LA-ICP-MS) at Oregon State University. For analyses of Sr and Ba, plagioclase crystals were analyzed with a beam spot size of 50 μm and calibrated using ^{43}Ca , while monitoring standards BHVO-2G and two separate standards of BCR-2G.

Analytical Results

Within each sample, the ilmenite and titanomagnetite analyses have a small range in composition (Table 2.2). Analyses of individual crystals of titanomagnetite and ilmenite for each sample are reported in the Appendix (Tables A2 and A3, respectively). A plot of $\log (X_{\text{Mg}}/X_{\text{Mn}})_{\text{magnetite}}$ vs $\log (X_{\text{Mg}}/X_{\text{Mn}})_{\text{ilmenite}}$ for all possible magnetite-ilmenite pairs in each sample is included in the Appendix (Fig. A3); no pairs deviate strongly from the test of equilibrium proposed by Bacon and Hirshmann (1988).

Table 2.2: Average Compositions of Fe-Ti Oxides

Sample:	TEQ-21	COMP-3	JAL-10	MLV-36	MLV-37	MLV-45
Phase:	IL	IL	IL	IL	IL	IL
No. of Analyses	17	8	11	21	15	14
SiO ₂	0.02	0.06	0.04	0.04	0.10	0.03
TiO ₂	47.29	37.78	40.13	45.82	45.57	42.7
Al ₂ O ₃	0.17	0.32	0.41	0.25	0.16	0.40
Fe ₂ O ₃	11.83	31.06	27.01	16.19	15.43	22.7
V ₂ O ₃	0.36	0.09	0.06	0.47	0.47	0.34
Cr ₂ O ₃	0.01	0.02	0.02	0.06	0.05	0.03
FeO	37.10	27.24	29.24	33.93	35.18	31.0
MnO	0.85	0.74	0.78	0.58	0.63	0.59
MgO	1.54	2.47	2.35	2.41	1.82	2.22
CaO	0.06	0.05	0.02	0.03	0.02	0.14
Total	99.24	99.83	100.05	99.79	99.43	100.2
X _{ilmenite}	81.1	59.7	64.1	74.5	77.2	69.1
$\pm 1\sigma$ X _{ilmenite}	2.3	2.0	1.1	1.1	0.1	0.1
Phase:	MT	MT	MT	MT	MT	MT
No. of Analyses	7	10	4	8	4	8
SiO ₂	0.07	0.07	0.12	0.9	0.17	0.12
TiO ₂	17.6	5.67	5.68	10.7	9.41	7.41
Al ₂ O ₃	1.74	2.23	2.36	2.19	1.98	2.55
Fe ₂ O ₃	32.9	56.2	56.0	44.8	47.6	52.1
V ₂ O ₃	0.30	0.28	0.19	1.07	0.32	0.44
Cr ₂ O ₃	0.02	0.03	0.02	0.13	0.15	0.18
FeO	45.3	33.9	34.4	38.9	37.3	36.4
MnO	0.71	0.64	0.66	0.47	0.49	0.39
MgO	1.07	1.58	1.30	1.42	1.17	1.27
CaO	0.02	0.01	0.02	0.03	0.10	0.02
Total	99.7	100.6	100.5	99.9	98.7	100.5
X _{ulvospinel}	49.3	15.9	15.9	30.4	26.8	20.6
$\pm 1\sigma$ X _{ulvospinel}	1.8	1.1	1.8	0.3	3.3	2.0
T(°C)	940 ± 18	801 ± 8	779 ± 25	852 ± 12	813 ± 10	837 ± 20
Δ NNO	-0.4 ± 0.1	1.4 ± 0.1	1.4 ± 0.1	0.3 ± 0.1	0.4 ± 0.1	0.9 ± 0.1

Temperature and Δ NNO are average ($\pm 1\sigma$) from all possible pairings of ilmenite and titanomagnetite analyses using model of Ghiorso & Evans (2008).

A compositional traverse was taken along the long axis of each plagioclase grain within a thin section for each sample. Analyses from the plagioclase traverses are available in the Appendix (Table A4) and a subset is shown in Table 2.3. In Fig. 2.2, the

range in mol% An in a single crystal is shown as a function of length. No correlation is observed with phenocryst length and An content. The entire set of compositional traverses of plagioclase from sample MLV-36 illustrate that normal, reverse and no zoning all coexist (Appendix Fig. A4). The data in Figs. 2.2 and Fig. A4 show the compositional range for all plagioclase analyses in an entire sample is larger than that observed in a single crystal.

Table 2.3: Analyses of Minimum and Maximum % An Plagioclase

	TEQ	TEQ	COMP	COMP	JAL	JAL	MLV	MLV	MLV	MLV	MLV	MLV
Sample:	21	21	3	3	10	10	36	36	37	37	45	45
ph:	ph	ph	ph	ph	ph	ph	ph	ph	ph	ph	ph	ph
SiO ₂	64.5	69.0	54.9	57.8	55.5	66.8	56.1	60.6	53.2	62.6	50.6	59.7
Al ₂ O ₃	22.4	17.6	28.9	26.5	28.1	20.8	28.0	24.7	29.4	23.0	31.4	25.1
Fe ₂ O ₃	0.13	0.76	0.24	0.21	0.42	0.28	0.26	0.31	0.54	0.26	0.63	0.60
CaO	3.47	1.09	10.9	7.04	10.7	4.64	10.4	6.65	12.3	5.16	14.3	7.14
Na ₂ O	8.56	6.92	5.34	7.05	4.93	6.33	5.12	7.22	4.40	7.67	4.56	7.33
K ₂ O	1.62	4.08	0.22	0.43	0.22	0.98	0.31	0.73	0.26	1.02	0.11	0.56
Sum	100.2	99.7	100.3	99.3	100.3	100.1	99.1	100.3	100.1	100.0	100.5	100.5
<i>Anion normalization</i>												
Si	2.84	3.05	2.47	2.60	2.50	3.03	2.52	2.69	2.41	2.80	2.29	2.66
Al	1.16	0.92	1.53	1.41	1.49	1.11	1.48	1.30	1.57	1.21	1.68	1.32
Fe ³⁺	0.00	0.03	0.01	0.01	0.01	0.01	0.01	0.01	0.02	0.01	0.02	0.03
Ca	0.16	0.05	0.51	0.34	0.52	0.23	0.52	0.32	0.60	0.25	0.70	0.34
Na	0.73	0.59	0.47	0.62	0.43	0.63	0.44	0.62	0.40	0.67	0.30	0.63
K	0.09	0.23	0.01	0.03	0.01	0.06	0.02	0.04	0.00	0.06	0.01	0.03
<i>No. of</i>												
<i>Cations</i>	4.99	4.89	5.01	5.01	4.97	4.82	4.98	4.98	4.99	4.97	5.01	5.00
X _{An}	0.17	0.06	0.51	0.34	0.54	0.27	0.53	0.32	0.60	0.25	0.70	0.34
X _{Ab}	0.74	0.68	0.48	0.62	0.45	0.66	0.45	0.63	0.39	0.66	0.30	0.63
X _{Or}	0.09	0.26	0.01	0.03	0.01	0.07	0.02	0.04	0.01	0.06	0.01	0.03
An%	16.6	5.9	51.9	34.6	53.8	26.8	52.7	32.3	60.0	24.6	69.1	33.9
wt% H ₂ O	2.6	2.2	5.9	5.3	6.5	5.5	4.5	3.8	5.6	4.3	5.8	4.4

Ph, phenocrysts; Water concentrations are calculated with the hygrometer of Lange *et al.* (2009) and the calibration of Lange *et al.* 2012 and Waters *et al.* 2012 (See text for more details).

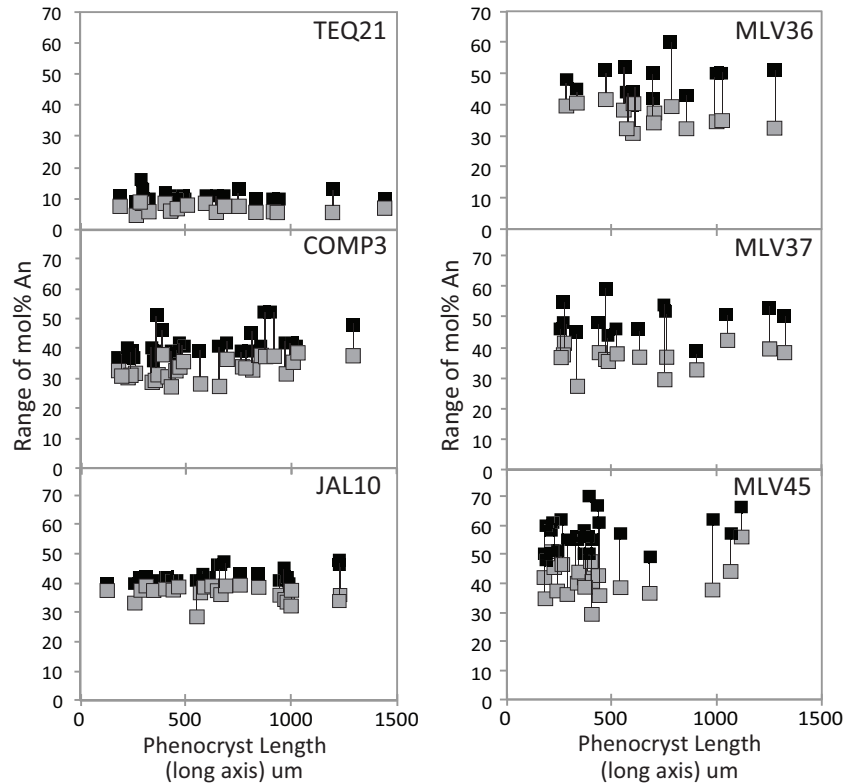


Figure 2.2: Plots of plagioclase length (long axis) by range in mol% An for all measured grains in each rhyolite. Maximum mol% An observed in a phenocryst is shown with a black square and connected to the minimum mol% An, a grey square, with a black line. Phenocryst length is not correlated with the range in mol% An observed (i.e. the largest range in mol% An is not found in the largest phenocryst). The entire data set spans a greater range in mol% An than is observed in a single grain.

Histograms of plagioclase compositions for phenocrysts (grey) and microlites (black) are shown as a function of mol% anorthite (An) for each sample (Fig. 2.3). Microlites make up all analyzable crystals less than 50 μm . In each sample, the microlite population, where present, is consistently more sodic than the phenocryst population. The plagioclase phenocrysts in the highly evolved rhyolite (TEQ-21) are sodic, $\text{An}_{17}\text{-An}_6$, with a peak at 9 mol% An. For the less-evolved rhyolites, the majority of the plagioclase phenocrysts range between $\sim\text{An}_{55}\text{-An}_{30}$, with a peak in the mid-range. In some rhyolites, a population of calcic plagioclase (up to An_{89}) was observed, separated by a gap from the most abundant compositional range (Fig. 2.3).

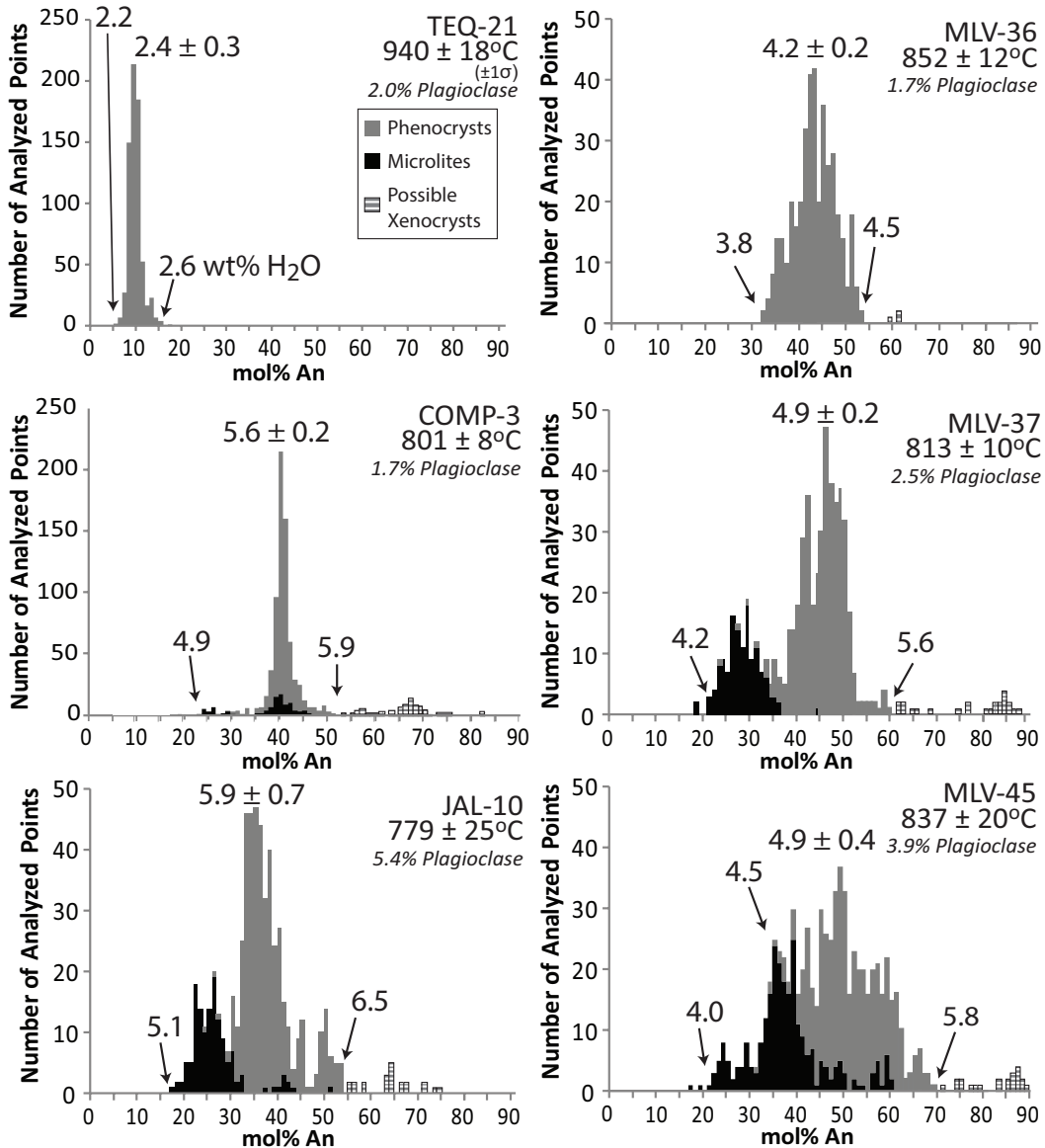


Figure 2.3: Histograms of plagioclase phenocrysts (in grey), microlites (in black), and possible xenocrysts (in hatched pattern) as a function of mol% An. Microlites (absent in TEQ-21 and MLV-36) are consistently more sodic than phenocrysts. Possible xenocrysts, determined by comparison with phase-equilibrium experiments (see text), were found in all samples except in TEQ-21. Also shown are melt wt% H₂O values calculated with the plagioclase-liquid hygrometer model of Lange et al. (2009) recalibrated for rhyolites (Lange et al. 2012; Waters et al. 2012). The errors shown next to the peak water contents are calculated by applying the one-sigma errors on the pre-eruptive temperatures (derived from the two iron oxide geothermometer) to the temperatures used in the plagioclase-liquid hygrometer.

Orthopyroxene crystals, like plagioclase, span a wide range of composition in each sample. Compositional traverses were taken along the long axis of each orthopyroxene grain and are presented in the Appendix (Table 5A) and a subset is shown

in Table 2.4. Often, the entire range of orthopyroxene compositions in a sample, as a function of Mg#, is much greater than the range of compositions observed in a single crystal (Appendix Fig. A4). The Mg# of orthopyroxene is calculated using the concentrations of MgO and FeO^T from the microprobe analyses, where all FeO is considered to be ferrous. The change in Mg# that results when considering small amounts of Fe³⁺ that may be present in the orthopyroxene structure is addressed in the following section on ^{Fe-Mg}K_D. Histograms of orthopyroxene composition as a function of Mg# are presented for each sample in Fig. 2.4. The orthopyroxene crystals in the highly evolved rhyolite (TEQ-21) have a narrow range in Mg# (45-46), whereas those in the less evolved rhyolites span a wide range in Mg# (51-76).

Table 2.4: Analyses of minimum and maximum Mg-number orthopyroxene

Sample	TEQ 21	TEQ 21	COMP 3	COMP 3	JAL 10	JAL 10	MLV 36	MLV 36	MLV 37	MLV 37	MLV 45	MLV 45
ph/mph	mph	mph	mph	ph	ph	ph	ph	mph	ph	ph	ph	ph
SiO ₂	49.4	49.8	53.7	51.9	51.5	57.4	50.0	52.1	50.2	51.8	51.3	52.0
TiO ₂	0.11	0.11	0.13	0.12	0.07	0.10	0.16	0.09	0.14	0.15	0.08	0.21
Al ₂ O ₃	0.30	0.34	1.74	1.55	0.55	3.22	0.41	0.54	0.50	3.62	0.28	1.71
FeO	31.4	30.9	19.2	18.9	22.2	15.9	29.4	23.5	29.2	15.7	26.5	18.0
MnO	2.36	2.24	1.23	1.27	1.98	1.12	0.88	0.81	0.90	0.25	1.17	0.87
MgO	14.2	14.6	22.5	25.3	22.4	20.9	17.2	21.6	17.5	26.2	19.5	25.0
CaO	1.40	1.37	0.59	0.54	0.52	0.60	1.01	0.87	0.93	1.17	0.70	1.15
Sum	99.3	99.5	99.1	99.7	100.7	99.3	99.5	98.9	99.1	99.5	99.3	99.3
<i>Cation sum=4, O=6</i>												
Si	1.95	1.97	2.00	1.90	1.93	2.10	1.95	1.96	1.95	1.88	1.96	1.92
Al (IV)	0.05	0.03	0.00	0.10	0.07	0.00	0.05	0.04	0.05	0.12	0.04	0.08
Al (VI)	0.00	0.00	0.08	0.00	0.00	0.14	0.00	0.00	0.00	0.03	0.00	0.00
Ti	0.00	0.00	0.00	0.00	0.00	0.00	0.00	0.00	0.00	0.00	0.00	0.01
Fe ³⁺												
(VI)	0.08	0.05	0.00	0.13	0.11	0.00	0.08	0.05	0.08	0.07	0.06	0.08
Fe ²⁺	0.95	0.97	0.60	0.45	0.59	0.49	0.88	0.69	0.87	0.41	0.78	0.47
Mn	0.08	0.07	0.04	0.04	0.06	0.03	0.03	0.03	0.03	0.01	0.04	0.03
Mg	0.84	0.86	1.25	1.38	1.26	1.14	1.00	1.21	1.01	1.42	1.11	1.37
Ca	0.06	0.06	0.02	0.02	0.02	0.02	0.04	0.03	0.04	0.05	0.03	0.05
Fe ²⁺ /Fe ^T	0.92	0.95	1.00	0.88	0.85	1.00	0.91	0.94	0.92	0.85	0.93	0.85
Mg-no.	46.7	47.0	67.6	75.3	68.0	70.1	53.3	63.7	53.8	77.7	58.6	74.4
KD	0.17	0.17	0.27	0.21	0.32	0.29	0.27	0.17	0.27	0.09	0.39	0.19
<i>All Fe²⁺</i>												
Mg-no.	44.6	45.7	67.6	70.5	64.3	70.1	51.1	62.2	51.7	74.8	56.7	71.2
KD	0.19	0.18	0.27	0.23	0.38	0.29	0.29	0.18	0.30	0.11	0.42	0.22

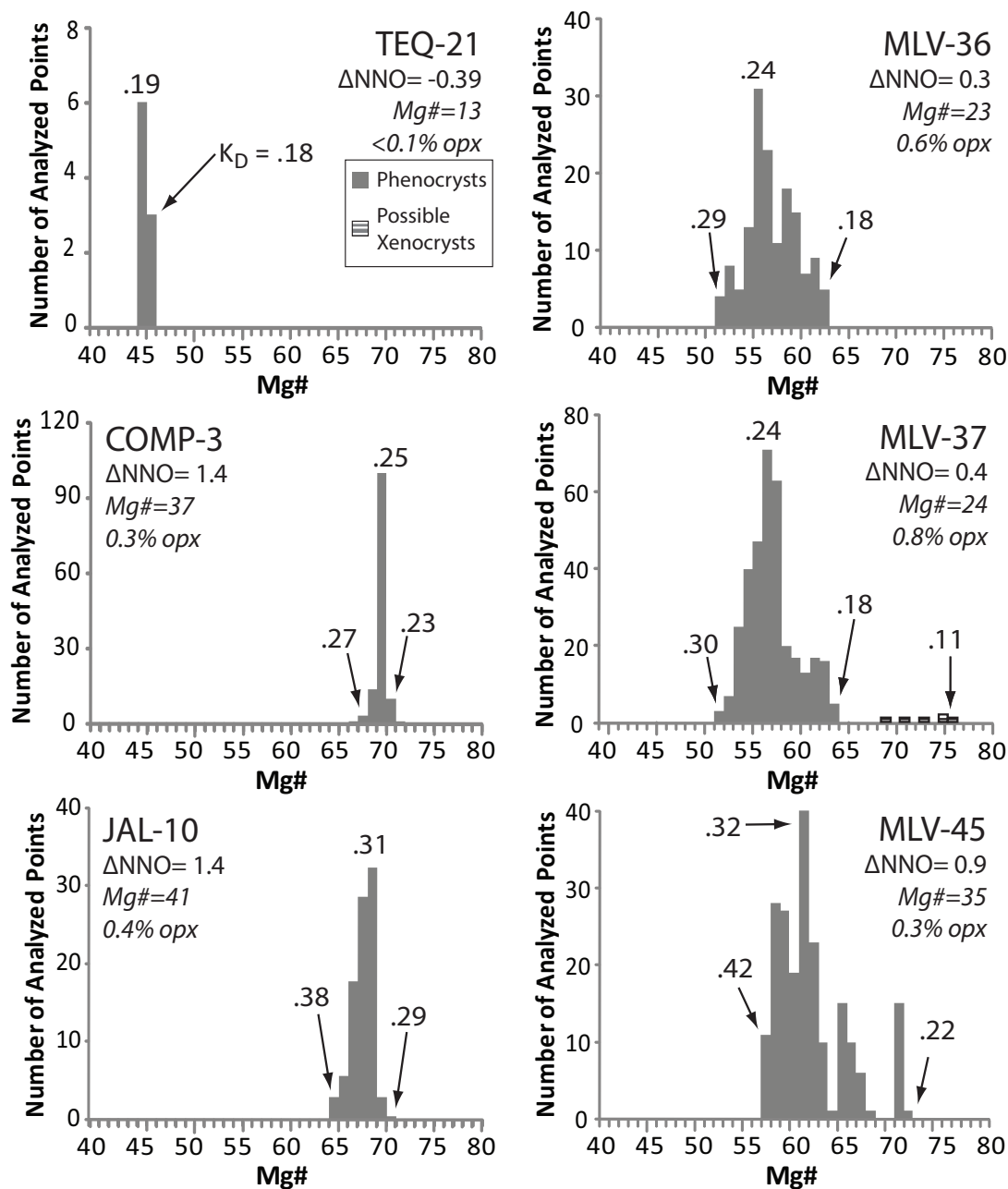


Figure 2.4: Histograms of orthopyroxene phenocryst (grey) compositions, as a function of Mg# with corresponding $Fe-Mg K_D$ values between orthopyroxene and liquid. The liquid Fe^{2+} concentration (wt% FeO) is derived from ΔNNO values obtained from two Fe-Ti oxide oxygen barometry and closely matches measurements by titration (Table 2.1) (see text for discussion).

Analyzed Ba and Sr concentrations in plagioclase and the Ba and Sr partition coefficients between plagioclase crystals and liquid for three rhyolites (TEQ-21, COMP-

3 and JAL-10) are presented in Table 2.5. Partition coefficients for barium and strontium were calculated using the following equations:

$$D_{Ba} = \frac{Ba(ppm)^{plagioclase}}{Ba(ppm)^{liquid}} \quad , \quad D_{Sr} = \frac{Sr(ppm)^{plagioclase}}{Sr(ppm)^{liquid}} \quad (\text{Equation 2.1})$$

The partition coefficients were calculated by taking into account the changing Ba and Sr liquid concentrations due to the sparse phenocryst growth of plagioclase (Table 2.5). Equilibrium crystallization and fractional crystallization were modeled, beginning with the most calcic plagioclase, and the results of both calculations are presented in the Appendix (Table A6). Because the most calcic plagioclase in each sample is the near-liquidus phase, whole-rock concentrations for Ba and Sr can be used for the liquid concentrations at the beginning of this calculation. The abundance (percent crystals) of plagioclase used at each step of the calculation was determined by multiplying total plagioclase abundance (Table 2.1) by the percent of plagioclase crystallized at a given mol% An from in the histogram in Fig. 2.3. The changing Ba and Sr concentrations in the liquid, driven by removal of the relatively more calcic plagioclase, were used to calculate D_{Ba} and D_{Sr} for the progressively more sodic plagioclase. The model results for both equilibrium and fractional crystallization are presented in the Appendix (Table A6). At the low phenocryst abundances in these samples, there is little difference between the two end-member crystallization models. However, because diffusive re-equilibration of plagioclase is slow, the fractional crystallization model is used to calculate the Ba and Sr liquid concentrations for the partition coefficients listed in Table 2.5. All analyzed trace element concentrations are provided in the Appendix (Table A7).

Table 2.5: Sr and Ba analyses in plagioclase

TEQ-21								COMP-3								JAL-10								
X _{An}	% xtl	Ba ^{plag} (ppm)	Sr ^{plag} (ppm)	Ba ^{liq} (ppm)	D _{Ba}	Sr ^{liq} (ppm)	D _{Sr}	X _{An}	% xtl	Ba ^{plag} (ppm)	Sr ^{plag} (ppm)	Ba ^{liq} (ppm)	D _{Ba}	Sr ^{liq} (ppm)	D _{Sr}	X _{An}	% xtl	Ba ^{plag} (ppm)	Sr ^{plag} (ppm)	Ba ^{liq} (ppm)	D _{Ba}	Sr ^{liq} (ppm)	D _{Sr}	
									0.00															
12.7	0.07	2777	520	130	21.3	24	22.0	57.4	1	187	1814	1141	0.16	253	7.17	50.7	0.09	300	1724	1135	0.26	255	6.77	
12.5	0.07	3248	578	130	24.9	24	24.4	41.4	0.41	371	1638	1145	0.32	247	6.64	50.3	0.09	245	1686	1136	0.22	253	6.65	
11.9	0.05	1486	341	129	11.5	23	14.6	40.6	0.41	398	1441	1148	0.35	241	5.98	49.9	0.09	270	1727	1136	0.24	253	6.82	
11.5	0.05	1983	393	129	15.4	23	16.8	40.6	0.41	545	1670	1148	0.47	241	6.93	49.4	0.09	295	1773	1136	0.26	252	7.03	
10.5	0.15	1431	332	126	11.4	23	14.5	40.6	0.41	350	1589	1148	0.30	241	6.59	45.4	0.08	277	1677	1137	0.24	251	6.69	
9.6	0.54	2337	335	119	19.6	21	15.8	40.4	0.53	366	1654	1152	0.32	234	7.07	44.7	0.08	279	1498	1137	0.25	251	5.97	
9.6	0.54	2645	388	119	22.2	21	18.3	40.4	0.53	384	1519	1152	0.33	234	6.49	44.7	0.08	285	1606	1137	0.25	251	6.40	
9.5	0.54	3528	371	119	29.6	21	17.5	40.1	0.53	367	1448	1152	0.32	234	6.19	42.1	0.29	785	1628	1139	0.69	247	6.59	
9.5	0.54	3429	460	119	28.8	21	21.7	39.7	0.53	412	1539	1152	0.36	234	6.58	40.8	0.43	394	1482	1141	0.35	241	6.15	
9.4	0.62	2817	343	100	28.1	19	18.4	39.7	0.53	429	1539	1152	0.37	234	6.58	40.7	0.43	363	1427	1141	0.32	241	5.92	
9.2	0.62	3054	362	100	30.5	19	19.4	39.7	0.53	402	1531	1152	0.35	234	6.54	40.6	0.43	434	1493	1141	0.38	241	6.19	
9.1	0.62	2621	345	100	26.2	19	18.5	39.6	0.53	377	1476	1152	0.33	234	6.31	40.5	0.43	415	1442	1141	0.36	241	5.98	
9.1	0.62	4005	379	100	40.0	19	20.3	39.5	0.53	387	1500	1152	0.34	234	6.41	39	0.55	724	1565	1145	0.63	235	6.67	
9	0.62	1929	365	100	19.2	19	19.5	39.4	0.22	641	1819	1154	0.56	231	7.87	38.8	0.55	554	1485	1145	0.48	235	6.33	
8.9	0.62	3773	378	100	37.7	19	20.2	39.3	0.22	382	1513	1154	0.33	231	6.54	38.4	0.37	348	1366	1147	0.30	230	5.94	
8.9	0.62	2099	286	100	20.9	19	15.3	39.3	0.22	471	1720	1154	0.41	231	7.44	36.7	0.5	508	1334	1151	0.44	224	5.95	
8.8	0.62	2162	284	100	21.6	19	15.2	38.8	0.22	325	1655	1154	0.28	231	7.16	36.5	0.57	401	1309	1151	0.35	224	5.84	
8.8	0.62	3674	342	100	36.7	19	18.3	38.6	0.22	384	1489	1154	0.33	231	6.44	36.3	0.57	662	1386	1155	0.57	218	6.35	
8.8	0.62	2314	291	100	23.1	19	15.6	38.6	0.22	383	1491	1154	0.33	231	6.45	36.3	0.57	610	1432	1155	0.53	218	6.56	
8.6	0.62	3801	363	100	37.9	19	19.4	38.4	0.08	394	1461	1155	0.34	230	6.35	36	0.57	568	1298	1155	0.49	218	5.95	
8.6	0.62	1481	283	100	14.8	19	15.1	38.3	0.08	380	1424	1155	0.33	230	6.19	36	0.57	483	1339	1155	0.42	218	6.14	
8.2	0.43	2753	307	94	29.2	18	17.5	37.6	0.08	303	1744	1155	0.26	230	7.58	35.8	0.57	492	1298	1155	0.43	218	5.95	
8.1	0.43	2315	294	94	24.5	18	16.7	36.4	0.03	441	1504	1155	0.38	230	6.55	35.8	0.57	505	1340	1155	0.44	218	6.14	
7.7	0.43	2429	271	94	25.7	18	15.4								35.7	0.57	591	1399	1155	0.51	218	6.41		
7.4	0.08	2489	296	93	26.9	17	17.0								35.4	0.48	483	1360	1158	0.42	213	6.40		
6.1	0.02	1363	220	92	14.8	17	12.7								35.2	0.48	517	1364	1158	0.45	213	6.42		
															34.6	0.48	517	1328	1158	0.45	213	6.25		
															33.3	0.22	420	1219	1160	0.36	210	5.80		

35

X_{An}=mol fraction anorthite in plagioclase; %xtal= percentage of plagioclase crystallized from the melt; Ba^{plag} (ppm) and Sr^{plag} (ppm) are the concentrations in plagioclase measured by LA-ICPMS. D_{Ba} and D_{Sr} are the Ba and Sr partition coefficients modeled with Rayleigh crystal fractionation using the liquid compositions (Ba^{liq} and Sr^{liq}). See text for more detail.

Temperature and Oxygen Fugacity

Temperature and oxygen fugacity (reported as ΔNNO : $\log_{10}f\text{O}_2$ relative to the $\log_{10}f\text{O}_2$ of the Ni-NiO buffer at a given temperature) were obtained by applying the two Fe-Ti oxide geothermometer and oxybarometer model of Ghiorso and Evans (2008) to all possible pairs of titanomagnetite and ilmenite analyses in each sample. The results of all possible pairings are shown as plots of ΔNNO vs. temperature for each sample in the Appendix (Fig. A5). Temperatures ($\pm 1\sigma$) range from 779 ± 25 (JAL-10) to 940 ± 18 °C (TEQ-21) and ΔNNO values ($\pm 1\sigma$) range from -0.4 ± 0.1 (TEQ-21) to 1.4 ± 0.1 (COMP-3; JAL-10)(Table 2.2). The four samples that contain hornblende have the lowest temperatures (≤ 837 °C). Values of wt% FeO were calculated using the temperature and ΔNNO from the Fe-Ti oxides into the equation of Kress and Carmichael (1991); the calculated values match those measured by titration (Table 2.1).

Calculation of K_D values for orthopyroxene and liquid

The orthopyroxene and liquid (whole-rock) compositions can be used to calculate $^{\text{Fe-Mg}}K_D$ values between orthopyroxene and liquid, using the following equation:

$$^{\text{Fe-Mg}}K_{D_{\text{opx-liq}}} = \left(\frac{X_{\text{Mgo}}}{X_{\text{FeO}}} \right)^{\text{liquid}} \left(\frac{X_{\text{FeO}^{\text{T}}}}{X_{\text{MgO}}} \right)^{\text{crystal}} \quad (\text{Equation 2.2})$$

The concentration of ferrous iron in each liquid (X_{FeO}), based on the calculated ΔNNO value derived from the two Fe-Ti oxybarometer (Table 2.1), was used for all calculations of $^{\text{Fe-Mg}}K_D$. The concentrations of FeO and MgO in orthopyroxene were those obtained from the electron microprobe analyses. The Fe^{3+} concentration in the orthopyroxenes was calculated based on stoichiometry, and the $^{\text{Fe-Mg}}K_D$ values that result (0.09-0.39) are presented in Table 2.4. Because the majority of the $^{\text{Fe-Mg}}K_D$ values

reported in the literature for orthopyroxene are based without considering concentrations of Fe^{3+} (i.e. total iron as Fe^{2+}) in the mineral phase, these values are also reported in this study (0.11-0.42; Table 2.4 and Fig. 2.4).

2.6 TESTS TO DISTINGUISH PHENOCRYSTS VS. XENOCRYSTS

Comparison with Phase-Equilibrium Experiments

The wide ranges of plagioclase and orthopyroxene compositions in each sample were compared to mineral compositions found in phase-equilibrium experiments in the literature to evaluate whether some of the plagioclase and/or orthopyroxene in each sample are xenocrystic.

Plagioclase

Three fluid-saturated experimental studies on natural rhyolites at upper crustal conditions were used to evaluate a possible xenocryst origin for some of the plagioclase crystals in each sample. Coombs and Gardner (2001), Couch et al. (2003), and Tomiya et al. (2010) conducted experiments on rhyolite liquids with An#s (defined in Table 2.1) of 5, 27 and 10, respectively. The results of the phase-equilibrium experiments are shown in a plot of plagioclase composition (mol% An) vs. the An# of the experimental liquid (Fig. 2.5). Also shown are the experimental data used to calibrate the plagioclase-liquid hygrometer of Lange et al. (2009), but only for liquids with An#s ≤ 30 (felsic compositions). The phase-equilibrium data show that a wide range of plagioclase compositions (spanning ~ 20 mol% An) can form in each liquid at a given An#, with more calcic plagioclase forming at higher temperatures and/or higher melt water concentrations. Additionally, the An# of the rhyolite liquid controls the range of

equilibrium plagioclase that can form, with more calcic plagioclase forming in liquids with higher An#s.

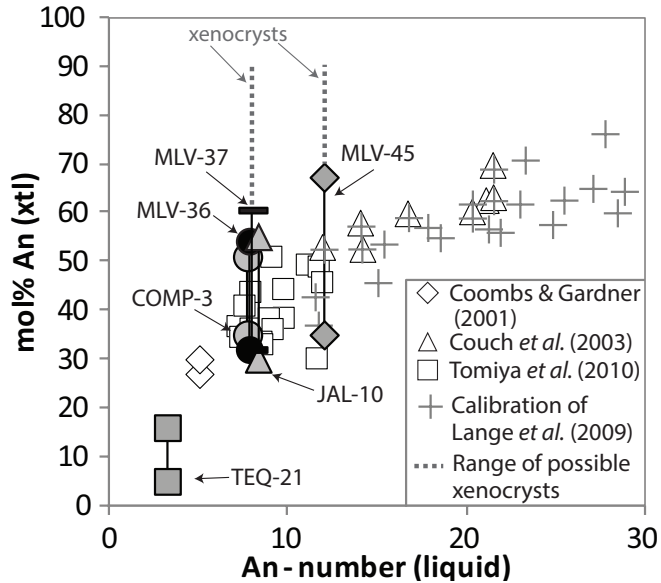


Figure 2.5: A plot of analyzed plagioclase compositions (mol% An) in the six obsidian samples as a function of the An# of the liquid (defined in Table 2.1) with a range of possible xenocrysts shown as a dashed grey line (see text for criteria for distinguishing xenocrysts). Also shown are plagioclase compositions (mol% An) crystallized in the phase-equilibrium experiments of Coombs and Gardner (2001) (open diamonds), Couch et al. (2003) (open triangles) and Tomiya et al. (2010) (open squares). Grey crosses show a subset of the experimental data, liquids with An#s <30, used to calibrate the plagioclase-liquid hygrometer of Lange et al. (2009). The experiments show that a range of equilibrium plagioclase compositions spanning 20 mol% An can crystallize out of a single liquid, with the more calcic plagioclase forming at higher temperatures and/or water contents. Liquids with higher An#s crystallize more calcic plagioclase than liquids with lower An#s.

Four of the six rhyolites in this study have liquid An#s that cluster around eight and overlap the An#s of the experimental glasses in the study of Tomiya et al. (2010) (Fig. 2.5). The most calcic plagioclase in the experiments of Tomiya et al. (2010) is An₅₁, which is the minimum cut-off for plagioclase compositions that are plausible phenocrysts in the four rhyolites with An#s of eight. The observed distribution of plagioclase compositions is also used as a guide, and the cut-off between phenocrysts and xenocrysts is taken at the first compositional gap in the analyzed plagioclase compositions (~An₅₅-An₆₀). Plagioclase crystals that are probable xenocrysts are shown

as a hatch pattern in the histograms in Fig. 2.3 and are removed in Fig. 2.5. Sample MLV-45 has a relatively high An# of 12, and therefore the range of plausible phenocrysts for this sample extends to $\leq \text{An}_{70}$. The more calcic plagioclase crystals in this sample (ranging up to An_{89}) are considered possible xenocrysts and are shown with a hatched pattern in Fig. 2.3.

Orthopyroxene

In order to compare the range of orthopyroxene compositions with the results of phase-equilibrium experiments, only those studies where oxygen fugacity was buffered and/or monitored can be used, so that the ferric-ferrous ratio in the liquid is known. All three of the fluid-saturated phase-equilibrium experiments on natural rhyolites were buffered at or near $\sim \text{Ni-NiO}$, but only Coombs and Gardner (2001) and Tomiya et al. (2010) report orthopyroxene compositions; the resultant $^{\text{Fe-Mg}}K_D$ values between orthopyroxene and liquid range from 0.16-0.17 and 0.31-0.71, respectively. These experimentally obtained $^{\text{Fe-Mg}}K_D$ values are plotted as a function of liquid Mg# in Fig. 2.6, along with those obtained for orthopyroxene in dacite and andesite liquids from various fluid-saturated phase-equilibrium experiments in the literature (Gardner et al. 1995; Blatter and Carmichael 1998, 2001; Moore and Carmichael 1998; Martel et al. 1999; Scaillet and Evans 1999; Pichavant et al. 2002; Grove et al. 2003; Costa et al. 2004; Holtz et al. 2005).

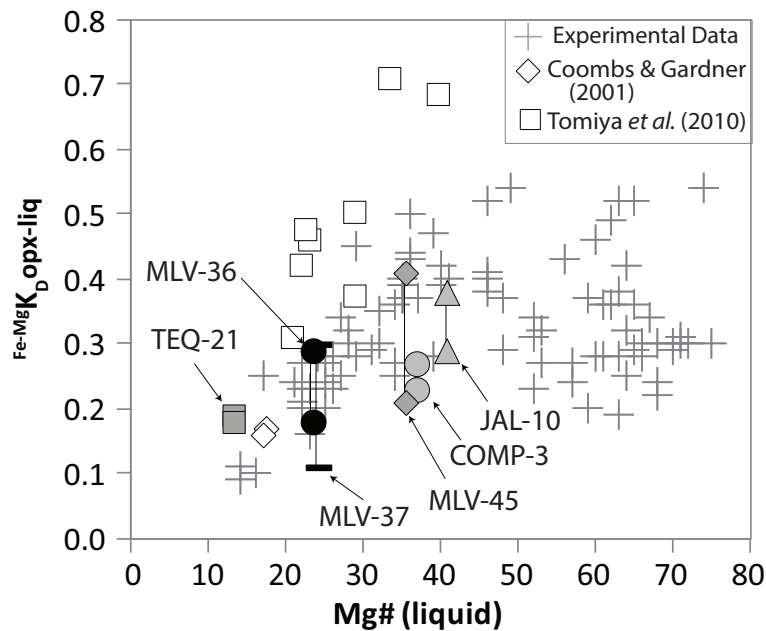


Figure 2.6: A plot of the range of $^{Fe-Mg}K_D$ values between orthopyroxene and liquid for the six obsidian samples. The $^{Fe-Mg}K_D$ values between orthopyroxene and liquid from the experiments of Coombs and Gardner (2001) (open diamonds) and Tomiya et al. (2010) (open squares) are also shown. Grey crosses show $^{Fe-Mg}K_D$ values obtained from orthopyroxene crystallized in water-saturated andesite and dacite liquids from experiments in the literature, where oxygen fugacity was rigorously controlled or monitored (see text).

For all six rhyolites, the range of $^{Fe-Mg}K_D$ values between orthopyroxene and liquid broadly overlap the experimental values shown in Fig. 2.6, consistent with a phenocryst origin for the full range of orthopyroxene compositions in each sample. The one exception is seen in MLV-37, for which the most Mg-rich orthopyroxenes ($Mg\#s = 70-76$) have unusually low $^{Fe-Mg}K_D$ values of 0.13-0.11, given the bulk liquid $Mg\#$ of 24. These magnesian orthopyroxenes are therefore plausible xenocrysts and are shown with a hatched pattern in Fig. 2.4.

Ba and Sr Partitioning

Another test of a phenocryst vs. xenocryst origin for plagioclase can be made with Ba and Sr partition coefficients between plagioclase and liquid. Blundy and Wood

(1991), Bindeman et al. (1988), and Bindeman and Davis (2000) present model equations, based on natural and experimental data, for determining $RT\ln(D_{Ba})$ and $RT\ln(D_{Sr})$ as a function of mol% An in plagioclase. Measured partition coefficients for Ba and Sr between plagioclase and liquid for three samples from this study (TEQ-21, COMP-3, and JAL-10) are shown in Table 2.5. These data are combined with temperatures obtained with from the Fe-Ti oxides (Table 2.2) to plot values of $RT\ln(D_{Ba})$ and $RT\ln(D_{Sr})$ as a function of mol% An in Fig. 2.7.

The results for JAL-10 and COMP-3 on phenocrystic plagioclase crystals (according to the data in Figs. 2.3 and 2.5) overlap the data set used to calibrate the model of Blundy and Wood (1991), which further supports a phenocryst origin for this compositional range of plagioclase. However, the results on the more calcic plagioclase crystals (An_{70} - An_{57}) in COMP-3 are offset from the data set used by Blundy and Wood (1991), consistent with a xenocryst origin for this calcic population. Interestingly, these same calcic crystals show correspondence with the data set used to calibrate the Blundy and Wood (1991) model for the partitioning of Ba, which suggests that Ba is less useful than Sr as a diagnostic tool for identifying xenocrysts. The sodic plagioclase crystals (An_6 - An_{13}) in the highly-evolved rhyolite (TEQ-21) have corresponding $RT\ln D_{Sr}$ and $RT\ln D_{Ba}$ values that are broadly consistent with the model equations of Blundy and Wood (1991), although there are few experimental data for sodic plagioclase ($<An_{30}$).

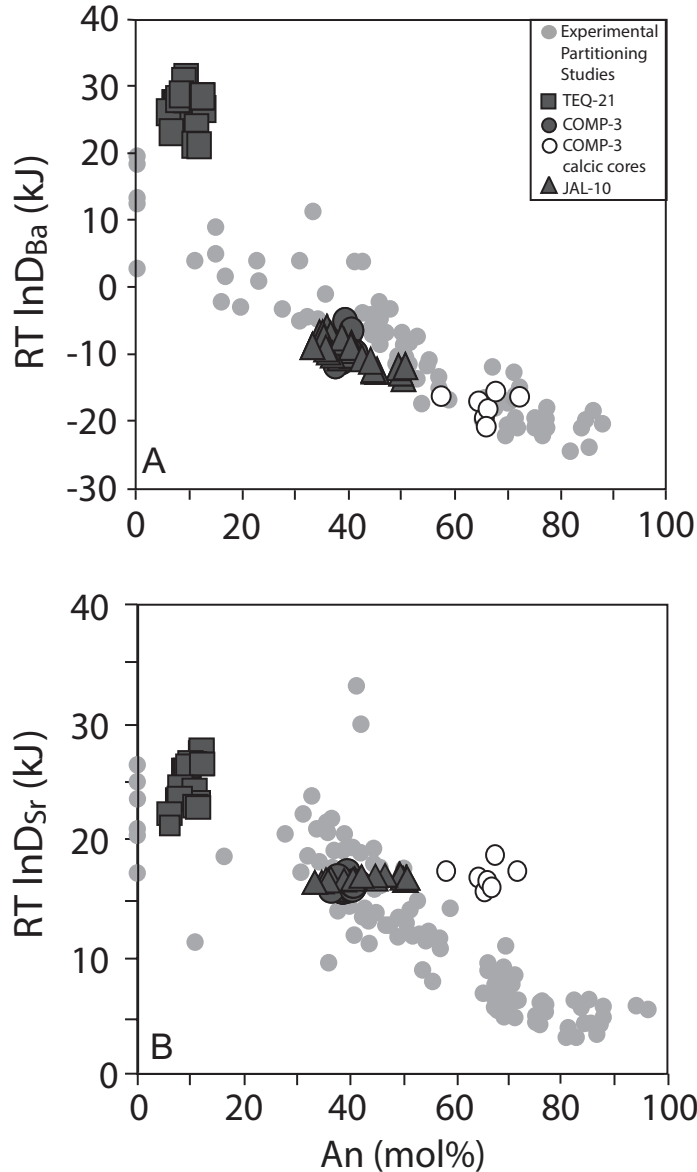


Figure 2.7: (A) Plot of $RT \ln D_{Ba}$ vs An (mol%) and (B) Plot of $RT \ln D_{Sr}$ vs An (mol%), where temperatures are those obtained from Fe-Ti oxides (Fig.2.7, Table 2.2) and D_{Ba} and D_{Sr} values are those calculated using the ppm Ba and Sr in plagioclase with the changing liquid Ba and Sr concentrations modeled by fractional crystallization (see text). Open symbols are samples from this study; grey circles the data used by Blundy and Wood (1991) to calibrate their model equation; grey squares and grey diamonds are the experimental data of Bindeman et al. (1998) and Bindeman and Davis (2000), respectively.

An additional feature of the data in Fig. 2.7b is that within each sample there is a trend of decreasing or unchanging $RT \ln(D_{Sr})$ with decreasing mol% An, whereas the trend predicted by the equation of Blundy and Wood (1991) is increasing values of

$RTln(D_{Sr})$ with decreasing mol% An. The results in Fig. 2.7b suggest that melt composition may also influence the partitioning of Sr between plagioclase and liquid.

Summary: Evidence for “Mafic” Xenocrysts at Trace Levels

On the basis of phase-equilibrium experiments and Sr partitioning data, xenocrysts of calcic plagioclase have been identified in five of six rhyolites. Based on the number of analyses plotted in Fig. 2.3, the proportion of phenocrysts (>50 microns) in each sample that is possibly xenocrystic ranges from 0-13%. Given the low overall abundances of phenocrysts in each sample, this leads to a maximum abundance of xenocrystic plagioclase in each sample of 0-0.17%. In addition, one of these rhyolites (MLV-37) appears to contain xenocrystic orthopyroxene (0.02% of sample) that is more Mg-rich than the phenocryst population. In all cases, the xenocrysts are more “mafic” than the phenocrysts and only occur in trace quantities (<0.2%). An outstanding question is whether these xenocrysts show diagnostic disequilibrium textures compared to phenocrysts, which can be evaluated with back-scattered electron (BSE) images.

2.7 BSE IMAGES OF XENOCRYSTS VS PHENOCRYSTS

BSE images of representative plagioclase and orthopyroxene crystals are presented for three samples (MLV-37 and MLV-45) in Figs. 2.8-9 to identify textures that may reflect their origin (phenocryst v. xenocryst).

Plagioclase

Examples of plagioclase xenocrysts are shown alongside examples of phenocrysts in Figs. 2.8-9, for samples MLV-37 and MLV-45, respectively. Plagioclase xenocrysts and phenocrysts from COMP-3 are provided in the Appendix (Fig. A6). In each sample,

the calcic xenocryst ($\sim\text{An}_{70}\text{-An}_{85}$) occurs as a core with a sharp interfacial boundary with the surrounding sodic plagioclase ($\sim\text{An}_{40}$) of variable thickness (Figs. 2.8a, 2.9a). In Fig. 2.8a (MLV-37), the calcic xenocryst is only partially enclosed by the more sodic phenocryst, and part of it remains in direct contact with the matrix liquid, without reaction. This lack of reaction is expected from the plagioclase phase diagram (Fig. 2.10), which shows that *calcic* xenocrysts will not melt, resorb or re-crystallize in a magma for which the equilibrium plagioclase is more sodic. The only reaction mechanism available to calcic xenocrysts is solid-state diffusion (NaSi-CaAl), which is slow. This is confirmed by experiments (e.g., Tsuchiyama 1985; Larsen 2005) where calcic plagioclase was placed into melts where the equilibrium plagioclase was more sodic; given sufficient time (53-480 hours), sodic plagioclase rims formed along the flat (unreacted) boundary with the calcic xenocrysts. In contrast, *sodic xenocrysts* (where the equilibrium plagioclase is more calcic) are expected to melt, resorb and recrystallize (Fig. 2.10), producing “dusty” rims, which is confirmed by experiments (e.g., Tsuchiyama 1985; Johannes et al. 1994; Nakamura and Shimakita 1998). Therefore, the textures of the calcic plagioclase crystals observed in this study are consistent with a xenocryst origin, but are not diagnostic. The only reason the calcic cores in the samples from this study are identified as xenocrysts is by comparison with the results of phase-equilibrium experiments and Sr partitioning (Fig. 2.5 and 2.7), and not because of their textural features.

In contrast, the plagioclase *phenocrysts* (inferred from phase-equilibrium experiments; Figs. 2.5 and 2.7) in these samples show a range of textures. In COMP-3, the phenocrysts ($\sim\text{An}_{40}$) are euhedral and faceted (Appendix Fig. A6), which is consistent

with equilibrium growth. However, in MLV-37 the phenocrysts ($\sim\text{An}_{45}$) are often anhedral, and crystal C displays a highly irregular shape (Fig. 2.8). Because crystal C is identical in composition to the rim of crystal A and crystal E in MLV-37, and it has the expected equilibrium plagioclase composition (Fig. 2.5), the possibility that its irregular shape is a growth texture rather than a resorption feature must be considered. The plagioclase phenocryst textures in MLV-45 (Fig. 2.9) support this hypothesis, with crystal C displaying incipient “swallow-tails”, a dendritic, diffusion-limited growth texture (e.g. Kirkpatrick et al. 1981).

Orthopyroxene

Evidence of diffusion-limited growth is particularly abundant among the orthopyroxene crystals, as seen in the BSE images for MLV-37 and MLV-45 (Figs. 2.8 and 2.9). Several of these orthopyroxene crystals display a vermiform-like texture, which Roeder et al. (2001) demonstrate is formed during diffusion-limited crystal growth (in chromites) from their cooling experiments on basalts (Appendix Fig. A7).

For example, at first glance, in MLV-37 (Fig. 2.8), crystals B, D and F appear to have resorption textures, given their irregular, rounded shapes and numerous melt inclusions. However, these crystals also display euhedral margins (at least on some sides). The Mg-rich core in crystal B (interpreted as a xenocryst on the basis of phase-equilibrium experiments; Fig. 2.6) is undergoing diffusive Fe-Mg exchange with the enclosing more Fe-rich orthopyroxene as seen from the microprobe analytical traverse for this crystal (Fig. 2.8). This is the expected reaction for an orthopyroxene xenocryst, namely to undergo Fe-Mg diffusive exchange rather than to resorb, if orthopyroxene is otherwise stable.

In sample MLV-45 (Fig. 2.9), crystals B and D (interpreted to be phenocrysts on the basis of phase-equilibrium experiments; Fig. 2.6) have highly irregular shapes, with abundant nubby protrusions along their margins. This texture is strikingly similar to the vermiform chromites produced in the cooling experiments of Roeder et al. (2001), where supercooling lead to cellular growth and the formation of multiple protuberances along the crystal margin (Appendix Fig. A7). As pointed out in that study, the metallurgical, material science and petrological literature contain several papers that discuss the change from planar to cellular to dendritic growth as the degree of undercooling increases (e.g., O'Hara et al. 1968; Lofgren 1974; Kirkpatrick 1975; Sekerka 1993; Hammer 2006). The faceted vermiform or cellular-growth texture seen along the margins of the orthopyroxenes in MLV-45 strongly suggest diffusion-limited rapid growth conditions and not resorption. Moreover, the abundant mineral inclusions (ilmenite, titanomagnetite, zircon and apatite) in these orthopyroxene crystals are consistent with their growth from an evolved SiO₂-rich liquid, as *all* of these mineral phases are stable in rhyolite melts.

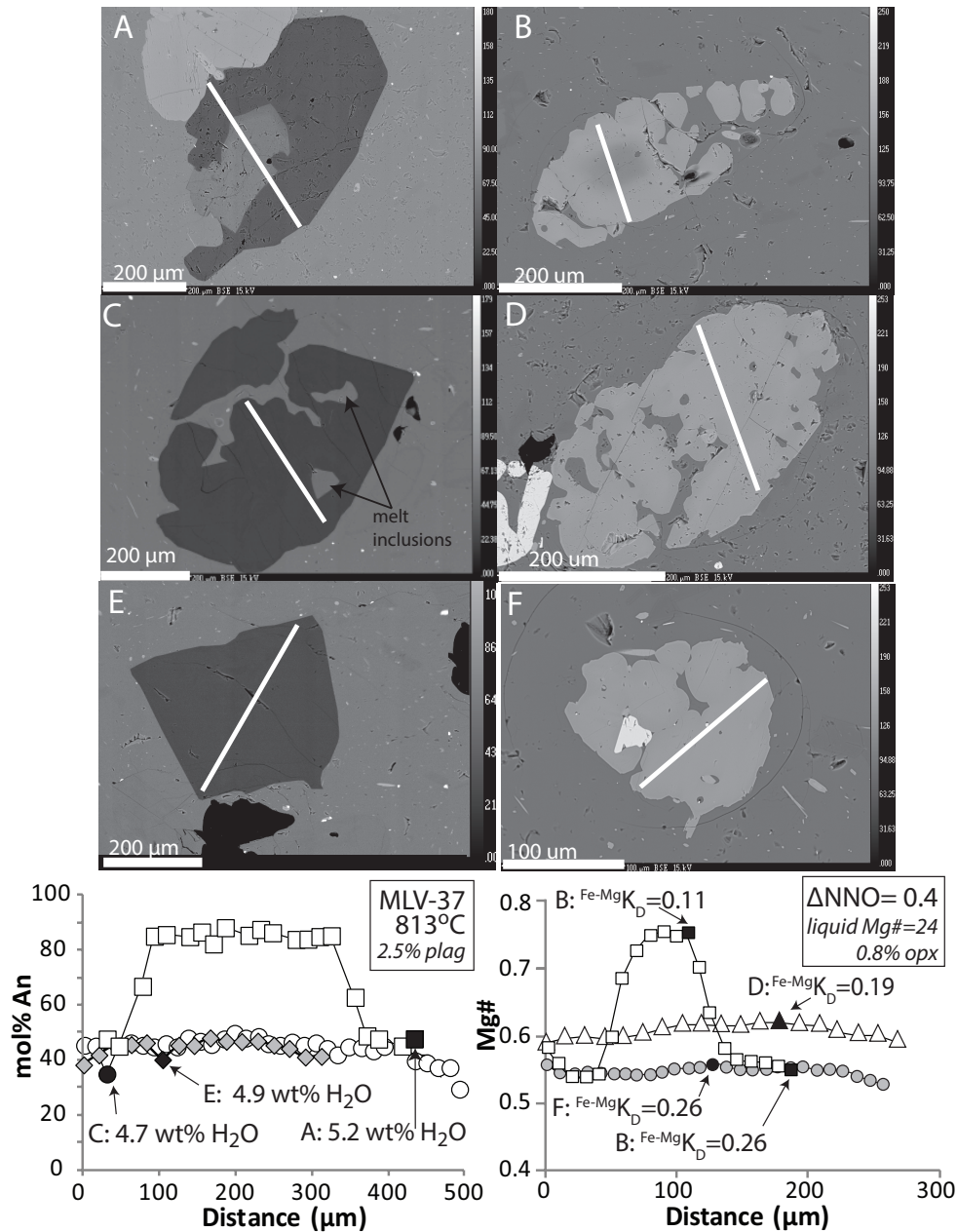


Figure 2.8: BSE images of plagioclase and orthopyroxene crystals (A-F) in MLV-37. A possible xenocrystic core (A) (An₈₀) is featured alongside two grains of plausible phenocrysts (An₃₄₋₅₀) (C and E), which display rounded margins that may reflect growth textures (see text). BSE images of orthopyroxene crystals are shown in B, D and F. A possible Mg-rich (>70 Mg#) xenocryst core is shown in (B). All other crystals have Mg#s that range from 53-62, and corresponding $^{Fe-Mg}K_D$ values that range from 0.28-0.19, respectively (B, D, and F). The orthopyroxene textures are complex with textures that are rounded, nubby, and with multiple melt inclusions (B, D, F), along side euhedral margins.

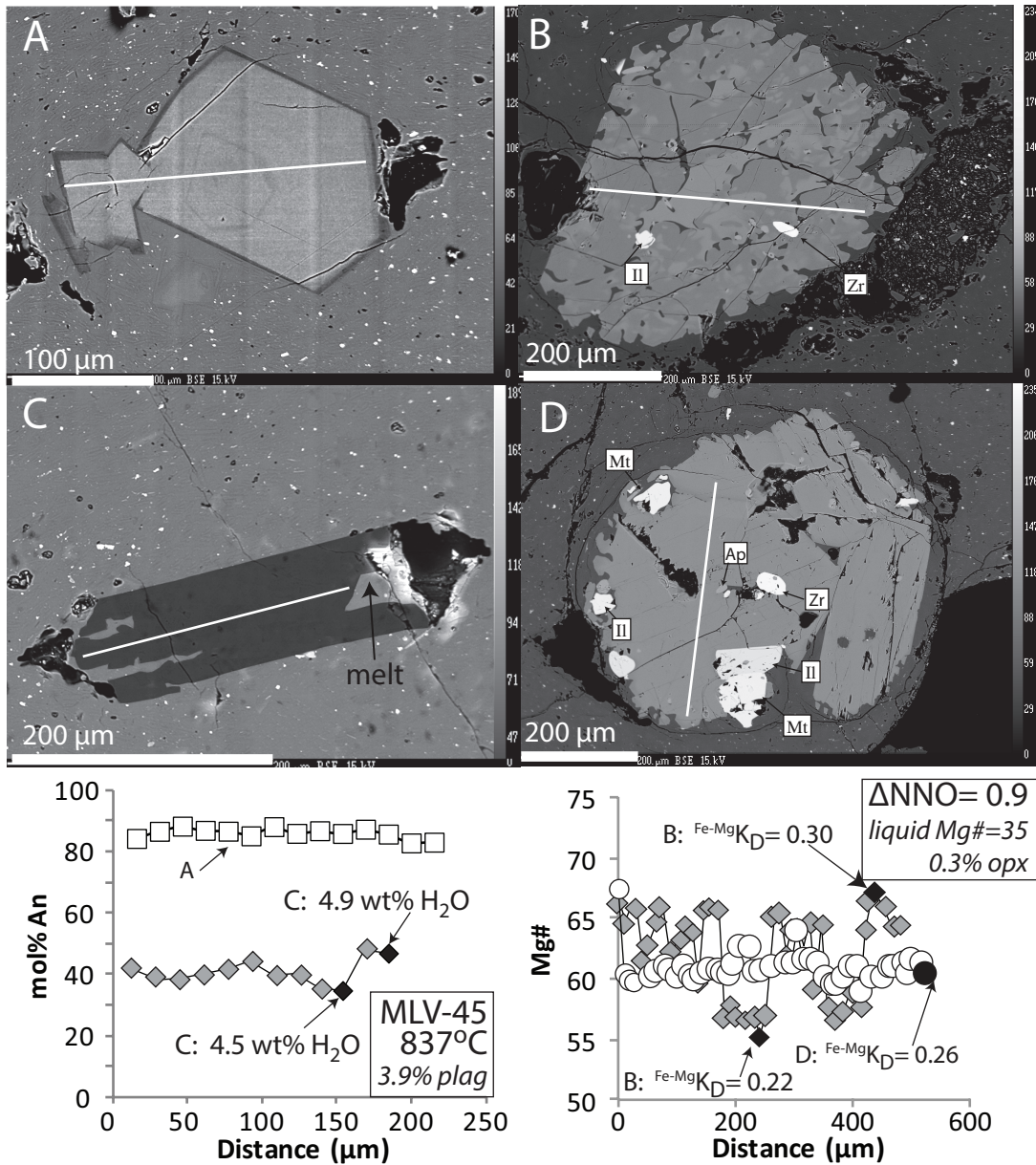


Figure 2.9 BSE images of plagioclase crystals (A and C) in MLV-55. A possible xenocrystic core (A) (An₈₅) is featured alongside a plausible phenocryst (An₃₅₋₅₅) (C). Crystal C displays swallow-tail texture, indicative of diffusion-limited growth. BSE images possible orthopyroxene phenocrysts are shown with Mg#s ranging from 55-70, and corresponding ^{Fe-Mg}K_D values that range from 0.45-0.22, respectively (B and D). Orthopyroxene crystals (B and D) are variably zoned and unzoned and all exhibit vermiform growth texture, which is characteristic of rapid, diffusion-limited growth (see text).

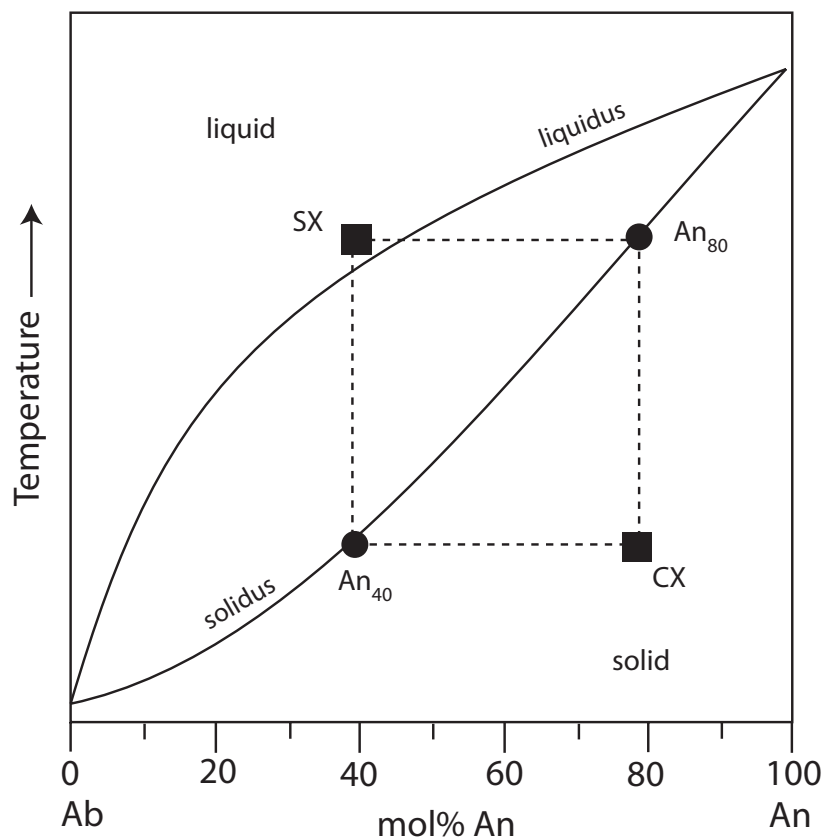


Figure 2.10: Schematic plot of the plagioclase binary loop projected from a magmatic liquid. An_{80} and An_{40} are equilibrium plagioclase on the solidus. CX is a calcic xenocryst, which is always in the crystalline stability field and re-equilibration occurs by solid-state diffusion. SX is a sodic xenocryst, which is always in the liquid stability field and re-equilibration occurs by melting and recrystallization of a more calcic plagioclase. For this phase diagram, the effect of an abrupt decrease in f_{H_2O} , or degassing, is equivalent to an abrupt decrease in temperature.

2.8 DEGASSING-INDUCED CRYSTALLIZATION OF PHENOCRYSTS?

The diffusion-limited growth textures seen in several of the plagioclase and orthopyroxene phenocrysts in the samples from this study (Figs. 2.8-9), combined with the small variation in temperature obtained for each sample from the Fe-Ti oxides (Table 2.2), raises the question of whether phenocryst growth was driven by degassing rather than cooling. Rapid ascent of the host magma along fractures under fluid-saturated conditions could lead to the development of large undercoolings and thus diffusion-

limited growth of phenocrysts. Degassing-induced crystallization may also explain the relatively wide compositional range of plagioclase and orthopyroxene phenocrysts in these samples, given that variations in melt water concentration are known to affect the composition of plagioclase (e.g., Sisson and Grove 1993) and possibly orthopyroxene (Crabtree and Lange 2011; Frey et al. 2011). Otherwise, the wide ranges in the plagioclase and orthopyroxene *phenocryst* compositions (excluding xenocrysts) are puzzling in these rhyolitic liquids given the low overall abundance of phenocrysts (2-6%) in these six samples. To test the hypothesis of degassing-induced crystallization of phenocrysts, the first step is to determine pre-eruptive water concentrations at the time of phenocryst growth.

Calculation of melt water concentrations

Water contents are readily calculated in the phenocryst-poor obsidian samples in this study using the plagioclase-liquid hygrometer of Lange et al. (2009), which has been recently recalibrated for rhyolites (Lange et al. 2012; Waters et al. 2012). Application of the plagioclase-liquid hygrometer requires an independent assessment of temperature, which is obtained from the two Fe-Ti oxides (Table 2.2). The plagioclase-liquid hygrometer of Lange et al. (2009) is calibrated on an experimental data set that spans a wide range of liquid silica concentration (46-74 wt% SiO₂), plagioclase compositions (An₃₇₋₉₃), temperature (825-1230°C), and pressure (0-300 MPa), but does not cover the entire range of conditions appropriate to rhyolites. Waters et al. (2012) conducted a series of water-saturated phase equilibrium experiments from 300-100 MPa and 750-900°C on three rhyolite and rhyodacite samples. Their experimental results, along with those from the literature on similar melts (e.g., Larsen, 2006; Coombs and Gardner, 2002;

Tomiya et al., 2010), have been used to re-calibrate the plagioclase-liquid hygrometer (Lange et al., 2012). The new calibration (Appendix Table A8) extends the range of plagioclase down to An₁₉ and the melt composition up to 78 wt% SiO₂. The effect of pressure on the hygrometer is small (± 100 MPa = ± 0.1 wt% H₂O) and therefore a constant pressure of 100 MPa can be used in all calculations.

The results of the melt water calculations are shown in the plagioclase histograms in Fig. 2.3. Due to the glassy, crystal-poor nature of each sample (Table 2.1), the bulk rock composition was used as the liquid composition in all hygrometer calculations. By using the bulk composition, the change in liquid composition due to crystallization of sparse phenocrysts was not taken into account, leading to a small *underestimate* (≤ 0.1 wt%) of the melt water concentrations, which ranges from 2.4-5.9 wt%, at the time of peak crystallization of plagioclase.

Although the dissolved water concentrations (2.4-5.9 wt%) calculated with the plagioclase-liquid hygrometer for the rhyolites from this study overlap those (3-8 wt%) reported from quartz-hosted melt inclusions in rhyolites (e.g., Dunbar et al. 1989; Westrich et al. 1991; Lowenstern 1993, 1994; Wallace et al. 1999; Liu et al. 2006; Allen et al. 2010; Smith et al. 2010; Johnson et al. 2011), no quartz was found in any of the rhyolite samples from this study. This may be explained by the phenocryst-poor character of the obsidian samples in this study, combined with the observation that the plagioclase-in curve is located at higher temperatures/pressures than that for the quartz-in curve in experiments on natural rhyolites at ≤ 200 MPa (Coombs and Gardner 2001; Couch et al., 2003a; Tomiya et al. 2010). This reflects the fact that the stability of quartz decreases with decreasing pressure during ascent in rhyolite melts (including

eutectic/minimum melts that segregate from a quartz-bearing assemblage) (Tuttle and Bowen, 1958), such that the plagioclase-in curve will be located at a higher pressure than that for quartz at shallow depths.

Comparison to experimental phase diagram for rhyolite

In Fig. 2.11, the plagioclase and quartz-in curves from the experiments of Tomiya et al. (2010) are shown in a H₂O fluid-saturated phase diagram, along with isopleths of dissolved wt% H₂O calculated from the water solubility model of Liu et al. (2005) for rhyolite melts. The calculated melt water concentrations for MLV-45 during plagioclase crystallization are plotted in this diagram, along with the temperature obtained for this sample (837 ± 20 °C) from the Fe-Ti oxides. The most calcic plagioclase phenocryst (An₇₀) leads to a calculated melt water concentration of 5.8 wt% H₂O, which crosses the plagioclase-in curve in Fig. 2.11 at 837°C. Collectively, the plagioclase phenocrysts in MLV-45 lead to calculated water concentrations that are plotted on the adiabatic ascent path in Figure 2.11, consistent with degassing-induced crystallization of a fluid-saturated magma as it ascended rapidly along a fracture. Although the phase diagram in Fig. 2.11 is for pure H₂O fluid-saturated conditions, the only effect of adding CO₂ to the system is to increase the absolute value of total pressure on the y-axis in Fig. 2.11, which will steepen the slope of the plagioclase-in curve. Importantly, the negative slope of the plagioclase-in curve is preserved as long as the magma is saturated in H₂O-CO₂ fluid

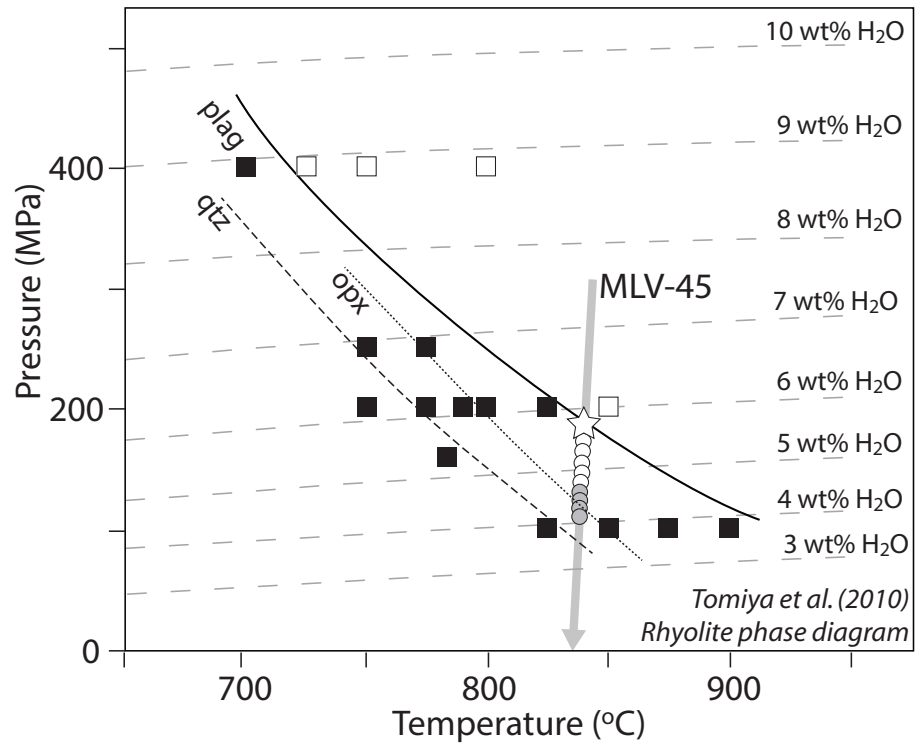


Figure 2.11: Phase diagram for H₂O fluid-saturated, low-K rhyolite from the experiments of Tomiya et al. (2010). Dashed lines show isopleths of water solubility in the melt when saturated with pure H₂O fluid from the model of Liu et al. (2005). Superimposed is an ascent path for rhyolite MLV-45 at the temperature obtained by two Fe-Ti oxide thermometry. The ascent path is modeled as adiabatic (rapid transport along a fracture), $(dT/dP)_S = TV\alpha/C_p$, where T is temperature in Kelvin, V is molar volume, α is the coefficient of thermal expansion (calculated from Lange, 1997 and Ochs and Lange, 1999) and C_p is the molar heat capacity (calculated from Lange and Navrotsky, 1993, with partial molar C_p of the H₂O component from Spera, 2000). For dissolved water concentrations of 2-6 wt%, the adiabat varies from 3-5 degrees per 100 MPa, respectively, and closely approximates an isothermal path. Open and grey circles correspond to water concentrations calculated with the plagioclase-liquid hygrometer applied to phenocrysts and microlites, respectively (Fig. 2.5).

The question arises as to why plagioclase crystals in MLV-45 do not record water concentrations < 4.0 wt%, consistent with continued degassing of the magma as it ascended to the surface. It appears that crystallization ceased in this rhyolite at a melt water concentration of ~4.0 wt% H₂O, before the magma crossed the quartz-in curve (Fig. 2.11), possibly because of a kinetic barrier to nucleation (discussed more fully below). The results of the hygrometer also indicate that the transition from growth-dominated to nucleation-dominated crystallization (i.e., phenocrysts to microlites; Hammer et al. 1999; Couch et al. 2003a; Blundy and Cashman 2008) occurred at a

relatively high melt water concentration (~ 4.5 wt% H_2O ; Fig. 2.3) in MLV-45, and therefore at relatively deep conditions (≥ 130 MPa; ≥ 4 km). The relationship between degree of undercooling and the transition from growth-dominated to nucleation-dominated crystallization, in the context of a rapidly ascending magma undergoing degassing-induced crystallization, is discussed more fully below.

Crystal growth rates vs. nucleation rates with undercooling

The evidence outlined in Fig. 2.11 supports the hypothesis that the wide range in plagioclase phenocryst compositions in MLV-45 can be explained by adiabatic ascent under fluid-saturated conditions. A degassing scenario is also consistent with the pattern observed in its plagioclase histogram in Fig. 2.3, namely a phenocryst population that peaks in the mid-compositional range and a microlite population that overlaps the sodic end of the phenocryst population. The connection between degassing-induced crystallization and the histograms in Fig. 2.3 is illustrated with a schematic plot (Fig. 2.12; modified from the experimental results of Meiling and Uhlmann, 1967) of how crystal growth rate and nucleation rate vary as a function of undercooling ($\Delta T = T$ of plagioclase liquidus – T of magma). Similar diagrams have been constructed from the results of decompression experiments under fluid-saturated conditions (e.g., Hammer and Rutherford, 2002; Couch et al., 2003b).

For example, when a fluid-saturated rhyolite liquid, such as MLV-45, ascends adiabatically and crosses the plagioclase-in curve (Fig. 2.12a), the magnitude of the undercooling ($\Delta T = T$ of plagioclase liquidus – T of magma) will increase as the melt water concentration decreases. The most calcic plagioclase phenocryst is expected to

form at low ΔT (zone 1 in Fig. 2.12b), which corresponds to relatively low crystal growth rates and low nucleation rates. Therefore, for a rapidly ascending magma that does not

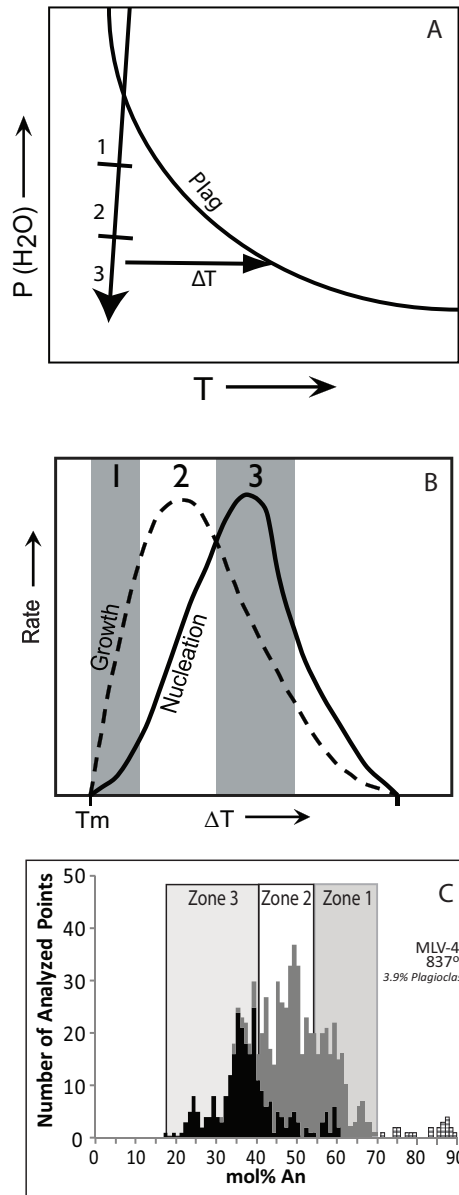


Figure 2.12: Schematic fluid-saturated plagioclase liquidus curve on a pressure v. temperature plot. After an ascending magma crosses the plagioclase-in curve, it passes through three zones, where ΔT (=temperature of plagioclase liquidus- temperature of magma) progressively increases. (B) Schematic plot of crystal growth rate and nucleation rate with degree of under cooling (ΔT); modified from the experiments of Meiling and Uhlmann (1967). Three zones are indicated, which correspond to those in (A). In zone 1, the most calcic plagioclase grows, owing to relatively high melt water concentrations; nucleation rates are low, and crystal growth rates are increasing. In zone 2, plagioclase of intermediate composition grows as nucleation rates increase and crystal growth rates peak; this composition is expected to be the most abundant. In zone 3, the most sodic plagioclase grows, owing to relatively low melt water, and marks the transition from growth-controlled crystallization (i.e. phenocrysts) to nucleation-controlled crystallization (i.e. microlites).

stall, the most calcic plagioclase phenocrysts are expected to form in relatively low abundance, which is consistent with the plagioclase histogram for MLV-45 in Fig. 2.3. As the magma continues to ascend and degas, *both* the crystal growth rate and nucleation rates increase (zone 2 in Fig. 2.12b) and the plagioclase becomes more sodic. Plagioclase growth during zone 2 corresponds to the mid-range An peak in the histogram. Further ascent and degassing will increase undercooling to the point where the crystal growth rate declines and the nucleation rate reaches a maximum (zone 3 in the Fig. 2.12b). In this interval, microlite crystallization occurs, in conjunction with dwindling phenocryst growth. At this stage, both the microlites and the phenocrysts are more sodic due to declining melt water concentrations during ascent, as well as changing melt composition (lower CaO/Na₂O ratios) due to sparse plagioclase crystallization. Therefore, the histogram pattern in Fig. 2.3 for MLV-45, as well as those for the other five rhyolites, is fully consistent with degassing-induced crystallization, which in turn has been documented in decompression experiments (e.g. Couch et al., 2003b).

The schematic diagram in Fig. 2.12 additionally explains all the zoning patterns found in the plagioclase crystals in the obsidian samples from this study (Appendix Fig. A4), which includes normal, reverse and no zoning at all. During stage 2, the rates of *both* crystal growth and nucleation increase, although crystal growth is dominant. This leads to different possible zoning patterns, including the classic case of normal zoning where sodic rims grow on calcic cores that previously grew during stage 1. However, because of rapid, diffusion-limited crystal growth, it is additionally possible for initial crystallization of calcic plagioclase during stage 1 to be skeletal and/or hopper, with large liquid interior regions in communication with the matrix liquid. Subsequent growth of

more sodic plagioclase during stage 2 can occur in these large melt hollows, leading to reverse zoning. Finally, because the nucleation rate is increasing during stage 2, it is additionally possible for nucleation of relatively sodic plagioclase to occur from the liquid, without it always having to grow on pre-existing calcic plagioclase, forming relatively sodic plagioclase crystals with little to weak zoning. Although nucleation of plagioclase from the liquid becomes dominant in stage 3, it is expected to occur during stage 2, albeit at a lower rate.

Couch et al. (2003b) explore how undercooling driven by degassing affects plagioclase growth rates and nucleation rates in a rhyolite melt during isothermal decompression experiments under pure H₂O-fluid saturated conditions. For example, one of their runs (#236) was a multistep (MD) decompression experiment at 875°C, where the sample was initially held at 160 MPa for a period of 16 hours, and then the pressure was dropped to 50 MPa in eight steps, with a dwell time of one hour per step (Fig. 2.13). The calculated water solubility (Liu et al., 2005), melt viscosity (Hui and Zhang, 2007) and equilibrium plagioclase composition (Couch et al., 2003a,b) at each pressure step in this MD experiment is shown in Figure 2.13a. Despite an undercooling of 132 degrees at 50 MPa, the abundance of plagioclase in the final run product is only 15.7 wt% (6.4 vol%), whereas the equilibrium abundance is ~28.1 wt% (Couch et al., 2003a). The reported plagioclase composition ($\pm 1\sigma$) in the run product is 50.1 ± 3.0 mol% An. Although the full range of observed plagioclase composition is not reported, it must be larger than the 1σ standard deviation (± 3 mol% An) and may have extended to An₅₅-An₄₅. From Figure 13b, it is clear that most of the plagioclase crystallization in the MD decompression experiment occurred during steps 4 through 7, at the peak of the

crystallization growth curve, as determined in their various experiments on this rhyolite.

This is exactly the pattern predicted in Fig. 2.12 and observed in the histograms in Fig.

2.3.

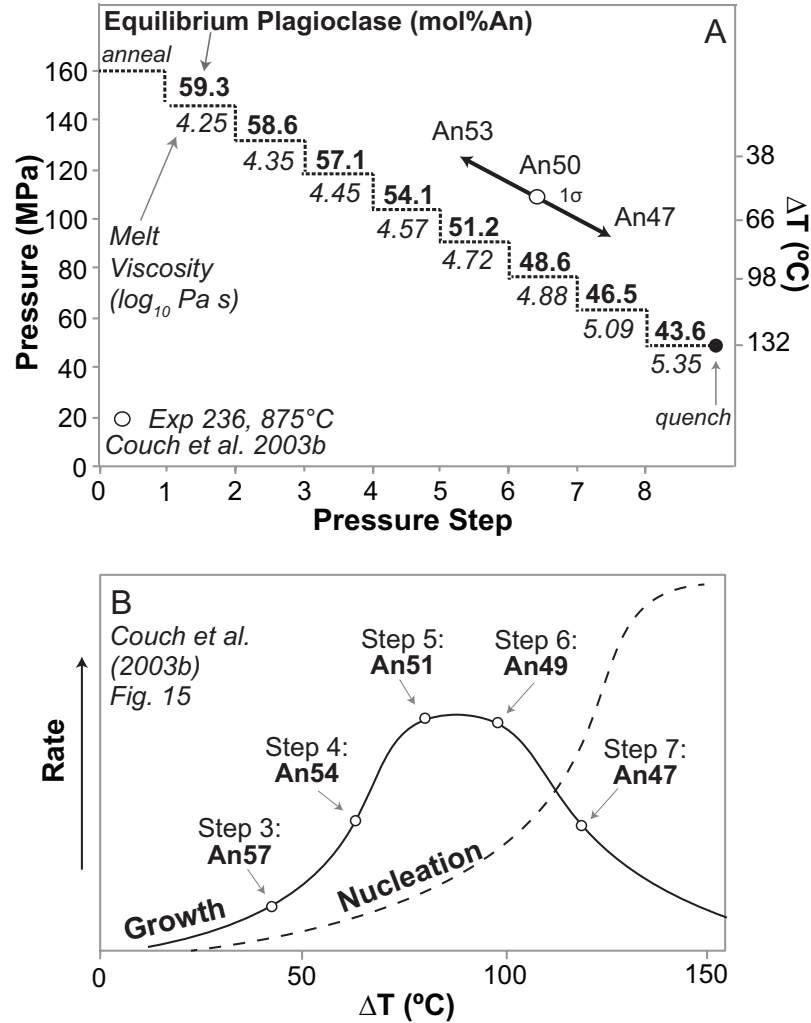


Figure 2.13: (A) A multistep (MD) decompression path for experiment 236 of Couch et al. (2003b) is shown as a dashed line at a constant temperature of 875°C. Melt viscosities (\log_{10} Pa s) are shown beneath the decompression path in italicized font and are calculated with the water solubility model of Liu et al. (2005) and the viscosity model of Zhang and Hui (2007) and the equilibrium plagioclase composition reported by Couch et al. (2003a, b). The mean plagioclase composition grown in experiment 236 is shown above the decompression path with a hollow circle, along with a 1 σ (solid black line) and ~2 σ (dashed line) standard deviation. Experiment 236 ceased nucleation and growth at ~An44-An47, which corresponds to melt viscosities of 4.88-5.35 \log_{10} Pa s. (B) A schematic plot of nucleation and growth curves as a function of undercooling (ΔT) is drawn based on rates observed in the experiments of Couch et al. (2003b) (and shown as Figure 2.15 in Couch et al., 2003b). Decompression steps 3-7 are shown on the growth curve at their approximate undercooling (ΔT) with corresponding plagioclase compositions (from A). The average plagioclase composition measured by Couch et al. (2003) in experiment 236 and the 1 σ distribution corresponds to the maximum growth rates in B.

Rapid degassing during ascent as a kinetic barrier to nucleation

What is perhaps most surprising from the data presented thus far is the relatively high concentrations of water in each of the six rhyolite samples at the time nucleation ceased (Fig. 2.3), thus facilitating the eruption of crystal-poor rhyolite glasses (obsidians). In one sample, MLV-36, no microlites formed (Figs. 2.1 and 2.3), clearly indicating that nucleation ceased at melt water concentrations of ~ 3.8 wt% H_2O (Fig. 2.3) and therefore pressures ≥ 100 MPa (depths ≥ 3.8 km). It is well understood that the rate of undercooling is an important control on whether or not a liquid will quench to a glass and that melt viscosity also plays a role; the higher the rate of undercooling, the lower the melt viscosity when nucleation ceases. High melt viscosity contributes to a kinetic lag in nucleation owing to low melt component diffusivity (e.g., Loomis 1981), and it is therefore of interest to calculate the melt viscosity for each obsidian sample when plagioclase crystallization ceased.

Because both temperature and melt water concentration are known for each sample (obtained from the Fe-Ti oxides and plagioclase-liquid hygrometer, respectively; Fig. 2.3), the viscosity of the melt phase during plagioclase crystallization can be calculated using the model of Hui and Zhang (2007). In Fig. 2.14, the melt viscosity corresponding to growth of the most calcic plagioclase phenocrysts (i.e., at the highest calculated melt water concentration) is marked by a black square, whereas the melt viscosity corresponding to the onset of microlite crystallization is marked by a black diamond. Also shown is the maximum melt viscosity at the end of plagioclase crystallization. The sample that ceased crystallization at the lowest melt viscosity (~ 4.7 \log_{10} Pa-s) is MLV-36; therefore, it experienced the highest rate of undercooling. The

mechanism to induce this rapid rate of undercooling must have been degassing (through ascent and decompression) and not actual cooling, because at depths ≥ 3.8 km, such rapid rates of undercooling (to prevent microlite growth) cannot be achieved by conductive cooling in the upper crust.

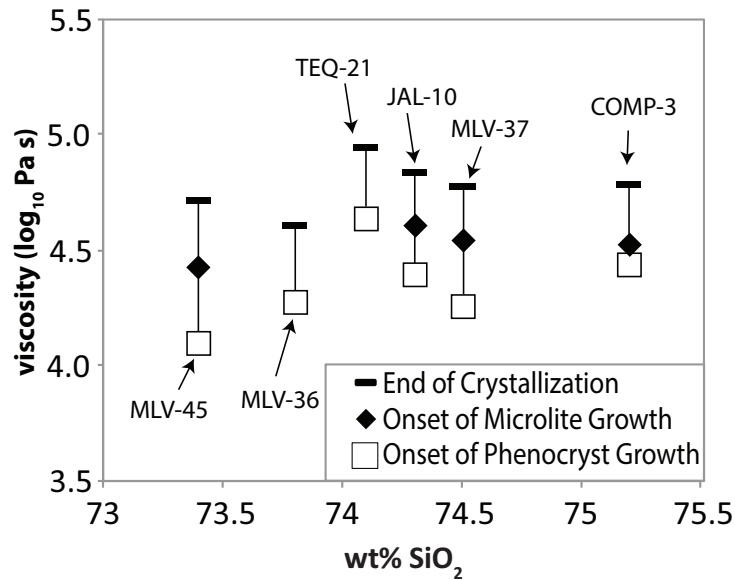


Figure 2.14: A plot of melt viscosity during plagioclase growth for each sample as a function of wt% SiO₂. Melt viscosity is calculated from the model of Hui and Zhang (2007), using the bulk liquid compositions (Table 2.1), temperatures from the Fe-Ti oxides (Table 2.2), and the melt water concentrations from the plagioclase-liquid hygrometer (Fig. 2.5). Black squares mark the onset of phenocryst crystallization; open diamonds mark the onset of extensive microlite crystallization; black bars mark the cessation of crystallization.

A broad constraint on the ascent rate for MLV-36 can be drawn from the experimental results for run #236 from Couch et al. (2003b), shown in Figure 2.13. In that experiment, decompression from 160 to 50 MPa occurred in eight hours and the authors report that the plagioclase composition expected for the final pressure (50 MPa) did not grow in that experiment. From Figure 2.13b, it is seen that a cessation of plagioclase nucleation and growth occurred once the melt viscosity reached $\sim 5.2 \log_{10}$ Pa s (between steps 7 and 8). This result suggests that MLV-36, which contains no microlites and ceased nucleation at a melt viscosity of $\sim 4.7 \log_{10}$ Pa-s, had a faster

decompression path, and probably transited from ≥ 4.7 km (depth of its plagioclase liquidus) to the surface in less than eight hours.

Degassing to explain the variable orthopyroxene compositions?

Given that the wide range in plagioclase composition in each sample (Fig. 2.3) is plausibly explained by degassing-induced crystallization during magma ascent (Fig. 2.11), the question arises as to whether this process can also explain the wide compositional range in the orthopyroxenes (Fig. 2.4). Their variation in Mg# (Fig. 2.4) cannot be explained by oxidation caused by degassing (e.g., Luhr, 2000; Burgisser and Scaillet, 2007) because the post-eruptive Fe^{2+} concentrations (wt% FeO), as measured by titration (Table 2.1), are within analytical error of the pre-eruptive Fe^{2+} concentration during phenocryst growth prior to extensive degassing, as obtained from the two Fe-Ti oxides (Table 2.1). In other words, there is no analytical evidence that degassing had any measurable effect on the ferric-ferrous ratio in these rhyolites, which is consistent with the results of Crabtree and Lange (2012) for phenocryst-poor andesites and dacites.

There is evidence, however, that an increase in melt water concentration (i.e., dissolved hydroxyl groups) favors a more Fe-rich orthopyroxene. For example, this result is found in the phase-equilibrium experiments of Grove et al. (2003) on a Mt. Shasta Mg-andesite (Fig. 2.15a) and from experiments of Gardner et al. (1995) on Mount St. Helens dacite (Fig. 2.15b); in both studies, values of $^{Fe-Mg}K_D$ increase with melt water concentration. A positive correlation between $^{Fe-Mg}K_D$ and dissolved water in the melt phase is additionally found in the combined phase-equilibrium experiments of Coombs and Gardner (2001) and Tomiya et al. (2010) on rhyolites. Those data show that $^{Fe-Mg}K_D$ between orthopyroxene and liquid increases from $\sim 0.2-0.3$ at ~ 4 wt% H_2O to $\sim 0.4-0.5$ at

~6 wt% H₂O (Fig. 2.15c). Although there are undoubtedly other compositional components in the melt phase, in addition to H₂O, that affect the ^{Fe-Mg}K_D value between orthopyroxene and liquid, the available evidence strongly suggests that a loss of water during degassing can induce the observed change in the Mg# of orthopyroxenes.

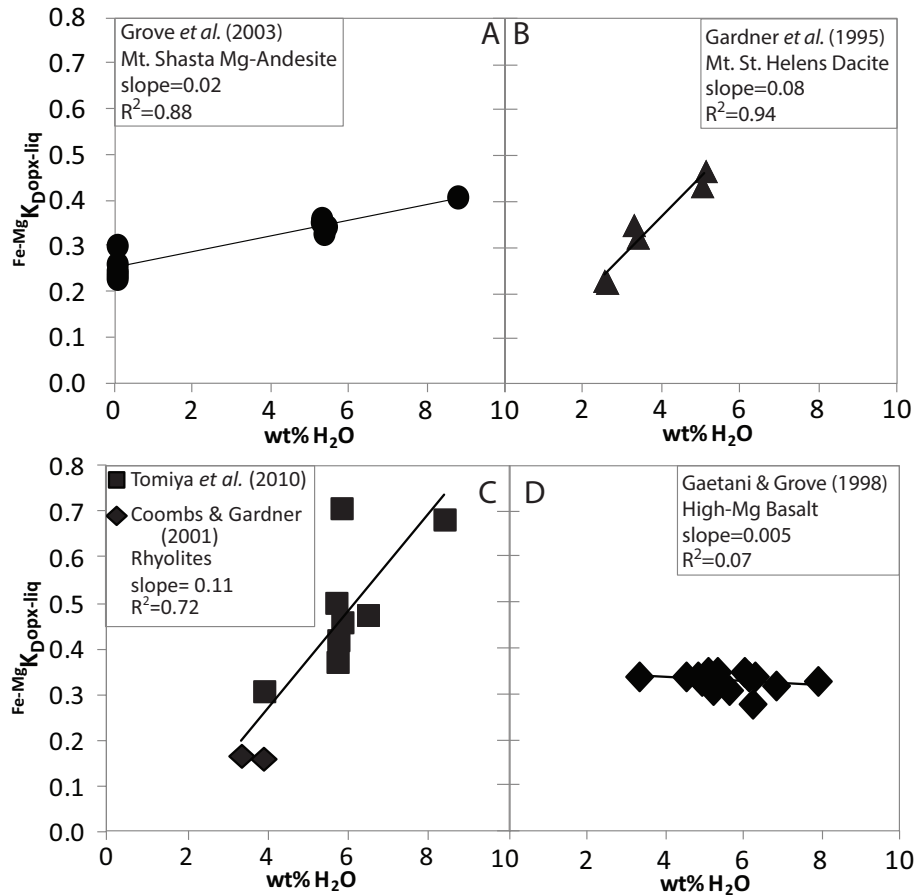


Figure 2.15: A plot of wt% H₂O and ^{Fe-Mg}K_D values between orthopyroxene and liquid for water-saturated phase equilibrium experiments on Mg-rich andesite (a) (Grove *et al.* 2003), (b) dacite (Gardner *et al.* 1995), (c) rhyolite (Tomiya *et al.* 2010 and Coombs and Gardner 2001) and (d) high-Mg basalt (Gaetani and Grove 1998). The effect of dissolved water on the ^{Fe-Mg}K_D values is greater in more evolved liquids (i.e., lower MgO).

As discussed previously by Crabtree and Lange (2011) and Frey and Lange (2011), the mechanism by which dissolved water might reduce the activity of MgO

relative to FeO in the melt phase, and therefore the Mg# of orthopyroxene, is through the following reaction:



At 298 K and one bar, the free energy of the reaction for the solids in Eq. 3, using the JANAF thermochemical tables (4th edition; Chase 1998) is -24.2 kJ/mole, which indicates that hydroxyl groups preferentially complex with Mg²⁺ rather than Fe²⁺ and suggests that dissolved hydroxyl groups may reduce the activity of MgO relative to FeO in the melt phase. A similar reaction can be written involving the CaO and Na₂O components:



At 298 K and one bar, the free energy of the reaction for the solids in Eq. 2.4 is -85.5 kJ/mole (Chase 1998), which shows that hydroxyl groups strongly favor complexing with Na⁺ compared to Ca²⁺. Lange et al. (2009) present evidence that the reaction in Eq. 2.4 provides the basis of the plagioclase-liquid hygrometer. If correct, Eq. 3 predicts that an increase in dissolved water in magmatic liquids will favor a more Fe-rich pyroxene in the same way that it favors a more Ca-rich plagioclase.

Another question that arises from the experimental data in Fig. 2.15 is why is there a progression in the magnitude of how dissolved water affects the composition (Mg#) of orthopyroxenes as a function of melt composition (rhyolite > dacite > andesite > basalt). In fact, the evidence from the experiments of Gaetani and Grove (1998) is that dissolved water has *no* effect on the ^{Fe-Mg}K_D between orthopyroxene and *basalt* liquid (Fig. 2.15d). The main reason may be that the effect of dissolved water in reducing the activity of MgO relative to FeO is more discernible when MgO concentrations are relatively low. In other words, for a given amount of dissolved hydroxyl groups, there

will be a greater *relative* effect on the activity of MgO in rhyolite liquids with < 0.4 wt % MgO (Tomiya et al. 2010) compared to basalt liquids with 11-13 wt% MgO (Gaetani and Grove 1998). For a fixed concentration of dissolved H₂O, melts with relatively low MgO concentrations are expected to have a greater *proportion* of their Mg²⁺ cations speciated to hydroxyl groups compared to melts with much higher MgO concentrations.

In summary, the experimental evidence summarized in Fig. 2.15 is fully consistent with the hypothesis that degassing-induced crystallization not only led to the diffusion-limited growth textures of the orthopyroxenes in the samples from this study (Fig. 2.8 and 2.9), but also explains the wide compositional variation observed for the orthopyroxene population in each sample ($\leq 14\%$ Mg#), despite their low abundance (< 1%).

2.9 CONCLUSIONS

One of the most important observations from this study is that rhyolites with only 2-6 % phenocrysts (+ microphenocrysts) are multiply saturated with five to eight different mineral phases (plagioclase + orthopyroxene + titanomagnetite + ilmenite + apatite \pm zircon \pm hornblende \pm clinopyroxene \pm sanidine). This permits temperatures to be obtained from Fe-Ti oxide thermometry (~ 780 to 940°C), which in turn allows pre-eruptive water concentrations to be calculated with the plagioclase-liquid hygrometer (~ 1.5 - 5.7 wt% during peak crystallization of plagioclase). The results indicate that these magmas were fluid-saturated in the upper crust, and therefore degassing-induced crystallization was inevitable during magma ascent. That the rhyolites were each multiply saturated with five to eight mineral phases at such low crystallinities (2-6%)

suggests that they segregated as an interstitial liquid from a source (crystal-rich magma or partially-melted pluton) that contained all of these mineral phases.

Comparison with phase-equilibrium experiments from the literature permit phenocrysts vs. xenocrysts to be identified in the obsidian samples; in all cases the xenocrysts only occur in trace ($< 0.2\%$) quantities and are “mafic” (calcic plagioclase and a rare case of Mg-rich orthopyroxene). The evidence from this study indicates that the wide compositional range of plagioclase phenocrysts (typically An_{50} - An_{30} in the five less-evolved rhyolites) formed because of a progressive loss of water (< 1.5 wt%) during magma ascent. It also appears that the wide compositional range in the orthopyroxene populations (≤ 14 mol% Mg#) formed by the same process, with higher melt water concentrations leading to more Fe-rich pyroxenes.

Finally, there is clear evidence that these phenocryst-poor, fluid-saturated rhyolite magmas were transported rapidly to the surface, in most cases from depths ≥ 2 -7 km. The loss of water during magma ascent, owing to degassing, caused a large undercooling and an increase in melt viscosity, which together contributed to diffusion-limited crystal growth (e.g., vermiform texture in orthopyroxenes) and led a kinetic barrier to nucleation. For example, sample MLV-36 ascended so rapidly that no microlites formed and crystallization ceased at a melt viscosity as low as $4.7 \log_{10}$ Pa-s.

Acknowledgements

This paper is dedicated to the memory of Ian Carmichael, who had an abiding interest in obsidians that began when he was an undergraduate and first introduced to the “pitchstones” in Scotland. As far back as the 1960s, Ian recognized the opportunity that glassy rhyolites provided to extract information on pre-eruptive temperatures, oxidation

states, and melt water concentrations, which eventually led to his life-long pursuit of the application of thermodynamics to magmatic systems. We were privileged to talk over the early stages of this study with Ian, who – as always –gave valued advice and encouragement. Ian’s thermodynamic “intuition” led him to long argue (at least to his graduate students) that dissolved water should favor $\text{Mg}(\text{OH})_2$ over $\text{Fe}(\text{OH})_2$ species in the melt, and he expected this to affect ferromagnesian phases in hydrous magmas. These conversations planted the seed for us to think about progressive loss of dissolved water as an explanation for the wide range in orthopyroxene compositions in the rhyolites from this study. This work was funded by the National Science Foundation: EAR-12503685 and EAR- 9911352 (equipment grant for electron microprobe at the University of Michigan), along with discretionary funds from the University of Michigan.

2.10 REFERENCES

- Allen SR, Fiske RS, Yoshihiko T (2010) Effects of water depth on pumice formation in submarine domes at Sumisu, Izu-Bonin arc, western Pacific. *Geology* 38:391-394
- Anderson, AT (1984) Probably relations between plagioclase zoning and magma dynamics, Fuego Volcano, Guatemala. *Am Mineral* 69:660-676
- Bacon CR, Hirschmann MM (1988) Mg/Mn partitioning as a test for equilibrium between coexisting Fe-Ti oxides. *Am Mineral* 73:57-61
- Bindeman IN, Davis AM, Drake MJ (1998) Ion microprobe study of plagioclase basalt partition experiments at natural concentration levels of trace elements. *Geochim Cosmochim Acta* 62:1175-1193
- Bindeman IN, Davis AM (2000) Trace element partitioning between plagioclase and melt: Investigation of dopant influence on partition behavior. *Geochim Cosmochim Acta* 64:863-878
- Blatter DL, Carmichael ISE (1998) Plagioclase-free andesites from Zitácuaro (Michoacán), Mexico: petrology and experimental constraints. *Contrib Mineral Petrol* 132:121-138
- Blatter DL, Carmichael ISE (2001) Hydrous phase equilibria of a Mexican high-silica andesite: A candidate for a mantle origin? *Geochim Cosmochim Acta* 65:4043-4065

- Blundy J, Cashman K (2005) Rapid decompression-driven crystallization recorded by melt inclusions from Mount St. Helens volcano. *Geology* 33:793-796
- Blundy J, Cashman K (2008) Petrologic Reconstruction of Magmatic System Variables and Processes. In: Putirka KD, Tepley FJ (eds) *Minerals, Inclusions and Volcanic Processes*. Mineral Soc Am Rev Mineral 69:179-239
- Blundy J, Wood J (1991) Crystal-chemical controls on the partitioning of Sr and Ba between plagioclase feldspar, silicate melts, and hydrothermal solutions. *Geochim Cosmochim Acta* 55:193-209
- Brophy JG, Whittington CS, Park YR (1999) Sector-zoned augite megacrysts in Aleutian high alumina basalts: implications for the conditions of basalt crystallization and the generation of calc-alkaline series magmas. *Contrib Mineral Petrol* 135, 277-290
- Brugger CR, Hammer JE (2010) Crystallization kinetics in continuous decompression experiments: Implications for interpreting natural magma ascent processes. *J Petrol* 51:1941-1965
- Brugisser A, Scaillet B (2007) Redox evolution of a degassing magma rising to the surface. *Nature* 445:194-197
- Cashman K, Blundy J (2000) Degassing and crystallization of ascending andesite and dacite. *Philos trans R Soc London Series A- Math Phys and Engin Sci* 258:1487-1513
- Chase MW (1998) NIST-JANAF thermochemical tables, fourth edition. *J Phys Chem Ref Data*, Monograph Springer: Heidelberg 9
- Chesner CA (1998) Petrogenesis of the Toba Tuffs, Sumatra, Indonesia. *J Petrol* 39:397-438.
- Coombs ML, Gardner JE (2001) Shallow-storage conditions for the rhyolite of the 1912 eruption at Novarupta, Alaska. *Geology* 29:775-778
- Costa F, Scaillet B, Pichavant M (2004) Petrological and experimental Constraints on the Pre-eruption Conditions of Holocene Dacite from Volcán San Pedro (36°S, Chilean Andes) and the Importance of Sulphur in Silicic Subduction-related Magmas. *J Petrol* 45:855-881
- Couch S, Harford CL, Sparks RSJ, Carroll MR (2003a) Experimental constraints on the conditions of formation of highly calcic plagioclase microlites at the Soufriere Hills Volcano, Montserrat. *J Petrol* 44: 1455-1475
- Couch S, Sparks RSJ, Carroll MR (2003b) The kinetics of degassing-induced crystallization at Soufriere Hills Volcano, Montserrat. *J Petrol* 44:1477-1502
- Crabtree SM, Lange RA (2011) Complex Phenocryst Textures and Zoning Patterns in Andesites and Dacites: Evidence of Degassing-Induced Rapid Crystallization? *J Petrol* 52:3-38
- Deering CD, Cole JW, Vogel TA (2011) Extraction of crystal-poor rhyolite from a hornblende-bearing intermediate mush: a case study of the caldera-forming

- Matahina eruption, Okataina volcanic complex. *Contrib Mineral Petrol* 161:129-151
- Dunbar NW, Hervig RL, Kyle PR (1989) Determination of pre-eruptive H₂O, F and Cl contents of silicic magmas using melt inclusions- examples from Taupo Volcanic Center, New Zealand. *Bull Volcanol* 51:177-184
- Eichelberger JC, Westrich HR (1981) Magmatic volatiles in explosive rhyolitic eruptions. *Geophysical Research* 8:757-760
- Faure F, Trolliard G, Nicollet C (2003) A developmental model of livine morphology as a function of the cooling rate and the degree of undercooling. *Contrib Mineral Petrol* 145:251-263
- Frey HM, Lange RA (2011) Phenocryst complexity in andesites and dacites from the Tequila volcanic field, Mexico: resolving the effects of degassing vs. magma mixing. *Contrib Mineral Petrol* 162:415-445
- Gardner JE, Rutherford M, Carey S, Sigurdsson H (1995) Experimental constraints of pre-eruptive water contents and changing magma storage prior to explosive eruptions of Mount St Helens volcano. *Bull Volcanol* 55:1-17.
- Ghiorso M, Evans BW (2008) Thermodynamics of rhombohedral oxide solid solutions and a revision of the Fe-Ti two-oxide geothermometer and oxygen barometer. *Am J Sci* 308:957-1039
- Grove TL, Elkins-Tanton LT, Parman SW, Chatterjee N, Mütener O, Gaetani GA (2003) Fractional crystallization and mantle-melting controls on calc-alkaline differentiation trends. *Contrib Mineral Petrol* 145:515-533
- Hammer JE (2006) Influence of fO₂ and cooling rate on the kinetics and energetics of Fe-rich basalt crystallization. *Earth Planet Sci Lett* 248:618-637
- Hammer JE, Rutherford MJ (2002) An experimental study of the kinetics of decompression-induced crystallization in silicic melt. *J Geophys Res* 107(B1): 2021
- Hammer JE, Sharp TG, Wessel P (2010) Heterogeneous nucleation and epitaxial crystal growth of magmatic minerals. *Geology* 38:367-370
- Harris JM (1986) Silicic volcanics of Volcán Tequila, Jalisco, Mexico. MS thesis, University of California
- Holtz F, Sato H, Lewis J, Behrens H, Nakada S (2005) Experimental Petrology of the 1991-1995 Unzen Dacite, Japan. Part I: Phase Relations, Phase Compositions and Pre-eruptive Conditions. *J Petrol* 46:319-337
- Hui J, Zhang Y (2007) Toward a general viscosity equation for natural anhydrous and hydrous silicate melts. *Geochim Cosmochim Acta* 71:403-416
- Johannes W, Koepke J, Behrens H (1994) Partial melting reactions of plagioclase and plagioclase-bearing assemblages. In: Parson, I. (ed.) *Feldspars and their Reactions*. Dordrecht: Kluwer, pp 161-194

- Johnson ER, Kamenetsky VS, McPhie J (2011) Degassing of the H₂O rich rhyolites of the Okataina Volcanic Center, Taupo Volcanic Zone, New Zealand. *Geology* 39:311-314
- Kirkpatrick RJ (1975). Crystal growth from the melt: A review. *Am Mineral* 60:798-814
- Kirkpatrick RJ, Kuo LC, Melchior J (1981) Crystal growth in incongruently-melting compositions: programmed cooling experiments with diopside. *Am Mineral* 66:223–241
- Kress V, Carmichael ISE (1991) The compressibility of silicate liquids containing Fe₂O₃ and the effect of composition, temperature, oxygen fugacity and pressure on their redox states. *Contrib Mineral Petrol* 108:82-92
- Lange RA (1997) A revised model for the density and thermal expansivity of K₂O-Na₂O-CaO-MgO-Al₂O₃-SiO₂ liquids from 700-1900 K: extension to crustal magmatic temperatures: *Contrib Mineral Petrol* 110: 311-320
- Lange RA, Frey HM, Hector J (2009) A thermodynamic model for the plagioclase-liquid hygrometer/thermometer. *Am Mineral* 94:494-506
- Lange RA, Navrotsky A (1993) The heat capacity of Fe₂O₃-bearing silicate liquids: *Contrib Mineral Petrol* 110: 311-320
- Lange RA, Waters, LE, Andrews, BJ (2012) A newly calibrated plagioclase-liquid hygrometer or rhyolites. Assessing the Role of Crystallization and Degassing on the Evolution of Magmatic-Hydrothermal Systems: Cosponsored by MSA II: American Geophysical Union Fall Meeting
- Larsen JF (2005) Experimental study of plagioclase rim growths around anorthite seed crystals in rhyodacite melt. *Am Mineral* 90:417-427
- Liu Y, Anderson AT, Wilson CJN (2006) Mixing and differentiation in the Oruanui rhyolitic magma, Taupo, New Zealand: evidence from volatiles and trace elements in melt inclusions. *Contrib Mineral Petrol* 151:71-87
- Liu Y, Zhang Y, Behrens H (2005) Solubility of H₂O in rhyolitic melts at low pressure and a new empirical model for mixed H₂O CO₂ solubility in rhyolitic melts. *J Volcanol Geotherm Res* 143:219-235
- Lofgren G (1974) An experimental study of plagioclase crystal morphology: isothermal crystallization. *Am J Sci* 274:243-273
- Loomis TP (1981) An investigation of disequilibrium growth processes of plagioclase in the system anorthite-albite-water by methods of numerical simulation. *Contrib Mineral Petrol* 81:230-239
- Lowenstern JB (1993) Evidence for a copper-bearing fluid in magma erupted at the Valley of Ten-Thousand-Smokes, Alaska. *Contrib Mineral Petrol* 114:409-421
- Lowenstern JB (1994) Dissolved volatile concentrations in an ore-forming magma. *Geology* 22:893-896
- Luhr J (2000) The geology and petrology of Volcán San Juan (Nayarite, Mexico) and the compositionally zoned Tepic Pumic. *J Volcanol Geotherm Res* 95:109-156

- Martel C, Schmidt BC (2003). Decompression experiments as an insight into ascent rates of silicic magmas. *Contrib Mineral Petrol* 144, 397-415
- Martel C, Pichavant M, Holtz F, Scaillet B, Bourdier JL, Traineau H (1999) Effects of fO_2 and H_2O on andesite phase relations between 2 and 4 kbar. *J Geophys Res* 104:453-470
- McCanta MC, Rutherford MJ, Hammer JE (2007) Pre-eruptive and syn-eruptive conditions in the Black Butte, California dacite: Insight into crystallization kinetics in a silicic magma system. *J Volcanol Geotherm Res* 160:263-284
- Meiling GS, Uhlmann DR (1967) Crystallization and melting kinetics of sodium disilicate. *Phys Chem Glasses* 8: 62-68
- Moore G, Carmichael ISE (1998) The hydrous phase equilibria (to 3 kbar) of an andesitic and basaltic andesite from western Mexico: constraints on water content and conditions of phenocryst growth. *Contrib Mineral Petrol* 130:304-319
- Nakada S, Bacon CR, Gartner A (1994) Origin of Phenocrysts and Compositional diversity in Pre-Mazama Rhyodacite Lavas, Crater Lake, Oregon. *J Petrol* 35:127-162
- Nakamura M, Shimakita S (1998) Dissolution origin and syn-entrapment compositional change of melt inclusion in plagioclase. *Earth Planet Sci Lett* 161:119-133
- Nelson ST, Montana A (1992) Sieve-textured plagioclase in volcanic rocks produced by rapid decompression. *Am Mineral* 77:1242-1249
- Newman S, Lowenstern JB (2002) VOLATILECALC: a silicate melt- H_2O - CO_2 solution model written in Visual Basic for excel. *Comp and Geosci* 28:597-604
- Ochs FA, Lange RA (1999) The density of hydrous magmatic liquids: *Science* 283: 1314-1317.
- O'Hara S, Tarshis LA, Tiller WA, Hunt JP (1968). Discussion of interface stability of large facets on solution grown crystals. *J Crystal Growth* 3-4:535-561
- Pallister JS, Hoblitt RP, Crandell DR (1992) Mount St. Helens a decade after the 1980 eruptions- magmatic models, chemical-cycles, and a revised hazards assessment. *Bull Volcanol* 54:124-146
- Pichavant M, Mysen BO, Macdonald R (2001) Source and H_2O content of high-MgO magmas in island arc settings: An experimental study of a primitive calc-alkaline basalt from St. Vincent, Lesser Antilles arc. *Geochim Cosmochim Acta* 66:2193-2209
- Putirka KD (2005) Igneous thermometers and barometers based on plagioclase + liquids equilibria: Tests of some existing models and new calibrations. *Am Mineral* 90:336-346
- Roeder PR, Poustovetov A, Oskarsson N (2001) Growth forms and composition of chromian spinel in MORB magma: Diffusion-controlled crystallization of chromian spinel. *The Canadian Mineral* 39:397-416

- Ruprecht P, Bergantz GM, Cooper KM (2012) The Crustal Magma Storage System of Volcan Quizapu, Chile, and the Effects of Magma Mixing on Magma Diversity. *J Petrol* 53:801-840
- Sakuyuma M (1979) Evidence of Magma Mixing: petrological Study of Shirouma-Oike Calc-alkaline Andesite Volcano, Japan. *J Volcanol Geotherm Res* 18:179-208
- Salisbury MJ, Bohron WA, Clynne MA (2008) Multiple Plagioclase Crystal Populations Identified by Crystal Size Distribution and in situ Chemical Data: Implications for Timescales of Magma Chamber Processes Associated with the 1915 Eruption of Lassen Peak, CA. *J Petrol* 49:1755-1780
- Scaillet B, Evans BW (1999) The 15 June 1991 Eruption of Mount Pinatubo. I. Phase Equilibria and Pre-eruption P-T-fO₂-fH₂O Conditions of the Dacite Magma. *J Petrol* 40:381-411.
- Sekerka RF (1993) Role of instabilities in determination of the shapes of growing crystals. *J Crystal Growth* 128:1-12
- Smith V, Shane P, Nairn I (2010) Insights into silicic melt generation using plagioclase, quartz and melt inclusions from the caldera-forming Rotoiti eruption, Taupo volcanic zone, New Zealand. *Contrib Mineral Petrol* 160:951-971
- Spera FJ (2000) Physical properties of magmas, in Sigurdsson H, Houghton B, McNutt SR, Rymer H, Stix J (eds), *Encyclopedia of Volcanoes*: Academic Press, San Diego, 171-190
- Szramek L, Gardner JE, Larsen JF (2006) Degassing and microlite crystallizations of basaltic andesite magma erupting at Arenal volcano, Costa Rica. *J Volcanol Geotherm Res* 157:182-201
- Suzuki Y, Gardner JE, Larsen, JF (2007) Degassing and microlite crystallization of basaltic andesite magma erupting at Arenal volcano, Costa Rica. *J Volcanol Geotherm Res* 69:423-459
- Tepley FJ, Davidson JP, Clynne MA (1999) Magmatic interactions as recorded in plagioclase phenocrysts of Chaos Crags, Lassen Volcanic Center, California. *J Petrol* 40: 787-806
- Tomiya A, Takahashi E, Furukawa N, Suzuki T (2010) Depth and Evolution of a Silicic Magma Chamber: Melting Experiments of a Low-K Rhyolite from Usu Volcano, Japan. *J Petrol* 51:1333-1354
- Tsuchiyama A (1985) Dissolution kinetics of plagioclase in the melt of the system diopside-albite-anorthite and origin of dusty plagioclase in andesites. *Contrib Mineral Petrol* 89:1-16
- Tuttle OF, Bowen NL (1958) Origin of granite in the light of experimental studies in the system NaAlSi₃O₈-KAlSi₃O₈-SiO₂-H₂O. *Geol Soc Am Mem* 74: 153 pp
- Wallace PJ, Anderson AT, Davis AM (1999) Gradients in H₂O, CO₂, and exsolved gas in a large-volume silicic magma system: Interpreting the record preserved in melt inclusions from the Bishop Tuff. *J Geophys Res-Sol Earth* 104:20097-20122

- Wallace PJ, Carmichael ISE (1994) Petrology of Volcan-Tequila, Jalisco, Mexico- Disequilibrium phenocryst assemblages and evolution of the subvolcanic magma system. *Contrib Mineral Petrol* 117:345-361
- Waters LE, Andrews BJ, Lange RA (2012) Water-saturated phase-equilibrium experiments on rhyolite and dacite obsidians: the effect of variable melt water concentration on the composition of phenocrysts. *Assessing the Role of Crystallization and Degassing on the Evolution of Magmatic-Hydrothermal Systems: Cosponsored by MSA II: American Geophysical Union Fall Meeting*
- Watts RB, de Silva SL, de Rios GJ (1999) Effusive eruption of viscous silicic magma triggered and driven by recharge: a case study of the Cerro Chascon-Runtu Jarita Dome Complex in Southwest Bolivia. *Bull Volcanol* 61:241-264
- Westrich HR, Eichelberger JC, Hervig RL (1991) Degassing of the 1912 Katmai Magmas. *Geophys Res Lett* 18:1561-1564
- Zhao SR, Liu R, Wang QW, Xu H, Fang M (2011) Skeletal morphologies and crystallographic orientations of olivine, diopside and plagioclase. *J Crystal Growth* 318:135-140

CHAPTER III

NO EFFECT OF DEGASSING OF H₂O ON THE FE³⁺/FE²⁺ OF RHYOLITE OBSIDIANS

3.1 ABSTRACT

In this study a comparison is made between the pre-eruptive (pre-degassing) and post-eruptive (post-degassing) Fe²⁺ concentrations in six phenocryst-poor (<5%) glassy obsidians. Pre-eruptive Fe²⁺ concentrations were determined by incorporating temperatures and Δ NNO values for each sample, obtained by ilmenite-titanomagnetite geo-thermometry, into the experimentally calibrated equation of Kress & Carmichael (1991). Pre-eruptive dissolved H₂O contents were calculated by incorporating the pre-eruptive temperatures, the most calcic plagioclase phenocrysts found in each sample, and the whole rock compositions into a modified version of the plagioclase-liquid hygrometer of Lange et al. (2009). Maximum calculated pre-eruptive H₂O contents range from 2.4 to 5.1 wt%; therefore, both the oxidation state and dissolved H₂O concentrations are known prior to eruption at the time of phenocryst growth. After eruption, the rhyolites lost nearly all of their volatiles as indicated by low loss on ignition values (LOI < 0.7 wt%). In order to test how much oxidation of ferrous iron occurred as a consequence of degassing, the ferrous iron concentration in the bulk samples was measured by titration. The results of this study indicate that no detectable change within analytical error, between pre-and post-eruptive FeO concentrations, which range from 0.95-1.58 wt%

FeO, with an average deviation of 0.09 wt% and a maximum deviation of 0.15 wt%, suggesting that H₂O degassing has no effect on the redox state of these systems.

3.2 INTRODUCTION

The oxidation state of a magma is determined by the oxygen fugacity (fO_2), which also controls the valence state of heterovalent ions (e.g., Fe, S, Mn, Sn, V, Ti). An example of the effect of fO_2 on ferrous iron in the melt is shown in Equation 3.1:



And hence the ratio of ferric to ferrous iron reflects the oxidation state of the magma.

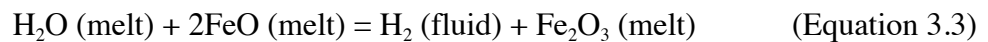
It has been proposed that open- or closed- system degassing of mixed H-C-S-O-Cl fluids may induce either oxidation or reduction of a magma, and thus change its ferric-ferrous ratio (e.g., Maclean 1969; Whitney et al., 1985; Koder et al. 1998; Maretta and Papale, 2004; Evans 2006; Dolejjs and Wagner 2008; Jugo 2009; Jugo et al. 2010; Webster et al. 2011; Bell and Simon, 2011). Observations of magnetite in fluid inclusions in plutons (Whitney et al., 1985), sulfides and sulfate occurring in melt inclusions and groundmass, respectively (e.g., Pinatubo), have lead to hypotheses that explain apparent changes in redox state of a melt/magma by the exsolution of a volatile phase during decompression (e.g., Burgisser and Scaillet, 2007).

Experimental studies and theoretical models (e.g., Dolejjs and Wagner, 2007; Bell and Simon, 2011) provide evidence that a Cl-rich volatile phase exsolved from a melt is capable of removing ferrous iron from the melt to the fluid phase, resulting in an oxidizing effect on the melt phase (via increases in Fe^{3+}/Fe^{2+}). In contrast, degassing of S₂ from a melt to a fluid phase can result in the reduction of ferric iron into ferrous iron

(Carmichael, 1991). Partitioning behavior of sulfur between melt and fluid phases is complex as it is dependent on speciation of sulfur in the melt, which is also dependent on the fO_2 of the system (Scaillet et al., 1998). A third commonly invoked mechanism that may alter the redox state of a magma/melt is by increasing the fO_2 of the melt by the disassociation of H_2O , shown in the homogenous reaction in Equation 3.2.



The effect of degassing of H_2O on the ferric-ferrous ratio of the melt is investigated in a theoretical study by Candela (1986) based on the heterogeneous reaction shown in Equation 3.3.



The dissociation of H_2O to form H_2 in the fluid phase and Fe_2O_3 in the melt phase is dependent on the initial fO_2 of the melt (Equations 3.1 and 3.2), thus the ability of dissolved H_2O to oxidize ferrous iron in the melt is dependent on the initial fO_2 of the system. Additionally, if H_2 in equation 3.3 remained in the melt phase, no increased oxidation of the melt would occur. If closed-system degassing of H_2 from the melt to a vapor phase occurred, where the melt and vapor phase is in equilibrium with the melt, there will be no increase in oxidation state. In contrast, an increase in the oxidation state (an increase in the ratio of ferric-ferrous iron) of a melt is required if H_2 is preferentially lost from *both* the fluid and melt phases.

Experimental studies from the literature that investigated the effect dissolved melt H_2O on the ferric-ferrous ratio (Sisson and Grove, 1993; Moore et al., 1995; Gaillard et al., 2001; Wilke et al., 2002; Gaillard et al., 2003; Botcharnikov et al., 2005) have conflicting results. In phase equilibrium experiments where oxygen fugacity was buffered

or monitored, Gaillard et al. (2001, 2003) demonstrate that H₂O increases the activity of FeO and decreases the activity of Fe₂O₃, where the fO₂ of the system is $\leq \Delta \text{NNO} - 0.8$. In a Mössbauer spectral study, Wilke et al. (2002) demonstrate that dissolved H₂O increases activity of Fe₂O₃ relative to FeO in hydrous tonalite melts under fO₂ conditions ranging from air, Cu-Cu₂O, hematite-magnetite, and C-O-H buffers. These results contrast with the experimental studies of Moore et al. (1995) and Botcharnikov et al. (2005). In a series of H₂O-saturated experiments, where log(fO₂) ranges from -0.68 to -10.4, Moore et al. (1995) compared the ferric-ferrous ratios measured in the hydrous rhyolite and basalt glasses, respectively, to ferric-ferrous ratios calculated with the anhydrous equation of Kress and Carmichael (1991). Botcharnikov et al. (2005) demonstrated that H₂O has no effect on the ferric-ferrous ratio in a series of experiments where fO₂ range from less than the QFM to as great as the Mn-MnO buffers. Both studies demonstrate that Kress and Carmichael (1991) accurately predicted ferric-ferrous ratios in H₂O-saturated liquids, which supports the hypothesis that dissolved melt H₂O has no chemical effect on the homogeneous ferric-ferrous equilibrium. The conclusions of Moore et al. (1995) and Botcharnikov et al. (2005) are supported by the JANAF tables (Chase et al. 1998), which report small positive and negative Gibbs free energies for the exchange of OH⁻ groups and Fe³⁺ and Fe²⁺, respectively.

A true test of the effect of degassing of H₂O on the oxidation state requires a measurement of a pre- and post-eruptive indicator of redox state (e.g., ferrous iron), and the results will reveal whether or not the oxidation states of magmas are altered during degassing or if they are reflective of the source region. In a micro-XANES study of Fe³⁺/Fe²⁺ in olivine hosted melt inclusion from arc basalts, Kelly and Cottrell (2009)

demonstrates that degassing of dissolved melt H_2O does not impose a change on $f\text{O}_2$, but rather that the oxidation states of magmas are reflective of the source region, as proposed by Carmichael (1991). The results of Kelly and Cottrell (2009) are supported by the results of Crabtree and Lange (2012), which demonstrated that degassing of H_2O exerts no change in the pre-eruptive and post-eruptive concentrations of FeO in andesites and dacites. In this study, the pre-eruptive ferrous iron concentrations of six rhyolite obsidians are determined with the temperatures and $f\text{O}_2$ recorded by iron oxides, which crystallized during water saturated conditions, and are compared to the post-eruptive ferrous iron concentrations measured directly by titration.

3.3 SAMPLE DESCRIPTION

Samples used in this study are rhyolite obsidians from Western Mexico and Medicine Lake Volcano, CA that were the subjects of a detailed electron microprobe study (Waters and Lange, 2013), where pre-eruptive temperatures, $f\text{O}_2$, and water contents were calculated for each sample. The obsidians have a glassy matrix with sparse phenocryst (grains $>50 \mu\text{m}$) mode totals that are low (1.6-6.4%). The obsidians are minimally saturated with five phases: plagioclase, orthopyroxene, titanomagnetite, ilmenite, apatite. All samples are fresh and show no sign of secondary alteration (Appendix B Figure B1).

3.4 METHODOLOGY

Samples were powdered and analyzed for major element chemistry by inductively coupled plasma analysis at Activation Laboratories in Ancaster, Ontario. Analyses for the obsidian samples from this study are included in Table 3.1.

A two-fold strategy is employed to determine pre-eruptive FeO concentration. (1)

Pre-eruptive oxygen fugacity and temperature are calculated using the compositions of

Table 3.1 Whole-rock major element compositions

Sample	MLV-37	MLV-36	CAM-49	TEQ-21	JAL-10	COMP-3
Lat. (N)	41° 34.28'	41° 36.97'		20° 51.26'	21° 16.68'	21° 09.79'
Long. (W)	121° 41.96'	121° 38.48'		103° 51.86'	104° 41.86'	104° 42.39'
SiO ₂	74.5	73.8	72.9	74.1	74.3	75.2
TiO ₂	0.28	0.27	0.28	0.15	0.26	0.2
Al ₂ O ₃	13.6	13.2	13.2	13.3	14.2	13.5
FeO ^T	2.12	2.08	2.01	1.62	1.5	1.13
MnO	0.04	0.04	0.04	0.06	0.06	0.05
MgO	0.28	0.27	0.29	0.11	0.38	0.3
CaO	1.25	1.23	1.29	0.51	1.4	1.3
Na ₂ O	4	3.99	4.02	4.61	4.86	4.55
K ₂ O	4.21	4.18	4.18	4.83	3.04	3.36
P ₂ O ₅	0.05	0.06	0.04	0.03	0.07	0.06
LOI	0.4	0.31	0.3	0	0	0.7
Total	100.7	99.41	98.62	99.36	100.07	99.65
Plag ph	1.80%	1.80%	1.50%	0.70%	3.50%	1.40%
mph	0.70%	0.10%	1.00%	1.30%	1.90%	0.30%
Opx ph	0.40%	0.40%	0.10%	-	0.20%	0.10%
mph	0.40%	0.20%	0.70%	<0.1%	0.20%	0.20%
Cpx ph	-	-	-	-	-	-
mph	-	-	0.10%	0.10%	-	-
Hbl	0.10%	-	-	-	0.20%	0.20%
Fe-Ti Ox	0.30%	0.30%	0.20%	0.60%	0.50%	0.50%
Gdms	96.30%	97.10%	96.20%	97.10%	93.60%	97.10%
Max X _{An}	53	50.2	53.3	16.6	44.3	50.9
Max wt% H ₂ O	7.5	5.8	6.6	4.2	7.3	7.4

LOI = Loss on ignition

Abundances determined with point counts of 2000 points in triplicate. Abbreviations: Plag, plagioclase; Opx, orthopyroxene; Cpx, clinopyroxene; Hbl, hornblende; Fe-Ti oxides, ilmenite and titanomagnetite; Gdms, groundmass; ph = phenocrysts, crystals with long axis > 200 microns; mph = microphenocrysts, crystals with long axis > 50 microns and < 200 microns; gdms = groundmass; Max X_{An} from Waters and Lange (in review) Max wt% H₂O calculated from the plagioclase-liquid hygrometer of Lange et al. (2009)

co-precipitated iron-titanium oxides and the oxygen barometer and thermometer of Ghiorso and Evans (2008). Crystals of titanomagnetite and ilmenite were analyzed using the CAMECA SX-100 electron microprobe at the University of Michigan, with an accelerating voltage of 15 kV and 15 nA. All possible pairings of ilmenite and titanomagnetite were incorporated into the geo-thermometer/oxy-barometer of Ghiorso and Evans (2008) to determine temperature and fO_2 . The temperature, oxygen fugacity,

and liquid compositions (bulk compositions are used for liquid compositions due to low crystallinities) are then incorporated into the empirically calibrated equation of Kress and Carmichael (1991), which calculates $\text{Fe}^{3+}/\text{Fe}^{2+}$:

$$\ln\left(\frac{X_{\text{Fe}_2\text{O}_3}}{X_{\text{FeO}}}\right) = a \ln(fO_2) + \frac{b}{T} + c + \sum_i d_i X_i \quad (\text{Equation 3.4})$$

(2) Post-eruptive FeO content is measured by direct titration of whole rock using V^{4+} as an indicator of FeO (Wilson 1960). The Fe^{2+} concentrations of Canadian Survey standard, SY-4, and USGS standards, BIR-1a, W-2 and QLO-1, were also measured by back titration (Wilson 1960) to evaluate accuracy, and closely recover the certified values of 2.97 (± 0.05), 8.34 (± 0.10), 8.34 (± 0.09) and 2.86 (± 0.09) wt% FeO, respectively. Crabtree and Lange (2012) demonstrate that titrations following the Wilson (1960) method recover consistent analyses of ferrous iron with a maximum deviation of ± 0.22 wt% FeO. In a comparison of direct titration of wt% FeO (Reichen and Fahey, 1962) and the back titration method (Wilson, 1960), Crabtree and Lange (2012) propose that the Wilson (1960) titration method more accurately recovers the wt% FeO because it does not require normalization to a standard, as in the method described by Reichen and Fahey (1962). Because the calibration of Kress and Carmichael (1991) was measured by colorimetry, Crabtree and Lange (2012) also tested the titration and the colorimetric techniques and demonstrated that both were comparable analytical methods. Lastly, the S content of the groundmass was measured with the electron microprobe to determine if interference with the V^{4+} indicator solution used in the titration was likely to occur (Appendix B Table B1). In all obsidians except MLV-37, the S content of the groundmasses were below detection limit (14 ppm), and in the case of MLV-37, S content was on average 28 ppm and its effect on titrated FeO is negligible.

Determination of Pre-eruptive H₂O, S and Cl Contents

Pre-eruptive H₂O contents were determined in each sample by using the plagioclase-liquid hygrometer model of Lange et al. (2009), and the new calibration for rhyolites (Lange et al., 2012; Waters et al., 2012) (Appendix B Table B2). To apply the plagioclase-liquid hygrometer to each sample, the temperature, liquid composition and plagioclase compositions must be known. The temperatures used in the plagioclase hygrometer are the averages obtained from all possible pairings of ilmenite and titanomagnetite (Table 3.2). The bulk composition (Table 3.1) is used as the liquid composition in the hygrometer due to the low overall crystallinity (<6%) and the glassy nature of the obsidians. Plagioclase compositions used in the hygrometer are reported in Table 3.1 and obtained from Waters and Lange (2013), where a detailed description of the range of plagioclase compositions and accompanying textures in each sample is provided. Sulfur was measured using the CAMECA SX-100 electron microprobe at the University of Michigan, with a defocused 5 μ m beam and accelerating voltage of 15 kV and 40 nA. Chlorine contents of apatites (1-3 wt%) in each sample suggest the melts contained Cl during phenocryst growth. The partition coefficients for Cl between apatite-melt and apatite-fluid are determined by Webster et al. (2009) for rhyolite liquids with ≤ 3 wt% H₂O at temperatures between 900-924°C and are therefore only directly applicable to one of the six samples, TEQ-21, which has a dissolved melt water content of <3 wt% and temperature of 939°C. The pre-eruptive Cl contents for each rhyolite were estimated by using the bulk composition of each obsidian and the Cl solubility model of Webster and De' Vivo (2002). The Cl contents in apatite and groundmasses of the rhyolites were analyzed using the CAMECA SX-100 electron microprobe at the University of Michigan

with a defocused 10 μ m beam and accelerating voltage of 15 kV and 10 nA. Apatites were analyzed following the recommended calibration and beam settings of Henderson (2012), which are optimized to eliminate any compositional effects of axial orientation of the apatites and to minimize any interference of fluorine with the beam during analysis (Stormer et al. 1993; Pyle et al., 2002).

3.5 RESULTS

Pre-eruptive Fe²⁺ determinations

The compositions of all analyzed titanomagnetite and ilmenite grains are presented as plots of log (X_{Mg}/X_{Mn}) magnetite versus log (X_{Mg}/X_{Mn}) ilmenite for all possible pairs for each sample in supplementary material (Appendix B Fig. B2). None of the pairs deviate strongly from the proposed test of equilibrium by Bacon & Hirschmann (1988). Temperature and Δ NNO values, calculated from all possible pairings titanomagnetite and ilmenite analyses in each sample using the geothermometer and oxybarometer of Ghiorso & Evans (2008), are presented in Table 3.2. Plots of temperature and Δ NNO values for all possible pairs of ilmenite and titanomagnetite are presented in the supplementary material (Appendix B Fig. B3). For the six rhyolites, the maximum one standard deviation for temperatures is 25°C. The calculated oxygen fugacity for each sample relative to the Ni-NiO buffer (O'Neill & Pownceby, 1993) is presented in Tables 2 and 3. Pre-eruptive Δ NNO values range from -0.9 ± 0.1 to $+1.4 \pm 0.05$ ($\pm 1\sigma$). Histograms of the Δ NNO values and corresponding wt% FeO concentrations are presented in the supplementary material (Appendix B Fig. B4). The range of temperatures and Δ NNO values derived from the equation of Ghiorso & Evans (2008) results in a small variation in wt% FeO ($\leq 0.05\%$) in the rhyolites when incorporated into

the empirical equation of Kress & Carmichael (1991). The uncertainty in the total iron concentration (± 0.17 wt% FeO^T) is a potential source of error in this calculation and can be evaluated by propagating maximum and minimum possible total iron concentrations through the equation of Kress & Carmichael (1991). Propagating the possible total iron concentration through the equation of Kress & Carmichael results in a maximum error of ± 0.13 wt% on the concentration of ferrous iron.

Table 3.2 Average Fe-Ti oxide compositions

Sample	TEQ21		COMP3		JAL10		MLV36		MLV37		CAM49	
Phase	Ilm											
#	14	$\pm 2\sigma$	8	$\pm 2\sigma$	11	$\pm 2\sigma$	21	$\pm 2\sigma$	15	$\pm 2\sigma$	16	$\pm 2\sigma$
SiO ₂	0.02	0.04	0.06	0.07	0.04	0.06	0.04	0.06	0.1	0.29	0.02	0.04
TiO ₂	47.3	1.33	37.8	2.91	40.1	1.02	45.8	1.25	45.6	0.81	46.3	0.69
Al ₂ O ₃	0.17	0.07	0.32	0.07	0.41	0.49	0.25	0.33	0.16	0.08	0.15	0.04
Fe ₂ O ₃	11.8	2.06	31.1	5.29	27.0	2.08	16.2	2.30	15.4	1.11	13.1	0.98
V ₂ O ₃	0.36	0.08	0.09	0.08	0.06	0.06	0.47	0.10	0.47	0.06	0.14	0.11
Cr ₂ O ₃	0.01	0.05	0.02	0.04	0.02	0.06	0.06	0.06	0.05	0.04	0.06	0.03
FeO	37.1	0.90	27.2	2.24	29.2	2.23	33.9	1.79	35.2	0.85	36.8	0.89
MnO	0.85	0.08	0.74	0.13	0.78	0.09	0.58	0.06	0.63	0.06	0.61	0.06
MgO	1.54	0.14	2.47	0.37	2.35	0.26	2.41	0.33	1.82	0.12	1.98	0.53
CaO	0.06	0.10	0.05	0.08	0.02	0.08	0.03	0.06	0.02	0.05	0.03	0.03
Total	99.2	0.60	99.8	0.67	100.1	1.44	99.8	0.92	99.4	1.06	99.0	0.55
Mol% ilm	81.1	1.51	59.7	4.15	64.1	2.22	74.5	2.22	77.2	1.26	79	0.02
Phase	Mte											
#	7	$\pm 2\sigma$	8	$\pm 2\sigma$	4	$\pm 2\sigma$	9	$\pm 2\sigma$	4	$\pm 2\sigma$	11	$\pm 2\sigma$
SiO ₂	0.07	0.09	0.07	0.03	0.12	0.02	0.09	0.06	0.17	0.01	0.11	0.08
TiO ₂	17.6	1.51	5.67	0.48	5.68	1.58	10.9	0.21	9.41	1.17	11.5	2.92
Al ₂ O ₃	1.74	0.21	2.23	0.08	2.36	0.16	2.19	0.22	1.98	0.63	1.87	0.20
Fe ₂ O ₃	32.9	2.50	56.2	0.77	56.0	2.80	44.8	0.54	47.6	0.64	44.0	4.95
V ₂ O ₃	0.3	0.06	0.28	0.05	0.19	0.25	1.07	0.09	0.32	0.20	0.42	0.10
Cr ₂ O ₃	0.02	0.04	0.03	0.05	0.02	0.03	0.13	0.12	0.15	0.37	0.01	0.03
FeO	45.3	1.50	33.9	0.65	34.4	1.27	38.9	0.24	37.3	1.08	39.5	1.30
MnO	0.71	0.07	0.64	0.04	0.66	0.07	0.47	0.05	0.49	0.13	0.45	0.06
MgO	1.07	0.11	1.58	0.12	1.3	0.42	1.42	0.08	1.17	0.44	1.21	0.29
CaO	0.02	0.05	0.01	0.02	0.02	0.06	0.03	0.02	0.1	0.14	0.02	0.07
Total	99.7	1.07	100.6	0.69	100.5	0.54	99.9	0.81	98.7	0.24	99.1	1.13
Mol% ulv	49.3	4.00	15.9	5.04	15.9	4.27	30.3	0.64	26.8	4.91	32.5	7.95
T (°C)	940	36	801	16	779	50	852	24	813	20	849	50
Δ NNO	-0.40	0.4	1.41	0.14	1.35	0.38	0.28	0.5	0.36	0.28	0.19	0.36

Ilm = Ilmenite; Mte = titanomagnetite

Wet chemistry determinations of post-eruptive Fe^{2+}

Results of the titrations of the rhyolites and standards are presented in Table 3.3. FeO concentrations range from 0.95-1.57wt% with 2σ errors <0.15 . All standards were recovered within a 2σ error of their reported values, with the exception of USGS standard SY-4. The titrated wt% FeO value for SY-4 from this study is 2.91 ± 0.1 , and the wt% FeO values for SY-4 reported by the USGS are 2.97 ± 0.05 .

Table 3.3 Measurements of wt% FeO and Δ NNO by different techniques

	Total Iron ¹ wt% FeO ^r	Fe-Ti Oxides (Pre-eruptive) wt% FeO $\pm 2\sigma$	Fe-Ti Oxides (Pre-eruptive) Δ NNO $\pm 2\sigma$	Back-Titration (Wilson, 1960) (Pre-eruptive) wt% FeO $\pm 2\sigma$	Back-Titration (Pre-eruptive) Δ NNO $\pm 2\sigma$	Δ wt% FeO ²
TEQ-21	1.62	1.31 ± 0.02	-0.39 ± 0.20	1.27 ± 0.06	-0.04 ± 0.49	0.04
COMP-3	1.13	0.95 ± 0.03	1.41 ± 0.07	0.95 ± 0.15	1.44 ± 1.00	0.00
JAL-10	1.50	0.98 ± 0.03	1.35 ± 0.19	1.00 ± 0.08	1.25 ± 0.53	-0.01
MLV-36	2.08	1.58 ± 0.04	0.27 ± 0.26	1.54 ± 0.02	0.52 ± 0.11	0.04
MLV-37	2.12	1.58 ± 0.03	0.36 ± 0.14	1.57 ± 0.09	0.48 ± 0.49	0.01
CAM-49	2.01	1.54 ± 0.03	0.19 ± 0.18	1.52 ± 0.15	0.3 ± 0.92	0.02
Standards		Certified wt% FeO		Back-Titration wt% FeO		Δ wt% FeO ³
BIR-1a		8.34 ± 0.10		8.33 ± 0.07		-0.01
QLO-1		2.86 ± 0.09		3.03 ± 0.20		0.06
SY-4		2.97 ± 0.05		2.91 ± 0.10		0.05
W-2a		8.34 ± 0.09		8.32 ± 0.21		-0.02

Recommended wt% FeO results are bolded (see text). All analyses performed in duplicate.

Δ NNO = $\log fO_2(\text{sample}) - \log fO_2(\text{Ni-NiO buffer})$ at temperature reported in Table 3.2

1: wt% FeO (FeTi oxides) - wt% FeO (back titration); pre- vs. post-eruptive wt% FeO

2: wt% FeO (back titration - certified value)

H_2O , S and Cl Concentrations

Estimated maximum melt water concentrations at the time of phenocryst growth are based on the most calcic plagioclase phenocryst in each rhyolite and range from 2.6-6.5 wt% H_2O (Table 3.1). According to the detailed experiments of Clemente et al. (2004), sulfide and sulfate solubility in rhyolite magmas is low (<20 ppm) over the range of temperatures and Δ NNO values observed in this study (Table 3.2), which means that if sulfide or sulfate were present in these magmas, it would have been in very low

concentrations. An additional line of evidence supporting low sulfide and sulfate concentrations is the absence of pyrrhotite as an accessory phase in five of the six samples. Modeled Cl contents are calculated incorporating the whole rock compositions (Table 3.1) into the Cl solubility model of Webster and De'vivo (2002) and range from 3600-6000 ppm (Appendix B Table B3). Measured Cl contents in groundmass glasses range from 580-900 ppm Cl (Appendix B Table B3).

3.6 DISCUSSION: PRE-ERUPTIVE AND POST-ERUPTIVE Fe^{2+}

Pre-eruptive and post-eruptive Fe^{2+} compositions (as wt% FeO) are compared in Figure 3.1, along with a 1:1 correspondence line. The six obsidians fall on the 1:1 correspondence line, and the average deviation between the pre- and post- eruptive oxidation states is ± 0.02 wt% FeO. This small error can be attributed to the presence of both ilmenite and titanomagnetite as liquidus phases (Carmichael, 1967; Carmichael, 1991), which yields precise temperatures and ΔNNO values from the model of Ghiorso & Evans (2008).

The absence of change in the oxidation states of the rhyolites, after degassing of < 6.5 wt% H_2O , illustrates that the equation of Kress & Carmichael (1991) can be used in conjunction with the temperature and ΔNNO values derived from the geothermometer and oxybarometer of Ghiorso & Evans (2008), to produce valid and precise measurements of the ferric-ferrous ratios in magmatic liquids. Even though the measurements of post-eruptive FeO for the rhyolites are in good agreement with the wt% FeO determined from the equation of Kress & Carmichael (1991), the standard deviations

of results of multiple titrations (≤ 0.15 wt% FeO) are large enough to produce significant error in back-calculated values of ΔNNO (± 1 ΔNNO), which are determined by

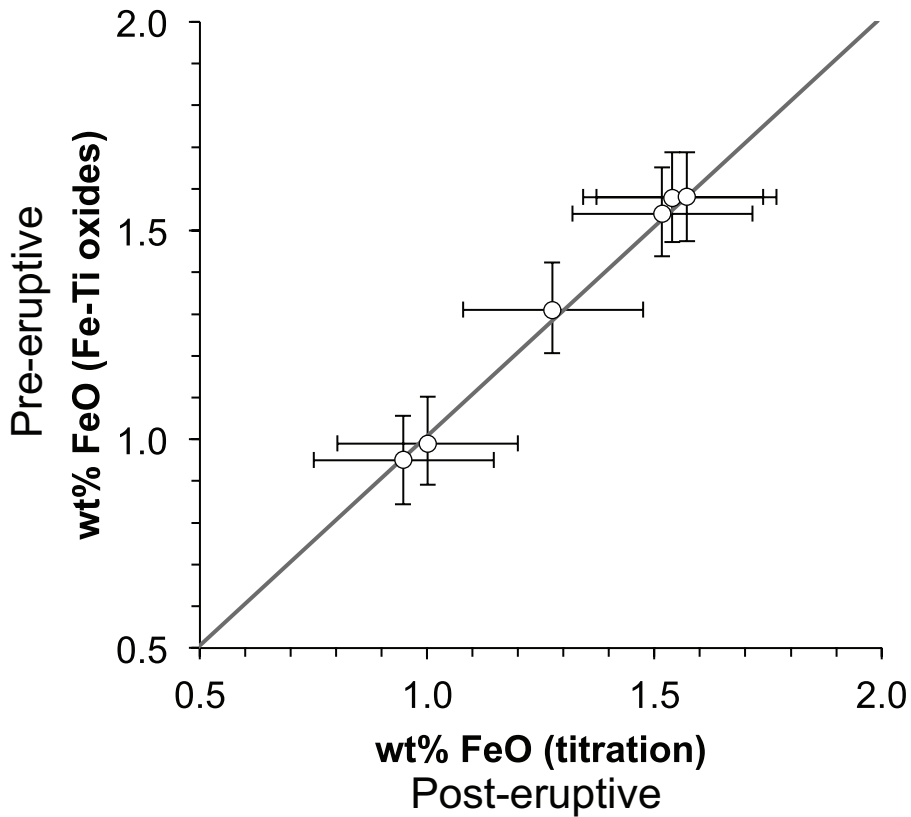


Figure 3.1: A plot of pre-eruptive wt% FeO (derived from Fe-Ti oxides and the geothermometer/barometer of Ghiorso & Evans 2008) and post-eruptive wt% FeO (from titrations (Wilson 1960)) with a 1:1 correspondence line. Solid circles are samples presented in Crabtree & Lange (2011), and white circles are the rhyolites and basaltic andesite presented in this study. The error bars presented for the post-eruptive wt% FeO represent the maximum error on the titrations (± 0.2 wt% FeO). The error bars presented for the pre-eruptive wt% FeO represent the maximum error from the results of all possible pairings of the iron-oxides combined with the uncertainty in total iron (see text; Crabtree & Lange 2011) (± 0.14 wt% FeO).

incorporating the wt% FeO result from the titration into the model equation of Kress & Carmichael (1991). For example, COMP-3 has a pre-eruptive ΔNNO value recorded by the ilmenite and titanomagnetite of $+1.4 \pm 0.2$ (two-S.D.), whereas the back-calculated ΔNNO value is $+1.44 \pm 1.0$ (two-S.D.) and the large error of ± 1 log unit ΔNNO is the result, when considering the range of ferrous iron concentrations possible given the two

standard deviations in wt% FeO (± 0.15) from titrations. The titrations of the rhyolite obsidians have 2σ standard deviations for the titrations ranging from ± 0.02 to 0.15 wt% FeO, which result in back calculated values of ΔNNO values with errors that range from ± 0.11 to ± 1.0 .

Based on the results of the hygrometer (Table 3.1), all samples presented in this study were water saturated prior to eruption and low LOI values (0.0-0.7) indicate that nearly complete degassing occurred during eruption. Fig. 3.1 provides evidence that nearly complete degassing of ~ 2.6 - 6.5 wt% H_2O produces no resolvable change in the pre-eruptive and post-eruptive Fe^{2+} concentrations in rhyolites with total iron concentrations that range from 1.13-2.12 wt%.

Waters & Lange (2013) proposed that all crystallization in the six obsidians presented in this study was due to degassing induced crystallization, which implies that the iron oxides also crystallized over a range of melt water concentrations. All possible pairings of ilmenite and titanomagnetite yield relatively small ranges in temperatures and ΔNNO values, which results in a small range in wt% FeO when incorporated into the model equation of Kress & Carmichael (1991); thus, it is likely that the iron oxides are unaffected by the degassing of water from the melt. An absence of an effect of dissolved melt water on the iron oxides is explained by competing hydration reactions between hydroxyl groups and various dissolved cations in melt. The addition of hydroxyl groups into melt affects the activities of cations, and based on the free energies there is clear, preferential pairing between hydroxyl groups and cations in the order $\text{Na} > \text{Ca} > \text{Mg} > \text{Fe}^{2+} > \text{Fe}^{3+}$ (Table 3.4). Hydroxyl groups are, therefore, unlikely to form complexes with Fe^{2+} and Fe^{3+} , which should result in little to no impact on the ferrous-ferric ratio in

magmas. Waters & Lange (2013) demonstrated the potential for dissolved melt H₂O to affect the $K_D^{\text{Fe-Mg}}$ between orthopyroxene and liquid, by reducing the activity of MgO in melts with low MgO contents (e.g., rhyolites). This effect of dissolved H₂O on the activity of MgO in the melt may result in variability in the Mg-rich spinel end member in titanomagnetite, MgAl₂O₄. Thus, degassing of H₂O from a melt will not affect the activities of Fe²⁺ and Fe³⁺ but will affect the activity of MgO, and may cause the observed ranges of composition in titanomagnetite and ilmenite. These changes then translate to small ranges in ΔNNO and temperature that convert into a small variation in wt% FeO. The small observed difference between pre-and post-eruptive ΔNNO values supports the conclusion that degassing of water had a negligible effect on the oxidation state of magmas (Fig. 3.1).

Table 3.4 *Free energy of hydration reactions*

Reaction	$\Delta G(298 \text{ K})$ kJ/mol
Na ₂ O + H ₂ O = 2NaOH	-143.3
CaO + H ₂ O = Ca(OH) ₂	-57.8
MgO + H ₂ O = Mg(OH) ₂	-27.6
FeO + H ₂ O = Fe ²⁺ (OH) ₂	-3.4
1/3 Fe ₂ O ₃ + H ₂ O = 2/3 Fe(OH) ₃	14.7
Na (gas) + Cl (gas) = NaCl (solid)	-566.5
1/2Ca (gas) + Cl (gas) = 1/2CaCl ₂ (solid)	-534.8
1/2Mg (gas) + Cl (gas) = 1/2MgCl ₂ (solid)	-457.5
1/2Fe (gas) + Cl (gas) = 1/2FeCl ₂ (solid)	-441.8
1/3Fe (gas) + Cl (gas) = 1/3FeCl ₃ (solid)	-340.2

From JANAF tables (Chase, 1998)

The Cl contents in apatites and the maximum Cl content that can be dissolved in the melt estimated from Webster and De'vivo (2002) demonstrate that chlorine was present during crystallization of apatite and phenocryst growth. The solubility model of Webster and De' Vivo (2002) incorporates the temperature and whole rock composition to estimate the maximum amount of Cl that can be dissolved in each rhyolite melt. The

solubility model estimates that pre-degassed Cl contents for all six samples may range from ~3600 to 6000 ppm, and post-degassed Cl contents measured in the groundmass glasses with electron microprobe range from ~580-900 ppm. A loss of >1000 ppm Cl in each sample produces no detectable change in the pre- and post-eruptive Fe²⁺ concentrations. One possible explanation to account for an absence of an effect of Cl on the pre- and post-eruptive concentration of ferrous iron, is that Cl degassed prior to the crystallization of oxides, therefore any scavenging of Fe²⁺ from the melt into the fluid phase (e.g., Bell and Simon, 2011) would not be recorded. A second explanation can be found in the chlorine solubility model of Webster and De' Vivo (2002) and the Gibbs free energy of exchange between Cl and melt components (Table 3.4), which both demonstrate that Cl will preferentially bond with K, Na, Ca, Mg, relative to Fe²⁺ and Fe³⁺. Based on the Gibbs free energy of exchange in Table 3.4, Cl is unlikely to bond with ferric or ferrous iron in liquids with elevated concentrations Na and K (e.g., rhyolites).

3.7 CONCLUSIONS

Degassing fluids consisting of mostly H₂O from a rhyolite melt has no observable effect on the pre-eruptive and post-eruptive ferric-ferrous ratio. It is likely that degassing of dissolved H₂O has no effect on the activities of Fe²⁺ and Fe³⁺ in the melt, which is consistent with the studies of Sisson and Grove (1993), Moore et al. (1995) and Botcharnikov et al. (2005). It would be expected that loss of a fluid rich Cl, F, and/or S from a rhyolite melt would cause a significant change in the pre- and post-eruptive ferrous iron contents.

3.8 REFERENCES

- Bacon, C.R. & Hirschmann, M. M. (1988). Mg/Mn partitioning as a test for equilibrium between coexisting Fe-Ti oxides. *American Mineralogist* 73, 57-61
- Behrens, H. & Gaillard, Fabrice. (2006). Geochemical Aspects of Melts: Volatiles and Redox Behavior. *Elements* 2, 275-280
- Bell, A.S. and Simon, A., (2011). Experimental evidence for the alteration of the $\text{Fe}^{3+}/\Sigma\text{Fe}$ of silicate melt caused by the degassing of chlorine-bearing aqueous volatiles. *Geology* 39, 499-502
- Botcharnikov, R.E., Koepke, J., Holtz, F., McCammon, C., and Wilke, M., (2005) The effect of water activity on the oxidation and structural state of Fe in a ferro-basaltic melt. *Geochimica Cosmochimica Acta* 69, 5071–5085
- Burgisser, A. & Scaillet, B. (2007). Redox evolution of a degassing magma rising to the surface. *Nature* 445, 194-197.
- Candela (1986) The evolution of aqueous vapor from silicate melts: effect on oxygen fugacity. *Geochim Cosmochim Acta* 50, 1205–1211
- Carmichael, I.S.E. (1967). The Iron-Titanium Oxides of Salic Volcanic Rocks and their Associated Ferromagnesian silicates. *Contributions to Mineralogy and Petrology* 14, 36-64.
- Carmichael, I.S.E. (1991). The redox states of basic and silicic magmas: a reflection of their source regions? *Contributions to Mineralogy and Petrology* 106, 129-141.
- Chase (1998) NIST-JANAF thermochemical tables, fourth edition. *Journal of Physical Chemistry Reference Data*, Monograph Springer, Heidelberg, p 9
- Clemente, B. Scaillet, B. and Pichavant, M. (2004). The solubility of sulphur in hydrous rhyolitic melts. *Journal of Petrology* 45, 2171-2196.
- Crabtree, S.M. & Lange, R.A. (2012) An evaluation of the effect of degassing on the oxidation state of hydrous andesite and dacite magmas: a comparison of pre- and post-eruptive Fe^{2+} concentrations. *Contributions to Mineralogy and Petrology* 163, 209-224
- Dolejš, D., and Wagner, T., 2007, Thermodynamic modeling of non-ideal mineral fluid equilibria in the system Si-Al-Fe-Mg-Ca-Na-K-H-O-Cl at elevated temperatures

- and pressures: Implications for hydrothermal mass transfer in granitic rocks: *Geochimica et Cosmochimica Acta*, v. 72, p. 526–553
- Evans, B.W., Scaillet, B., and Kuehner, S.M. (2006) Experimental determination of coexisting iron-titanium oxides in the systems FeTiAlO, FeTiAlMgO, and FeTiAlMgMnO at 800 and 900 °C, 1–4 kbar, and relatively high oxygen fugacity. *Contributions to Mineralogy and Petrology*, 152 149–167
- Gaillard, F., Scaillet, B., Pichavant, M., and Beny, J.M. (2001). The effect of water and fO₂ on the ferric-ferrous ratio of silicic melts. *Cemical Geology* 174, 255-273.
- Gaillard, F., Pichavant, M., and Scaillet, B. (2003). Experimental determination of activities of FeO and Fe₂O₃ components in hydrous silicic melts under oxidizing conditions. *Geochimica et Cosmochimica Acta* 67, 4389-4409.
- Ghiorso, M. S. & Evans, B.W. (2008). Thermodynamics of rhombohedral oxide solid solutions and a revision of the Fe-Ti two-oxide geothermometer and oxygen barometer. *American Journal of Science* 308, 957-1039.
- Henderson, C. (2011) *Protocols and Pitfalls of Electron Microprobe Analysis of Apatite*. University of Michigan M.S. Thesis.
- Jugo, P.J. (2009) Sulfur content at sulfide saturation in oxidized magmas: *Geology* 37, 415–418
- Kelley KA, Cottrell E (2009) Water and the oxidation state of subduction zone magmas. *Science* 325, 605–607
- Koděr, P., Rankin, A.H., and Lexa, J. (1998) Evolution of fluids responsible for iron skarn mineralisation: An example from the Vyhne-Klokoc deposit, Western Carpathians, Slovakia: *Mineralogy and Petrology*, v. 64, p. 119–147
- Kress, V. & Carmichael, I.S.E. (1991). The compressibility of silicate liquids containing Fe₂O₃ and the effect of composition, temperature, oxygen fugacity and pressure on their redox states. *Contributions to Mineralogy and Petrology* 108, 82-92.
- Lange, R. A., Frey, H. M. & Hector, J. (2009). A thermodynamic model for the plagioclase-liquid hygrometer/thermometer. *American Mineralogist* 94, 494-506.
- Macleod (1969)
- Mathez, E.A. (1984). Influence of degassing on oxidation states of basaltic magmas. *Nature* 30, 371-375.

- Moore, G., Richter, K., & Carmichael, I.S.E. (1995). The effect of dissolved water on the oxidation state of iron in natural silicate liquids. *Contributions to Mineralogy and Petrology* 120, 170-179.
- Moretti and Papale (2004)
- O'Neill H. S. C. & Pownceby, M. I. (1993). Thermodynamic data from redox reactions at high temperatures. I. An experimental and theoretical assessment of the electrochemical method using stabilized zirconia electrolytes, with revised values for the Fe-“FeO”, Co-CoO, Ni-NiO and Cu-Cu₂O buffers and new data for the W-WO₂ buffer. *Contributions to Mineralogy and Petrology* 114, 296-314
- Pyle, J.M., Spear, F.M. & Wark D.A. (2002) Electron Microprobe Analysis of REE in Apatite, Monazite and Xenotime: Protocols and Pitfalls. *Rev. Mineral. Geochem.* 48, 337-362.
- Sack, R.O., Carmichael, I.S.E., Rivers, M., and Ghiorso, M.S. (1980). Ferric-Ferrous Equilibria in Natural Silicate Liquids at 1 Bar. *Contributions to Mineralogy and Petrology* 75, 369-376
- Sisson TW, Grove TL (1993) Experimental investigations of the role of H₂O in calc-alkaline differentiation and subduction zone magmatism. *Contributions to Mineralogy and Petrology* 113, 143–166
- Stormer, J.C. Jr., Pierson, M.L. & Tacker, R.C. (1993) Variation of F and Cl X-ray intensity due to anisotropic diffusion in apatite during electron microprobe analysis. *American Mineralogist*, 78, 641-648
- Waters, L.E., Andrews, B.J., & Lange R.A. (2012) Water-saturated phase equilibrium experiments on rhyolite and dacite obsidians: the effect of variable melt water concentration on the composition of phenocrysts. Assessing the role of crystallization and degassing on the evolution of magmatic-hydrothermal systems: cosponsored by MSA II: American geophysical union fall meeting
- Waters, L.E. and Lange, R.A. (2013) Crystal-poor, multiply saturated rhyolites (obsidians) from the Cascade and Mexican arcs: evidence of degassing induced crystallization of phenocrysts. *Contributions to Mineralogy and Petrology* 166, 731-754

- Webster, J.D. and DeVivo, B. (2002) Experimental and modeled solubilities of chlorine in aluminosilicate melts, consequences of magma evolution, and implications for exsolution of hydrous chloride melt at Mt. Somma-Vesuvius. *American Mineralogist* 87, 1046-1061
- Webster, J.D., Tappen, C.M. and Mandeville, C.W. (2009) Partitioning behavior of chlorine and fluorine in the system apatite–melt–fluid. II: Felsic silicate systems at 200 MPa. *Geochimica et Cosmochimica Acta* 73, 559-581
- Whitney J. A., Hemley J. J. and Simon F. O. (1985) The concentration of iron in chloride solutions equilibrated with synthetic granitic compositions: the sulfur-free system. *Economic Geology* 80, 444-460
- Wilke, M., Behrens H., Burkhard, D.J.M., and Rossano, S. (2002) The oxidation state of iron in silicic melt at 500 MPa water pressure. *Chemical Geology* 189, 55-67
- Wilson, A.D. (1960) The micro-determination of ferrous iron in silicate minerals by a volumetric and a colorimetric method. *Analyst* 85, 823–827

CHAPTER IV

DEGASSING INDUCED CRYSTALLIZATION OF PLAGIOCLASE IN RHYOLITE AND RHYODACITE OBSIDIANS: PHASE EQUILIBRIUM AND DECOMPRESSION EXPERIMENTS

4.1 ABSTRACT

A series of phase-equilibrium experiments under pure H₂O fluid-saturated conditions were performed on three crystal-poor (<3%) obsidians (one dacite, 67 wt% SiO₂; two rhyolites, 73 and 75 wt% SiO₂) in a cold-seal pressure vessel between 30-300 MPa and 750-950°C. The results show that the remarkably wide ranges of plagioclase compositions (≤38 mol% An) observed in the natural samples are all plausible phenocrysts. A single xenocryst, a plagioclase core (An₆₀₋₆₃) that comprises < 0.1% of the sample, was identified in one of the rhyolite obsidians. In addition, a series of isothermal (850°C) decompression experiments under pure H₂O fluid-saturated conditions were performed on one of the samples (73 wt% SiO₂). Decompressions were conducted at two continuous rates (2.9 and 0.8 MPa/hr), beginning above the liquidus at P_{H₂O} = 150 MPa and quenched at two pressures (P_{H₂O} = 89 and 58 MPa) below the plagioclase-in curve. For the experiments decompressed at 2.9 MPa/hr, the run products were 100% glass, whereas for those decompressed at 0.8 MPa/hr, the run products contained a mineral assemblage similar to that found in the phase-equilibrium experiments. A comparison between the decompression and phase-equilibrium experiments show that plagioclase began to crystallize immediately after the plagioclase-in curve was crossed during decompression at 0.8 MPa/hr and that a continuum of changing *equilibrium* plagioclase

compositions crystallized from the melt as degassing progressed. The plagioclase crystals in these decompression experiments often display textures (skeletal, large interior melt hollows, swallowtails) consistent with diffusion-limited crystal growth, which is expected to occur owing to the large undercoolings that develop during degassing-induced crystallization, especially as melt viscosity increases with the loss of dissolved water. The suppression of plagioclase nucleation and crystal growth in rhyolites that undergo rapid degassing explains the overall low abundance of plagioclase phenocrysts and scarcity of microlites in the three natural obsidian samples, and it is used to develop a plagioclase speedometer for rhyolites from the decompression experiments in this study as well as those from the literature.

4.2 INTRODUCTION

Plagioclase crystals in intermediate lavas (e.g., andesites and dacites) often span a wide range in composition (≤ 40 mol% An) and often display complex textures and zoning patterns (Tepley *et al.*, 1999, 2000; Zellmer *et al.*, 2003; Humphreys *et al.*, 2006; Ruprecht & Wörner, 2007; Crabtree & Lange, 2011; Frey & Lange, 2011). The mechanism most commonly invoked to explain these complex plagioclase populations found in intermediate lavas is mixing/mingling between relatively mafic (e.g., basalt or basaltic andesite) and relatively felsic end members (e.g., dacite or rhyolite) magmas (Izbeckov *et al.*, 2002; Couch *et al.*, 2003a; Gerbe & Thouret, 2004; Humphreys *et al.*, 2006; Ruprecht & Wörner, 2007; Andrews *et al.*, 2008; Reubi & Blundy, 2008, 2009; Kent *et al.*, 2010). A second independent process that may introduce complexity to the observed plagioclase compositions and textures in intermediate magmas is degassing-

induced crystallization during ascent of fluid-saturated magma (e.g., Crabtree & Lange, 2011; Frey & Lange, 2011; Waters & Lange, 2013). Because the concentration of dissolved water in the melt strongly affects the composition of plagioclase (e.g., Sisson and Grove, 1993; Housh & Luhr, 1991; Putirka, 2005; Lange *et al.*, 2009), degassing-induced crystallization can produce a wide range of plagioclase compositions (e.g., Couch *et al.*, 2003b; Martel & Schmidt, 2003; Brugger & Hammer, 2010). Degassing-induced crystallization can also produce complex, diffusion-limited growth textures (e.g., skeletal, melt hollows, swallow tail, vermiform) owing to the rapid development of large undercoolings during fluid-saturated decompression (e.g., Blundy & Cashman, 2005; Hammer & Rutherford, 2002; Shea & Hammer, 2013).

Importantly, populations of plagioclase crystals that span a wide range of composition and display complex zoning patterns are not exclusively found in intermediate magmas but are also observed in rhyolites. For example, in a detailed petrologic study of crystal-poor (<6 %) obsidian samples (73-75 wt% SiO₂), Waters & Lange (2013) document that plagioclase crystals in these obsidians often span a remarkably wide range of composition (≤ 30 mol% An) and display complex zoning patterns (normal, reverse, and unzoned). Mixing of magmas of distinctly different bulk compositions (felsic and mafic) can be ruled out for the origin of these glassy, crystal-poor rhyolites, as these lavas are end-member compositions, however, it is possible that plagioclase xenocrysts were incorporated into them. An outstanding question, therefore, is whether the wide compositional range of plagioclase phenocrysts observed in the obsidian samples can be attributed to degassing-induced crystallization, or if the incorporation of plagioclase xenocrysts is required to explain the full range observed.

To address this question, a series of fluid-saturated phase-equilibrium and decompression experiments were conducted on three obsidian samples (67, 73 and 75 wt% SiO₂) that contain < 3 % phenocrysts + microphenocrysts and are largely free of microlites. Fluid-saturated phase-equilibrium experiments were first performed to determine equilibrium plagioclase compositions in each sample as a function of temperature and P_{H₂O}. Next, a series of fluid-saturated isothermal decompression experiments, initiated above the liquidus, were then conducted to test whether the wide range of plagioclase compositions and complex textures and zoning patterns observed in the natural obsidian samples could be reproduced.

Sample Background

The three obsidian samples used in this study range from dacite (67 wt% SiO₂, TEQ-34) to rhyolite (73 and 75wt% SiO₂; MLV-36 and -44, respectively). The dacite was erupted from a monogenetic vent in the western Mexican arc and was the focus of a detailed petrologic study in Crabtree & Lange (2011). The two rhyolites were erupted from monogenetic vents at the Medicine Lake volcanic field in the Cascades. The petrologic details of MLV-36 are presented in Waters & Lange (2013), whereas those for MLV-44 are given in this study. Each sample contains four to six mineral phases (Table 4.1) with plagioclase, titanomagnetite and ilmenite common to all. Additional phases include orthopyroxene, clinopyroxene, biotite and apatite. Phenocryst + microphenocryst abundances are < 3%, and microlites are sparse in all three obsidian samples (Table 4.1; Fig. 4.1).

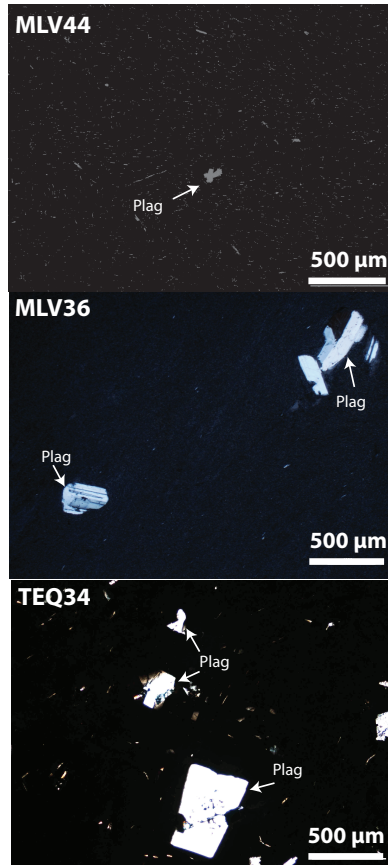


Figure 4.1: Photomicrographs of the three obsidians illustrate the phenocryst-poor glassy nature of the obsidians with little to no microlite crystallization. Images were collected in cross polarized light. Plagioclase crystals are labeled as “plag.”

Table 4.1: Bulk Compositions

Sample	MLV44	MLV36	TEQ34
SiO ₂	75.45	73.8	67.1
TiO ₂	0.22	0.27	0.6
Al ₂ O ₃	13.22	13.2	15.7
FeO ^T	1.42	2.08	3.38
MnO	0.04	0.04	0.11
MgO	0.21	0.27	0.65
CaO	0.81	1.23	1.66
Na ₂ O	3.91	3.99	5.53
K ₂ O	4.73	4.18	4.25
P ₂ O ₅	<0.01	0.06	0.16
LOI	0.43	0.31	0.30
Total	100.4	99.4	99.5
% plag	<0.1	1.9	1.8
% opx	<0.1	0.6	0.1
% cpx	<0.1	<0.1	0.1
% bte	-	-	<0.1
% ox	<0.1	0.3	0.2
% gdms	99.7	97.1	97.7

LOI, loss on ignition; plag, plagioclase; opx, orthopyroxene; cpx, clinopyroxene; bte, biotite; ox, oxides; gdms, groundmass.

Microprobe analyses of titanomagnetite, ilmenite and plagioclase in MLV-44 were performed at the University of Michigan with a Cameca SX electron microprobe, following the same procedures outlined in Waters & Lange (2013). Analyses of Fe-Ti oxide phases in MLV-44 are provided in Table C1 (Appendix C). A plot of $\log(X_{\text{Mg}}/X_{\text{Mn}})$ (Appendix C Fig. C1A) shows that all possible pairs of analyzed ilmenite and titanomagnetite crystals do not deviate strongly from the equilibrium test proposed by Bacon & Hirschman (1988). The two Fe-Ti oxide thermometer and oxybarometer of Ghiorso & Evans (2008) applied to all pairs of ilmenite and titanomagnetite in MLV-44 lead to a narrow range of temperature ($932 \pm 15^\circ\text{C}$) and ΔNNO (0.7 ± 0.1) values (Fig. C1B). Analyses of plagioclase phenocrysts + microphenocrysts in MLV-44 are reported in Table C2 (Appendix C); they span a narrow range of composition ($\text{An}_{29}\text{-An}_{20}$), which is illustrated in a histogram of all analyses in Fig 4.2.

Also shown in Fig. 4.2 are histograms of analyzed plagioclase phenocryst + microphenocryst compositions in MLV-36 and TEQ-34, as well the temperature and ΔNNO values obtained from two Fe-Ti oxides in those samples, previously reported in Waters & Lange (2013) and Crabtree & Lange (2011), respectively. The information on the pre-eruptive temperatures of these three samples, along with the range of plagioclase compositions, will be used later in this paper in a comparison to the phase-equilibrium experiments described below.

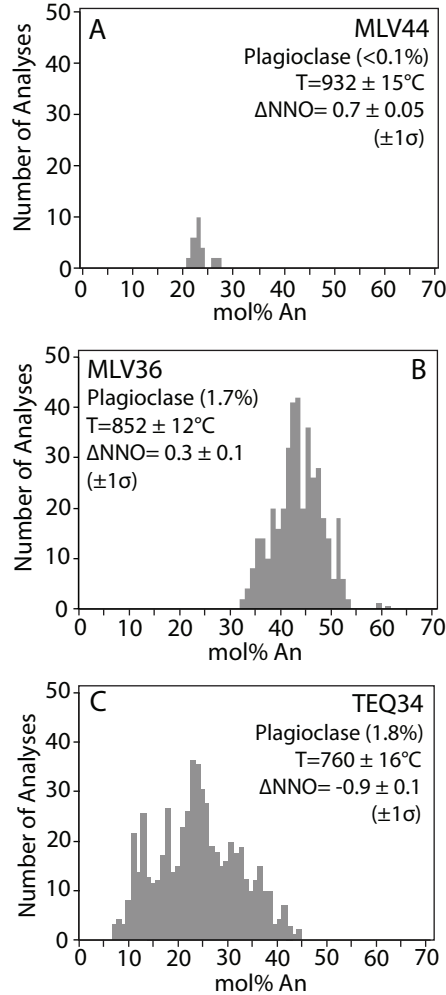


Figure 4.2: The range of plagioclase observed in the natural samples as a function of mol% An v. number of analyses from microprobe analyses for MLV44 (a), MLV36 (b), and TEQ34 (c). The analyses for plagioclase in MLV44 are sparse due to very low plagioclase crystallization and are reported in the Appendix C Table C1. Plagioclase analyses for MLV36 and TEQ34 are taken from Waters & Lange (2013) and Crabtree & Lange (2011). The temperature and $f\text{O}_2$ (as a function of the NNO buffer) results of the oxide geo-thermometer of Ghiorso and Evans (2008) are shown for all possible pairings of ilmenite and titanomagnetite for MLV44 (a), MLV36 (b), and TEQ34 (c). Ilmenite and titanomagnetite analyses for MLV44 are reported in Appendix C Table C2.

4.3 EXPERIMENTAL METHODS

Phase-Equilibrium Experiments

Starting Material Preparation

Pieces of black obsidian from each sample were crushed in a porcelain shatter box to a fine powder. Aliquots of ~ 10 g of each powder were then placed in a platinum

crucible in air, heated to 1450°C and held for one hour, and then quenched to a glass, which were determined to be aphyric and anhydrous. These aphyric glasses were crushed a second time and used as starting material for the phase-equilibrium experiments.

Experimental Conditions and Apparatuses

All experiments were conducted in cold-seal pressure vessels with water as the pressurizing medium at the National Museum of Natural History in Washington, D.C., at pressures and temperatures ranging from 30-300 MPa and 750-950°C (Table 4.2). For each experiment, 10-30 mg of starting material was placed inside 3 mm OD gold tubing, to which ~10% of the sample weight in DI water was added to ensure that all runs would be saturated with 100% H₂O fluid. The gold capsules were sealed using a PUK-3 welding system.

During the quenching procedure, the temperature in the hot spot of the pressure vessel cooled to below 500°C (~the glass transition temperature) in less than 30 seconds by blowing compressed air on the charge (the temperature change with time was recorded with a thermocouple placed in a retrofitted pressure head); the vessels were then plunged into a cold-water bath. Charges that contained excess water after quenching were considered successful. The system of waspaloy (nickel alloy) pressure vessels and nickel filler rods used in the phase equilibrium experiments has an intrinsic oxygen fugacity of $\Delta\text{NNO} +1 \pm 0.5$ (Geschwind & Rutherford, 1992). Venesky & Rutherford (1999) show that the $f\text{O}_2$ imposed by the waspaloy pressure vessels and nickel filler rods may vary significantly and is dependent on the age and degree of oxidation of the nickel filler rod. Based on the observation that the Ni-filler rod showed more signs of oxidation under these conditions, It is likely that the intrinsic $f\text{O}_2$ generated by the nickel filler rod and

Table 4.2: Phase equilibrium experiments: Run conditions and products

	Temperature (°C)	Pressure (MPa)	Duration (h)	Run Products
MLV44	750	300	120	g, bte, mt
	750	250	120	g, bte, mt
	750	250	48	g, bte, mt
	750	200	96	g, pl, bte, mt
	750	200	48	g, pl, bte, mt
	750	100	72	g, pl, opx, cpx, mt
	800	250	48	g, bte, mt
	800	150	48	g, bte, mt
	800	100	48	g, pl, mt
	850	200	48	g
	850	150	48	g
	850	100	48	g, mt
	900	150	48	g
	900	100	48	g
	950	50	48	g
	950	30	48	g, pl, opx, mt
MLV36	750	300	120	g, bte, mt
	750	250	120	g, bte, mt
	750	250	48	g, bte, mt
	750	220	48	g, pl, bte, mt
	750	200	120	g, pl, bte, mt
	750	200	48	g, pl, bte, mt
	750	100	72	g, pl, opx, cpx, mt
	800	300	48	g, bte, mt
	800	160	48	g bte, mt
	800	150	48	g, pl, opx, mt
	800	100	48	g, pl, opx, cpx, mt
	850	250	48	g
	850	200	48	g
	850	150	48	g
	850	125	48	g, opx, mt
	850	100	48	g, pl, opx, mt
	850	80	48	g, pl, opx, mt, il
	850	60	48	g, pl, opx, cpx, mt, il
	875	200	48	g
	900	100	48	g
900	75	48	g, mt	
900	50	48	g, pl, opx, mt	
950	50	48	g	
TEQ34	750	300	48	g, pl, bte, mt
	750	250	120	g, pl, bte, cpx, mt
	750	250	48	g, pl, bte, cpx, mt
	750	200	144	g, pl, bte, cpx, mt
	750	200	120	g, pl, bte, cpx, mt
	750	200	48	g, pl, bte, cpx, mt
	800	300	48	g, bte, mt
	800	250	48	g, pl, bte, cpx, mt
	800	200	48	g, pl, bte, cpx, mt
	800	150	48	g, pl, bte, cpx, mt
	800	110	48	g, pl, bte, cpx, mt
	850	250	48	g, bte, mt
	850	200	48	g, bte, mt
	850	150	48	g, pl, bte, mt
	850	100	48	g, pl, bte, mt
	875	200	48	g, bte, mt
	900	150	48	g, bte, mt
	900	100	48	g, mt
	900	50	48	g, cpx, mt
	950	50	48	g, mt

Abbreviations: g, glass; pl, plag; bte, biotite; opx, orthopyroxene; cpx, clinopyroxene; mt, magnetite; il, ilmenite.

Waspaloy pressure vessel system increases with P_{H_2O} in these experiments, possibly because the water used as the pressure medium is initially in equilibrium with air. Therefore, the only constraint on fO_2 in these experiments is that it is greater than that of the Ni-NiO buffer. Because fO_2 is only broadly constrained in each experiment, only plagioclase-liquid equilibrium results are used in this study. Fe-bearing mineral stability curves are recorded but not used.

Equilibrium Tests

To evaluate whether plagioclase-liquid equilibrium was attained, experiments conducted at the lowest temperature and highest melt viscosity for each sample were replicated three times, but for different run durations of 48, 96, and 120 hours. No significant change was observed in either the liquid (wt% SiO₂) or plagioclase (mol%An) compositions with time, as illustrated in Fig. 4.3. A similar result was obtained in Couch *et al.* (2003b), where it was argued that experiments conducted on an H₂O-saturated rhyolite liquid at 860°C reached plagioclase-liquid equilibrium after ~48 hours over a range of pressures (125, 75 and 50 MPa).

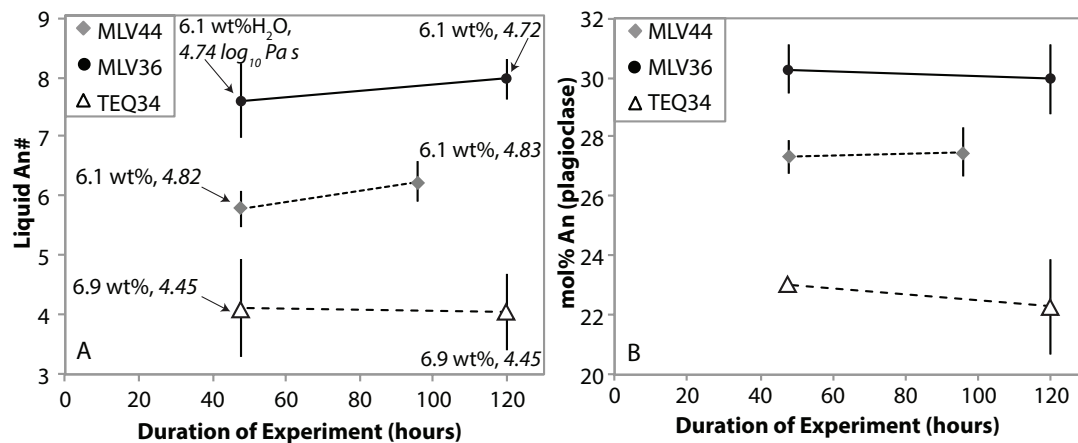


Figure 4.3: Plot of experiment duration (hours) v. the liquid composition as a function of the anorthite number of the liquid (liquid An#). No significant change in liquid composition is observed. (b) Plot of experiment duration (hours) v. the composition of the plagioclase grown in that experiment (as mol% An). No significant change in composition is observed.

Decompression Experiments

In order to accurately reproduce the scenario of an ascending, fluid-saturated liquid, decompression experiments were started above the liquidus (crystal free, H₂O-saturated conditions) and decompressed to pressures below the plagioclase-in curve. Decompression experiments were attempted on all three samples, but were only successful for MLV-36. For MLV-44, the plagioclase-in curve at the pre-eruptive temperature ($932 \pm 15^\circ\text{C}$) is located at a relatively low pressure (<40 MPa), which led to capsule rupture owing to the large molar volume of H₂O fluid at this T-P condition. For TEQ-34, the plagioclase-in curve at the pre-eruptive temperature ($760 \pm 16^\circ\text{C}$) was located at a pressure higher than could be accessed with the cold-seal vessel (300 MPa). For MLV-36, the plagioclase-in curve at the pre-eruptive temperature ($852 \pm 12^\circ\text{C}$) was located at a pressure readily accessed by the cold-seal pressure apparatus (150 MPa).

Starting Material

Starting material for each MLV-36 decompression experiment was H₂O-saturated glass. Approximately 70 mg of anhydrous glass was placed in a 3mm OD gold capsule with ~ 7 mg of H₂O. The capsule was held at 850°C and 150 MPa (super-liquidus conditions) for 48 hours and then quenched. Aliquots of these quenched, hydrous glasses were sealed in 3mm OD gold tubing with 1-2 mg deionized water to ensure H₂O fluid saturation.

Experimental Conditions

Isothermal decompression experiments were conducted in the same cold-seal pressure vessels used for the phase-equilibrium experiments. Samples were taken up to an initial pressure (150 MPa) and temperature (850°C), which is above the liquidus, and held

for over two hours. Samples were then decompressed isothermally at two different rates of 2.9 and 0.8 MPa/hr and were quenched at two different final pressures of 89 and 58 MPa. The decompression rate was controlled by slowly cooling an extra empty pressure vessel at a specific rate to produce a nearly constant rate of pressure change.

Decompression paths were recorded by a computer and reported in this paper for each experiment (Appendix C Fig. C2). The pressure monitoring system also picked up diurnal fluctuations in pressure (≤ 20 bars superimposed on the decompression path), likely due to both the building heating system and direct sunlight on the pressure line. Decompression rates, starting pressures, and quench pressures are reported in Table 4.3.

Table 4.3: *MLV36 Decompression Experiments: Run Conditions and Products*

Temperature (°C)	Initial Pressure (MPa)	Final Pressure (MPa)	Duration (h)	Rate (MPa/hr)	Run Products
850	150	89	20.5	2.9	g
850	150	58	30.3	2.9	g
850	150	89	76	0.8	g, plg, opx, mt, il
850	150	58	120	0.8	g, plg, opx, cpx, mt, il

Abbreviations: g, glass; pl, plag; opx, orthopyroxene; cpx, clinopyroxene; mt, magnetite; il, ilmenite

Analyses of Phases in Run Products

Phase-Equilibrium Experiments

The charges quenched from the phase-equilibrium experiments were peeled open and chips of the run products were mounted in epoxy and polished for microprobe analyses. Glasses and minerals in the run products were analyzed with the Cameca SX-100 electron microprobe at the University of Michigan and with the JEOL 8900 superprobe at the National Museum of Natural History in Washington, DC. An accelerating voltage of 15 kV with a focused beam was used in all analyses of run products. A beam current of 4 nA was used for analyses of plagioclase and 15 nA for

orthopyroxene and clinopyroxene. For matrix glasses, a defocused 5 μ m beam was used with a beam current of 5 nA. Count times for each element ranged between 20-30s. Na in glasses was measured on-peak for 30 seconds with six sub-counting intervals of five seconds to assess and correct for Na loss.

Melt H₂O Contents

Melt H₂O contents were calculated using the glass composition of each experiment and the H₂O solubility model of Liu *et al.* (2005). Ten experimental glasses with H₂O contents ranging from 1.5-7.5 wt% (using the model of Liu *et al.*, 2005) were analyzed using Fourier transform infrared (FTIR) spectroscopy to ensure that the H₂O solubility model was recording accurate values. The FTIR results are shown in Table C3 and are shown to be consistent with the H₂O results from Liu *et al.* (2005) in Fig. C3. All analyses of experimental glasses and modeled H₂O concentrations are shown in Table C4.

Decompression Experiments

Microprobe analyses of plagioclase in the decompression run products were made using the same procedures as those employed for the phase-equilibrium experiments. However, the shape of the plagioclase crystals (ranging from long and tabular with melt hollows to irregular) in the run products of the decompression experiments generally limited microprobe analyses to a few select points. To ensure that the full range of plagioclase compositions was accurately documented, several high-definition Energy Dispersive X-Ray Spectrometry (EDX) element maps (Si, Ti, Al, Fe, Mg, Ca, Na, K) were measured on all run products using the FEI Nova NanoSEM 600 (scanning electron microscope) at the National Museum of Natural History, Mineral Sciences Department. The element maps and BSE image of the mapped area were processed with MatLab to

create maps of anorthite content in the plagioclase crystals. The groundmass was filtered out using counts of Si, K and Fe, epoxy was filtered out with the grey scale map image, and anorthite content maps were made using the Ca, Na, K, Si and Al maps. To test and validate this mapping technique, a mapping standard was created by fusing chips of labradorite and oligoclase from the Smithsonian collection in a hydrated rhyolite glass. The labradorite (53 ± 4 mol% An) and oligoclase (22 ± 2 mol% An) were measured with the microprobe and shown to each span a small range in composition ($\pm 2\sigma$). The code used to process the element maps of the decompression run products was tested on element maps of the labradorite-oligoclase-rhyolite glass standard in an attempt to recover the compositions of oligoclase and labradorite. The code recovers both the labradorite and oligoclase compositions (53 ± 4 mol% An and 24 ± 4 mol% An and, respectively) in good agreement with the electron microprobe analyses.

4.4 RESULTS

Phase equilibrium Experiments

Run products of the phase equilibrium experiments are summarized in Table 4.2 and illustrated in Figs. 4.4-4.6. Compositions of matrix glasses and measurable plagioclase crystals are presented in Tables 4.4 and 4.5, respectively. The calculated H₂O concentrations for each of the samples using Liu *et al.* (2005) are listed in Table 4.4. All analyses of matrix glasses, plagioclase, orthopyroxene and clinopyroxene crystals are presented in Appendix C (Tables C4-C7).

Table 4.4: Glass Compositions

	T (°C)	Pressure (MPa)	Duration (h)	n	SiO ₂	TiO ₂	Al ₂ O ₃	FeO	MnO	MgO	CaO	Na ₂ O	K ₂ O	P ₂ O ₅	Total	liquidAn# ¹	wt% H ₂ O ²	Viscosity ³ (log ₁₀ Pa s)	XAn	XAb	% xtal ⁴
MLV44	750	200	96	5	76.9	0.12	13.8	1.14	0.04	0.12	0.92	3.54	4.88	0.02	92.3	6.24	6.05	4.83	27.5	65.9	2.1
				$\pm 1\sigma$	0.2	0.06	0.2	0.18	0.07	0.06	0.03	0.37	0.21	0.05	0.4	0.34	0.04	0.07	0.8	1	
	750	200	48	11	75.9	0.14	13.5	0.80	0.02	0.08	0.88	3.83	4.82	0.02	93.6	5.79	6.09	4.82	27.3	66.1	2
				$\pm 1\sigma$	0.3	0.04	0.1	0.09	0.03	0.02	0.03	0.27	0.12	0.06	0.5	0.31	0.03	0.05	0.6	1	
	750	100	72	11	77.0	0.11	13.0	0.96	0.06	0.12	0.64	3.12	5.01	0.03	95.0	4.53	4.22	5.58	19.9	67.2	6.6
				$\pm 1\sigma$	1.2	0.04	0.2	0.20	0.13	0.07	0.12	0.32	0.17	0.09	1.0	0.84	0.02	0.1	0.6	0.5	
800	100	72	8	75.7	0.17	13.1	1.14	0.03	0.15	0.85	4.05	4.80	0.00	95.2	5.4	4.11	5.03	24.5	65	1.5	
			$\pm 1\sigma$	0.2	0.04	0.1	0.11	0.05	0.05	0.02	0.24	0.15	0.06	0.3	0.24	0.02	0.06	0.8	0.8		
950	30	48	8	75.0	0.25	12.9	1.36	0.04	0.19	0.82	3.12	6.24	0.03	97.8	5.88	1.87	5.2	22.2	61.4	16.9	
			$\pm 1\sigma$	0.9	0.06	0.3	0.11	0.06	0.04	0.02	0.46	0.23	0.03	0.5	0.24	0.01	0.13	0.4	1.3		
MLV36	750	220	48	19	76.9	0.14	14.1	0.80	0.03	0.12	1.18	3.02	3.76	0.01	92.9	8.54	6.2	4.98	42.4	54.2	2.4
					0.4	0.03	0.1	0.07	0.02	0.03	0.06	0.21	0.22	0.04	0.7	0.53	0.04	0.06	1.4	1.5	
	750	200	120	6	74.4	0.18	13.9	1.32	0.03	0.21	1.25	4.09	4.60	0.01	93.5	7.97	6.08	4.72	29.9	65.4	2.7
					0.9	0.09	0.1	0.35	0.04	0.11	0.08	0.18	0.16	0.08	0.7	0.35	0.03	0.06	1.2	1.1	
	750	200	48	8	74.5	0.18	13.9	1.31	0.05	0.15	1.18	4.12	4.51	0.01	93.5	7.6	6.07	4.74	30.3	67.1	2.7
					0.8	0.11	0.1	0.38	0.04	0.08	0.04	0.33	0.19	0.07	0.5	0.63	0.02	0.06	0.8	1.5	
	750	100	72	9	75.9	0.10	13.4	1.12	0.05	0.14	0.75	3.16	5.21	0.10	95.0	5.43	4.21	5.56	19	68.3	6.8
					1.0	0.05	0.2	0.35	0.05	0.11	0.07	0.16	0.17	0.11	0.9	0.56	0.01	0.08	0.9	0.8	
	800	150	48	7	73.9	0.25	14.0	1.50	0.03	0.30	1.22	4.16	4.52	0.03	96.3	7.86	5.08	4.59	39.9	55	0.6
					0.5	0.04	0.2	0.14	0.02	0.02	0.07	0.27	0.14	0.02	0.3	0.3	0.03	0.07	3	3.1	
	800	100	72	7	75.4	0.17	13.5	1.06	0.03	0.17	0.86	3.98	4.78	0.03	95.8	5.6	4.09	5.07	28.9	62.2	2.1
					0.9	0.02	0.3	0.11	0.03	0.03	0.07	0.16	0.16	0.03	1.3	0.42	0.01	0.03	1.6	0.9	
850	100	48	9	74.1	0.25	13.7	1.54	0.04	0.21	1.19	4.35	4.60	0.00	96.1	7.42	3.96	4.56	49.6	45.3	0.8	
				0.2	0.02	0.1	0.08	0.06	0.07	0.02	0.24	0.10	0.06	0.3	0.34	0.01	0.05	0.9	1.3		
850	80	48	5	74.4	0.27	13.3	1.49	0.02	0.20	0.92	2.97	6.32	0.04	95.8	6.99	3.51	4.79	35.6	61	10.4	
				0.5	0.05	0.1	0.04	0.03	0.02	0.02	0.06	0.08	0.03	0.5	0.56	0.01	0.07	1.8	1.4		
850	60	48	5	75.3	0.27	12.9	1.44	0.10	0.14	0.73	2.90	6.17	0.00	97.7	5.49	2.99	5.19	25.3	68.5	16.4	
				1.2	0.04	0.6	0.27	0.13	0.03	0.07	0.56	0.21	0.00	1.2	0.33	0.02	0.09	0.7	0.7		
900	50	48	11	73.8	0.25	13.8	1.68	0.02	0.24	1.25	4.26	4.59	0.10	97.8	7.91	2.59	4.94	33.7	54.4	2.6	
				0.5	0.05	0.1	0.06	0.05	0.07	0.02	0.19	0.14	0.09	0.6	0.22	0	0.07	2.3	1.2		
TEQ34	750	300	120	5	71.8	0.24	16.2	1.45	0.03	0.19	1.24	4.15	4.58	0.14	93.2	8.83	7.33	4.5	34.6	62.8	4.7
					1.6	0.23	0.2	0.64	0.07	0.22	0.12	0.75	0.48	0.05	0.4	0.68	0.11	0.13	1.6	2.2	
	750	250	120	7	71.9	0.36	15.2	1.41	0.04	0.23	0.65	5.62	4.64	0.15	93.5	4.65	6.94	4.45	22.3	72.9	13.5
					0.9	0.20	0.4	0.38	0.06	0.21	0.08	0.38	0.35	0.09	0.4	0.64	0.06	0.13	1.6	2.5	
750	250	48		70.9	0.44	15.4	1.79	0.09	0.17	0.95	5.17	4.92	0.12	92.6	5.29	6.9	4.45	23	73.8	12.4	
				1.3	0.65	0.3	0.94	0.04	0.19	0.11	0.27	0.17	0.10	0.7	0.83	0.08	0.11	0.2	1.5		
750	200	120	4	70.1	0.73	15.5	2.76	0.07	0.07	0.61	4.89	5.23	0.05	93.7	4.16	6.1	4.67	17	71.4	19.4	
				1.4	0.43	0.3	2.02	0.03	0.08	0.15	0.92	0.48	0.04	0.9	0.96	0.05	0.16	1.1	1.3		

Table 4.4: Glass Compositions (cont.)

T (°C)	Pressure (MPa)	Duration (h)	n	SiO ₂	TiO ₂	Al ₂ O ₃	FeO	MnO	MgO	CaO	Na ₂ O	K ₂ O	P ₂ O ₅	Total	liquidAn# ¹	wt% H ₂ O ²	Viscosity ³ (log ₁₀ Pas)	XAn	XAb	% xtal ⁴
800	250	48	7	69.5	0.31	16.3	1.94	0.08	0.24	1.42	5.46	4.59	0.10	93.5	9.04	6.73	3.98	29.5	68.3	0.8
				0.9	0.13	0.4	0.85	0.02	0.15	0.13	0.35	0.10	0.05	0.8	0.76	0.04	0.09	0.9	2.2	
800	200	48	6	68.9	0.39	16.6	2.44	0.06	0.20	1.19	5.55	4.61	0.08	93.0	7.76	5.93	4.14	27.3	67.9	1.6
				0.9	0.27	0.7	1.73	0.04	0.09	0.08	0.32	0.18	0.08	1.3	0.62	0.08	0.13	0.7	0.8	
800	150	48	8	70.1	0.29	15.7	1.85	0.09	0.29	1.15	5.36	5.02	0.11	94.0	7.37	5.11	4.39	20.6	67.3	10.3
				0.5	0.03	0.2	0.17	0.03	0.03	0.10	0.22	0.19	0.05	0.6	0.5	0.02	0.05	1.4	2.3	
900	50	48	8	70.6	0.40	15.1	2.00	0.07	0.24	0.89	4.98	5.54	0.12	97.4	5.84	2.6	4.73	18.9	65.7	1.4
				0.8	0.03	0.4	0.22	0.04	0.07	0.15	0.31	0.18	0.07	0.3	0.12	0.0	0.02	2	2.3	

Table 4.5: Plagioclase Compositions

	T (°C)	Pressure (MPa)	Duration (h)	n	SiO ₂	TiO ₂	Al ₂ O ₃	Fe ₂ O ₃	MnO	MgO	CaO	BaO	Na ₂ O	K ₂ O	Total	XAn	XAb	XOr
MLV44	750	200	96	6	62.5	0.05	23.7	0.27	0.01	0.05	5.31	0.15	7.04	1.08	100.2	27.5	65.9	6.6
				$\pm 1\sigma$	1.3	0.05	0.5	0.16	0.02	0.04	0.23	0.06	0.23	0.10	0.9	0.8	1.0	0.6
	750	200	48	5	62.2	0.06	23.9	0.29	0.01	0.05	5.34	0.13	7.13	1.08	100.1	27.3	66.1	6.6
				$\pm 1\sigma$	1.1	0.06	0.3	0.17	0.02	0.04	0.18	0.04	0.18	0.11	0.9	0.6	1.0	0.7
	750	100	72	4	65.9	0.10	20.0	0.69	-0.01	0.12	3.52	0.28	6.65	2.05	99.9	19.9	67.2	12.6
				$\pm 1\sigma$	0.1	0.07	0.4	0.24	0.04	0.10	0.19	0.06	0.14	0.30	0.6	0.6	0.5	1.2
800	100	72	4	64.9	0.05	21.6	0.66	0.03	0.09	4.40	0.28	6.46	1.59	100.1	24.5	65.0	10.6	
			$\pm 1\sigma$	1.0	0.03	0.4	0.06	0.04	0.03	0.41	0.09	0.27	0.15	0.8	0.8	0.8	1.1	
950	30	48	3	65.2	0.16	18.3	0.61	0.01	0.12	4.62	-	7.06	2.85	98.9	22.2	61.4	16.4	
			$\pm 1\sigma$	0.7	0.05	0.2	0.12	0.02	0.03	0.19	-	0.31	0.24	0.4	0.4	1.3	1.7	
MLV36	750	220	48	4	58.0	0.01	26.6	0.35	0.02	0.03	8.77	-	6.19	0.60	100.6	42.4	54.2	3.5
				$\pm 1\sigma$	0.6	0.01	0.3	0.03	0.02	0.01	0.20	-	0.38	0.08	0.4	1.4	1.5	0.5
	750	200	120	9	60.5	0.03	24.2	0.34	0.00	0.03	6.12	0.14	7.39	0.79	99.5	29.9	65.4	4.6
				$\pm 1\sigma$	1.3	0.04	0.7	0.08	0.04	0.03	0.33	0.08	0.32	0.15	0.8	1.2	1.1	1.0
	750	200	48	8	60.2	0.11	24.9	0.58	0.06	0.19	5.91	0.12	7.24	0.43	99.7	30.3	67.1	2.6
				$\pm 1\sigma$	0.7	0.08	0.3	0.25	0.08	0.18	0.28	0.09	0.31	0.18	0.6	0.8	1.5	1.0
	750	100	72	4	63.7	0.13	21.5	0.74	0.03	0.17	3.60	0.27	7.14	2.03	99.8	19.0	68.3	12.8
				$\pm 1\sigma$	0.3	0.09	0.4	0.21	0.04	0.11	0.20	0.12	0.10	0.03	0.2	0.9	0.8	0.2
	800	150	48	6	62.0	0.02	25.0	0.26	0.01	0.04	7.06	0.03	5.43	0.76	100.2	39.9	55.0	5.1
				$\pm 1\sigma$	1.6	0.01	0.4	0.06	0.02	0.03	0.42	-	0.85	0.12	0.9	3.0	3.1	0.5
	800	100	72	5	62.8	0.16	23.0	0.67	-0.01	0.08	5.62	0.14	6.67	1.44	100.6	28.9	62.2	8.8
				$\pm 1\sigma$	0.6	0.17	0.3	0.23	0.02	0.04	0.39	0.12	0.10	0.20	0.3	1.6	0.9	1.3

Table 4.5: Plagioclase Compositions (cont.)

	T (°C)	Pressure (MPa)	Duration (h)	n	SiO ₂	TiO ₂	Al ₂ O ₃	Fe ₂ O ₃	MnO	MgO	CaO	BaO	Na ₂ O	K ₂ O	Total	XAn	XAb	XOr
	850	100	48	5	59.5	0.04	25.0	0.66	-0.01	0.09	8.76	0.11	4.26	0.80	99.3	49.6	45.3	5.3
				$\pm 1\sigma$	1.2	0.03	0.4	0.07	0.01	0.02	0.26	0.09	0.62	0.13	0.7	0.9	1.3	1.0
	850	80	48	6	59.4	0.13	23.5	0.35	0.09	0.05	7.74	-	7.33	0.63	99.3	35.6	61.0	3.4
				$\pm 1\sigma$	1.3	0.03	0.4	0.07	0.12	0.03	0.53	-	0.38	0.29	0.4	1.8	1.4	1.4
	850	60	48	5	63.1	0.22	21.2	0.62	0.04	0.14	5.04	-	7.53	1.03	98.9	25.3	68.5	6.2
				$\pm 1\sigma$	1.2	0.29	0.4	0.20	0.08	0.16	0.25	-	0.40	0.02	0.9	0.7	0.7	0.3
	900	50	48	4	63.8	0.10	21.8	0.66	0.01	0.12	6.20	-	5.52	1.81	100.0	33.7	54.4	11.9
				$\pm 1\sigma$	1.0	0.03	1.5	0.18	0.01	0.01	0.78	-	0.41	0.41	1.2	2.3	1.2	3.3
TEQ34	750	300	120	7	59.1	0.09	24.4	0.54	0.01	0.12	7.22	0.35	7.23	0.44	99.5	34.6	62.8	2.6
				$\pm 1\sigma$	1.0	0.12	0.8	0.43	0.02	0.27	0.77	0.11	0.64	0.15	0.7	1.6	2.2	1.0
	750	250	120	9	62.4	0.25	21.9	0.67	-0.01	0.08	4.55	0.10	8.26	0.82	99.0	22.3	72.9	4.8
				$\pm 1\sigma$	1.2	0.48	0.8	0.65	0.10	0.05	0.20	0.12	0.51	0.41	1.5	1.6	2.5	2.4
	750	250	48	5	62.4	0.24	23.6	0.46	-0.01	0.20	4.29	0.18	7.59	0.50	99.5	23.0	73.8	3.2
				$\pm 1\sigma$	0.4	0.14	0.4	0.27	0.07	0.09	0.10	0.10	0.26	0.23	0.5	0.2	1.5	1.5
	750	200	120	8	63.8	0.23	20.6	1.26	-0.01	0.24	3.15	0.17	7.29	1.80	98.6	17.0	71.4	11.6
				$\pm 1\sigma$	1.1	0.12	0.8	0.86	0.09	0.16	0.25	0.06	0.35	0.35	1.2	1.1	1.3	2.2
	800	250	48	8	61.3	0.11	23.4	0.50	0.06	0.25	5.82	0.27	7.46	0.36	99.5	29.5	68.3	2.2
				$\pm 1\sigma$	0.6	0.07	0.7	0.20	0.11	0.17	0.07	0.11	0.44	0.31	0.8	0.9	2.2	1.9
	800	200	48	5	61.9	0.05	23.5	0.49	0.01	0.03	5.53	0.11	7.60	0.82	99.7	27.3	67.9	4.8
				$\pm 1\sigma$	0.7	0.09	1.2	0.10	0.01	0.02	0.16	0.11	0.29	0.05	1.0	0.7	0.8	0.3
	800	150	48	5	64.3	0.19	21.9	0.94	0.02	0.07	3.42	0.43	6.17	1.69	99.4	20.6	67.3	12.2
				$\pm 1\sigma$	0.6	0.07	0.3	0.37	0.04	0.05	0.23	0.15	0.57	0.11	0.4	1.4	2.3	1.1
	900	50	48	6	63.5	0.22	20.9	1.35	0.00	0.07	3.51	0.51	6.74	2.38	99.3	18.9	65.7	15.4
				$\pm 1\sigma$	1.0	0.07	0.4	0.57	0.05	0.03	0.44	0.12	0.53	0.24	0.3	2.0	2.3	2.2

TEQ-34 (67 wt% SiO₂ dacite)

The results of the phase-equilibrium experiments for TEQ-34 are summarized in a phase diagram in Fig. 4.4. At the estimated pre-eruptive temperature (760 ± 16 °C) obtained from the two Fe-Ti oxide thermometer in the natural sample, the experimental phase diagram predicts that the plagioclase-in curve is located at $P_{\text{H}_2\text{O}} > 300$ MPa and, therefore, at melt water concentrations >7.3 wt%. Thus, the most calcic plagioclase composition at the pre-eruptive temperature is not recorded by the experiments in this study. The phase equilibrium experiments further predicts that the equilibrium composition of plagioclase at $760 (\pm 16)$ °C varies from $\sim\text{An}_{35}$ to $\sim\text{An}_{17}$ as the $P_{\text{H}_2\text{O}}$ varies from 300 to 200 MPa, which leads to a variation in melt water concentration from ~ 7.3 to ~ 6.0 wt%. This range in plagioclase composition overlaps with the range observed in the natural sample (Fig. 4.2). The phase diagram additionally shows that biotite is stable at temperatures <900 °C, which is consistent with the occurrence of biotite in the natural sample (Crabtree and Lange, 2011). The only discrepancy between the experimental phase diagram and the natural sample is the absence of orthopyroxene in the experimental run products, which can be attributed to the much higher $f\text{O}_2$ of the experiments ($\Delta\text{NNO} > 1$) relative to the natural sample ($\Delta\text{NNO} = -0.9$; Fig. 4.2), a difference of two orders of magnitude or more in $f\text{O}_2$.

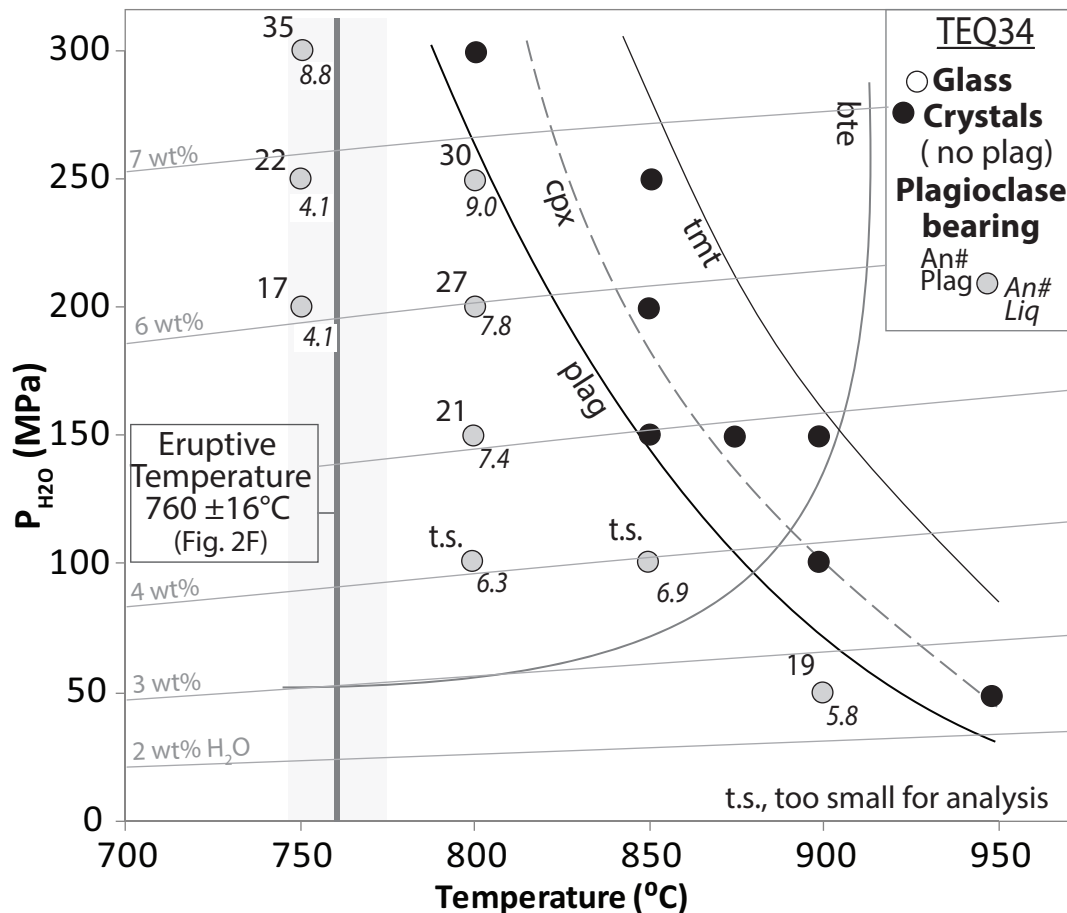


Figure 4.4: Phase equilibrium diagram for TEQ34. The analyses of experimental glasses and plagioclase are reported in tables 4.4 and 4.5, and clinopyroxene are reported in Appendix C Tables C7. In some experiments, plagioclase was identified using EDS spectra but was not able to be measured due to small sizes (<5µm). Isopleths of dissolved melt water are also shown, calculated with water solubility model of Liu et al. (2005). Abbreviations are: plag, plagioclase; cpx, clinopyroxene; bte, biotite; tmt, titanomagnetite. The plagioclase that was present and too small to be measured is noted on the phase equilibrium diagram with the abbreviation “t.s.”

MLV-36 (73 wt% SiO₂ rhyolite)

The results of the phase equilibrium experiments for MLV-36 are summarized with a phase diagram in Fig. 4.5. At the estimated pre-eruptive temperature (852 ± 12 °C) obtained from the two Fe-Ti oxide thermometry in the natural sample, the phase equilibrium experiments predict that the plagioclase-in curve is located at P_{H2O} = 100 MPa and, therefore, a calculated melt water concentration of ~4.0 wt%. The phase diagram shows that the equilibrium composition of plagioclase at 852 (± 12) °C varies from ~An₅₀

MLV-44 (75 wt% SiO₂ rhyolite)

The results of the phase-equilibrium experiments for MLV-44 are summarized in a phase diagram in Fig. 4.6. At the estimated pre-eruptive temperature (932 ± 15 °C) obtained from two Fe-Ti oxide thermometry in the natural sample, the experimental phase diagram predicts that the plagioclase-in curve is located at $P_{\text{H}_2\text{O}} = 40$ MPa and, therefore, at a melt water concentration of ~ 2.1 wt%. Isopleths of anorthite content (An_{22} , An_{24} , An_{26}) are shown as light grey dashed lines. The phase diagram illustrates that the equilibrium composition of plagioclase at $932 (\pm 12)$ °C varies from $\sim \text{An}_{28}$ to $\sim \text{An}_{22}$ as $P_{\text{H}_2\text{O}}$ varies from 38 to 25 MPa, which leads to a variation in melt water concentration from ~ 2.1 to ~ 1.7 wt%. This range in plagioclase composition overlaps with the range observed in the natural sample (Fig. 4.2). The phase diagram additionally shows that biotite is only stable at temperatures ≤ 825 °C, which is consistent with the absence of biotite in the natural sample. All other experimentally observed phases (clinopyroxene, orthopyroxene, titanomagnetite; Table 4.2) were found in the natural sample, whereas ilmenite was too sparse to identify in the experimental run products.

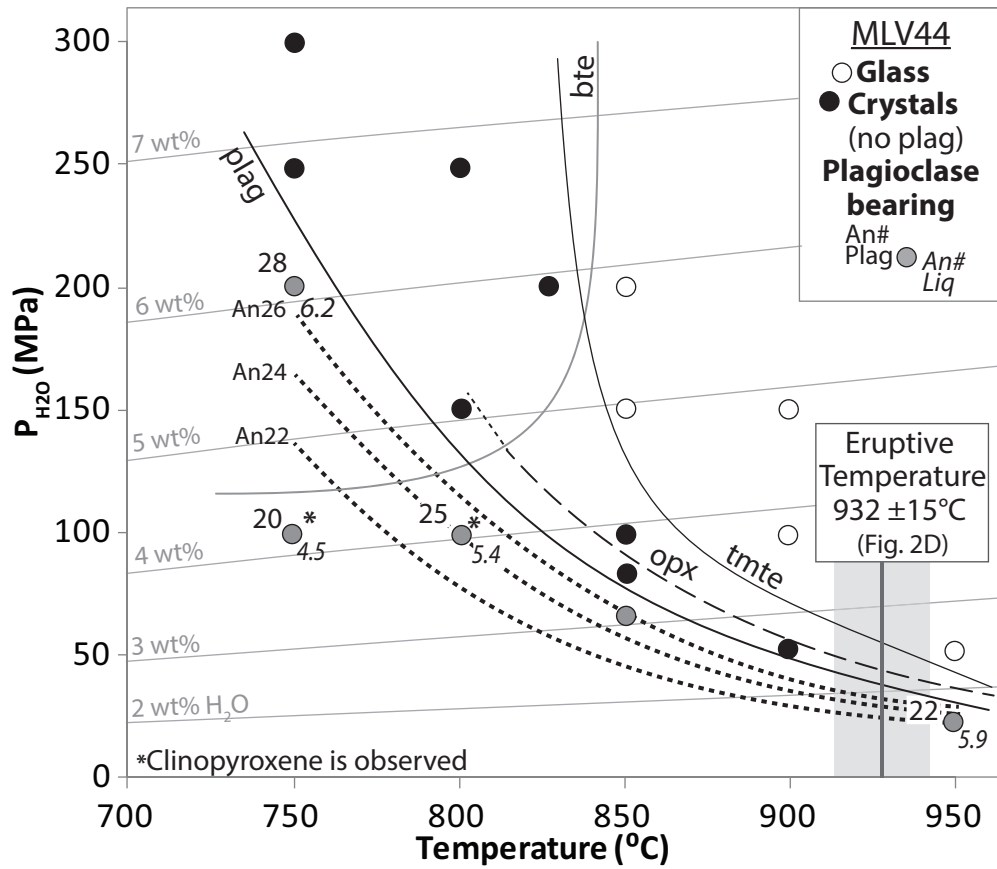


Figure 4.6: Phase equilibrium diagram for MLV44. The analyses of experimental glasses, plagioclase are reported in Tables 4 and 5, and orthopyroxene, and clinopyroxene are reported in Appendix C Tables C6-C7. Also shown are isopleths of anorthite content (An_{22} , An_{24} , and An_{26}). Isopleths of dissolved melt water are also shown, calculated with water solubility model of Liu et al. (2005). Abbreviations are: plag, plagioclase; opx, orthopyroxene; bte, biotite; tmte, titanomagnetite

Isothermal Decompression Experiments on MLV-36

Isothermal (850°C) decompression experiments that were conducted at a rate of 2.9 MPa/hr, whether quenched at 89 MPa or 58 MPa, led to run products that were devoid of crystals. In contrast, isothermal (850°C) decompression experiments performed at the slower rate of 0.8 MPa/hr, whether quenched to 89 or 58 MPa, resulted in run products that contained plagioclase, orthopyroxene, ilmenite and titanomagnetite, all of which are found in the natural sample. Notably, clinopyroxene was only observed in the decompression experiments (0.8 MPa/hr) quenched to 58 MPa. This is fully consistent with the phase-equilibrium diagram in Fig. 4.5, which shows that the clinopyroxene-in

curve (at 850°C) occurs at a $P_{\text{H}_2\text{O}}$ of ~ 70 MPa, lower than that for all other mineral-in curves. Compositions of the plagioclase crystals and matrix glass in each of the decompression run products are presented in Table 4.6; other mineral phases were too small for quantitative microprobe analyses.

The experimental charge from the decompression experiment quenched at $P_{\text{H}_2\text{O}} = 89$ MPa contains a population of plagioclase crystals that span a relatively wide range of composition (An_{50} - An_{30}). For those crystals large enough for microprobe analyses, the compositions range from An_{47} to An_{37} . The results of the An map and the BSE standard (discussed in the methods section) are shown in Fig. 4.7A, as a BSE image of the standard (Fig. 4.7A1), an An-map (Fig. 4.7A2), and a histogram of microprobe analyses from the standard, along with a histogram of pixels v. mol% An recorded by the An-map (Fig. 4.7A3). The range of plagioclase compositions and their relative abundances determined by the element maps (see Methods Section) are shown in Fig. 4.7B and C for one region of the decompression quenched at 89 MPa (Fig. 4.7B) and one region of the decompression quenched at 58 MPa. The results approximate a Gaussian distribution with a peak at $\sim \text{An}_{40}$, which is shifted to more sodic compositions by ~ 5 mol% An, compared to the natural sample.

Table 4.6: Glass and Plagioclase Compositions from Decompression Experiments

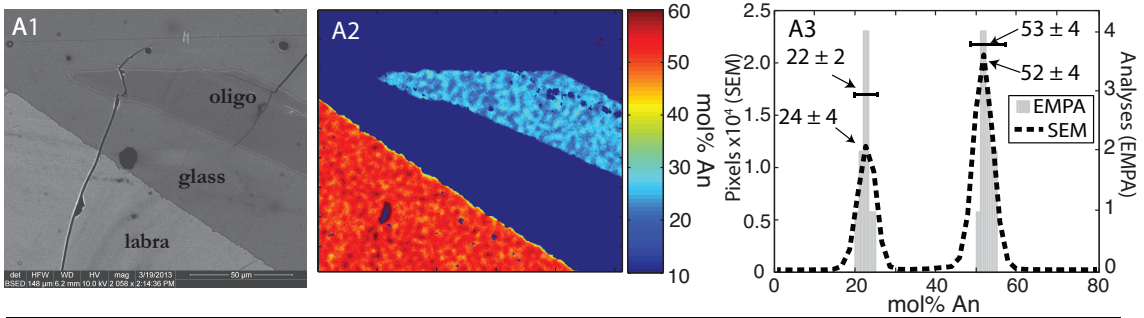
Pf (MPa)	Duration (h)	Phase	n	SiO ₂	TiO ₂	Al ₂ O ₃	Fe ₂ O ₃	MgO	CaO	Na ₂ O	K ₂ O	Total	wt% H ₂ O	XAn	XAb	XOr	% xtal
89	76	glass	5	73.3	0.23	13.9	1.77	0.21	0.90	3.28	6.51	96.7	3.7	6.62			6%
89	76	plag		59.6	0.06	25.2	0.19	0.03	7.68	6.31	0.78	99.8		38.3	57.0	4.6	
89	76	plag		58.4	0.00	24.9	0.38	0.04	7.93	6.58	0.74	99.0		38.3	57.5	4.3	
89	76	plag		58.0	0.10	25.1	0.40	0.05	8.80	6.64	0.88	100.2		40.2	55.0	4.8	
89	76	plag		59.3	0.08	25.6	0.29	0.06	7.60	6.25	0.84	100.1		38.1	56.8	5.0	
89	76	plag		58.4	0.03	25.7	0.29	0.08	7.98	6.36	0.83	99.7		39.0	56.2	4.8	
89	76	plag		58.3	0.15	24.9	0.21	0.00	8.45	6.79	0.79	99.7		39.0	56.7	4.4	
89	76	plag		58.9	0.03	25.8	0.21	0.00	7.45	6.76	0.66	99.8		36.4	59.8	3.8	
89	76	plag		58.0	0.16	25.0	0.19	0.00	8.58	7.24	0.78	100.0		37.9	57.9	4.1	
89	76	plag		58.1	0.07	25.3	0.38	0.14	8.40	7.17	0.87	100.4		37.5	57.9	4.6	
89	76	plag		57.9	0.07	25.9	0.48	0.00	7.98	7.14	0.14	99.6		37.9	61.3	0.8	
89	76	plag		58.0	0.12	26.2	0.80	0.06	7.56	5.31	1.52	99.6		39.8	50.6	9.5	
89	76	plag		57.9	0.07	27.0	0.82	0.02	7.45	5.05	0.35	98.7		43.8	53.8	2.4	
89	76	plag		56.3	0.04	26.8	0.29	0.04	9.18	5.57	0.47	98.7		46.3	50.9	2.8	
89	76	plag		57.1	0.10	26.2	0.40	0.47	7.98	6.26	0.77	99.3		39.5	56.0	4.5	
89	76	plag		57.4	0.15	24.9	0.46	0.32	7.94	6.13	0.85	98.1		39.6	55.4	5.0	
89	76	plag		58.5	0.01	26.4	0.40	0.04	7.81	6.66	0.72	100.7		37.7	58.2	4.1	
89	76	plag		55.1	0.10	27.8	0.69	0.10	9.91	5.60	1.20	100.4		46.2	47.2	6.7	
89	76	plag		57.4	0.13	24.6	0.84	0.23	7.68	6.51	0.84	98.3		37.5	57.6	4.9	
89	76	plag		57.4	0.08	26.1	0.48	0.03	8.24	7.02	0.58	100.0		38.1	58.7	3.2	
89	76	plag		58.7	0.00	25.5	0.36	0.11	8.04	6.10	0.90	99.9		39.9	54.8	5.3	
89	76	plag		57.7	0.00	26.5	0.21	0.00	8.29	6.58	0.57	99.9		39.7	57.0	3.2	
89	76	plag		58.9	0.04	25.1	0.08	0.04	7.70	6.25	0.79	98.2		38.6	56.7	4.7	
89	76	plag		58.8	0.06	25.0	0.50	0.08	7.92	5.55	0.80	98.8		41.9	53.1	5.1	
89	76	plag		58.6	0.09	24.8	0.15	0.06	7.41	6.05	0.62	98.1		38.8	57.4	3.9	
89	76	plag		58.9	0.09	26.6	0.25	0.05	7.82	6.78	0.55	101.0		37.7	59.2	3.1	
89	76	plag		57.6	0.10	24.9	0.42	0.13	8.05	6.05	0.66	98.0		40.7	55.4	4.0	
89	76	plag		58.3	0.13	26.6	0.50	0.08	7.38	6.15	0.14	99.3		39.5	59.6	0.9	
89	76	plag		56.3	0.12	26.4	0.44	0.02	8.61	7.21	0.99	100.1		37.7	57.1	5.2	
89	76	plag		56.4	0.01	26.7	0.36	0.00	8.37	7.14	0.57	99.8		38.1	58.8	3.1	
89	76	plag		55.5	0.05	26.7	0.06	0.00	10.3	6.93	0.79	100.7		43.4	52.7	4.0	
58	120	glass	7	74.7	0.25	13.5	1.68	0.24	0.85	3.82	6.45	97.2	2.9	5.69			11%
58	120	plag		57.5	0.06	25.0	0.21	0.04	7.98	7.33	0.74	98.9		36.1	60.0	4.0	
58	120	plag		58.6	0.03	25.0	0.15	0.02	6.72	6.53	0.99	98.1		34.1	59.9	6.0	
58	120	plag		58.8	0.02	24.4	0.25	0.00	8.32	7.16	0.62	99.7		37.8	58.9	3.4	
58	120	plag		59.1	0.10	25.1	0.36	0.08	6.43	6.64	0.90	98.7		33.0	61.6	5.5	
58	120	plag		59.3	0.09	24.6	0.42	0.08	6.80	7.25	0.86	99.6		32.5	62.7	4.9	
58	120	plag		59.0	0.11	24.1	0.15	0.04	6.66	7.64	0.88	98.6		30.9	64.2	4.8	
58	120	plag		58.7	0.02	24.8	0.21	0.00	7.70	7.38	0.86	99.6		34.9	60.5	4.6	
58	120	plag		59.3	0.00	23.6	0.31	0.03	7.39	7.75	0.88	99.2		32.9	62.4	4.7	
58	120	plag		61.4	0.06	24.7	0.25	0.00	6.18	7.61	0.73	101.1		29.7	66.2	4.2	
58	120	plag		63.8	0.00	23.1	0.15	0.08	6.02	7.40	0.70	101.4		29.7	66.2	4.1	
58	120	plag		58.3	0.08	24.2	0.25	0.02	7.57	8.34	0.84	99.6		32.0	63.8	4.2	
58	120	plag		59.2	0.19	25.0	0.36	0.00	6.57	7.24	0.74	99.3		32.0	63.8	4.3	
58	120	plag		60.1	0.05	24.2	0.33	0.05	6.70	7.84	1.33	100.8		29.8	63.2	7.0	

Table 4.6: Glass and Plagioclase Compositions from Decompression Experiments (cont.)

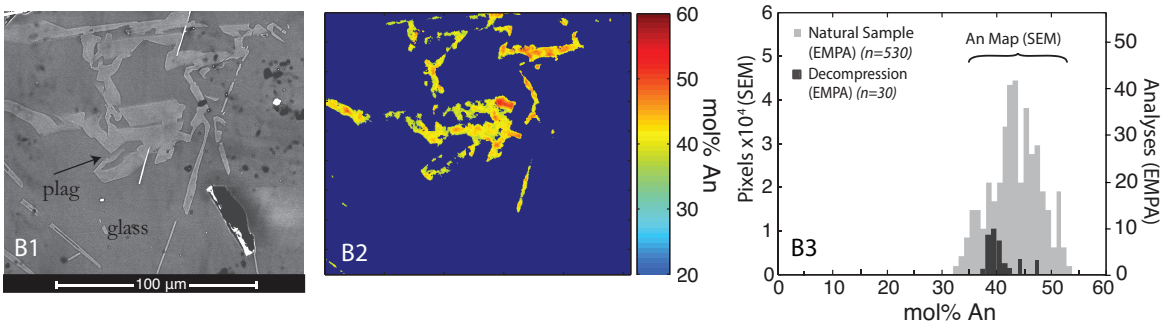
Pf (MPa)	Duration (h)	Phase	n	SiO ₂	TiO ₂	Al ₂ O ₃	Fe ₂ O ₃	MgO	CaO	Na ₂ O	K ₂ O	Total	wt% H ₂ O	XAn	XAb	XOr	% xtal
58	120	Plag		58.3	0.09	24.9	0.34	0.05	7.16	6.86	0.69	98.4		35.1	60.9	4.0	
58	120	plag		57.9	0.03	25.0	0.04	0.02	8.51	8.26	0.74	100.6		34.9	61.4	3.6	
58	120	plag		57.3	0.06	25.9	0.44	0.03	7.72	6.78	0.68	99.1		37.1	59.0	3.9	
58	120	plag		57.2	0.04	26.1	0.38	0.06	7.88	6.59	0.61	99.1		38.4	58.1	3.5	
58	120	plag		57.0	0.04	25.1	0.19	0.07	8.09	7.97	0.87	99.3		34.3	61.2	4.4	
58	120	plag		57.0	0.01	27.7	0.36	0.03	7.86	7.40	0.68	101.2		35.6	60.7	3.7	
58	120	plag		56.9	0.06	25.8	0.36	0.00	8.02	6.82	0.65	98.6		37.9	58.4	3.7	
58	120	plag		56.7	0.04	25.1	0.36	0.00	8.73	7.52	0.60	99.0		37.9	59.0	3.1	
58	120	plag		56.2	0.00	25.9	0.23	0.05	7.97	7.44	0.50	98.4		36.2	61.1	2.7	
58	120	plag		58.1	0.00	24.9	0.44	0.06	8.28	7.39	0.74	99.9		36.8	59.3	3.9	
58	120	plag		56.6	0.23	25.4	0.42	0.07	8.60	7.65	0.61	99.7		37.1	59.7	3.1	
58	120	plag		59.7	0.04	24.1	0.50	0.01	7.12	6.61	0.78	98.8		35.6	59.8	4.7	
58	120	plag		57.6	0.00	25.8	0.27	0.02	7.36	7.20	0.66	98.9		34.7	61.5	3.7	
58	120	plag		62.2	0.00	24.8	0.57	0.07	6.68	6.26	0.89	100.5		35.0	59.4	5.6	
58	120	plag		59.3	0.03	23.1	0.31	0.07	6.88	7.62	1.20	98.5		31.1	62.4	6.5	
58	120	plag		61.3	0.02	22.7	0.48	0.00	5.48	7.55	1.29	98.9		26.5	66.1	7.4	
58	120	plag		60.0	0.03	25.1	0.31	0.00	6.62	7.00	0.86	99.9		32.6	62.4	5.1	
58	120	plag		58.6	0.15	22.9	0.17	0.11	6.96	9.31	0.83	99.0		28.1	68.0	4.0	

Where XAn of liquid compositions refers to the liquid An-number, and % Xtal refers to the crystallinity calculated with linear regression and the most calcic and most sodic plagioclase compositions, the experimental glass compositions and the bulk composition reported in Table 4.1

A: BSE Standard



B&C: MLV36 Decompression from 150 to 89 MPa at 0.8 MPa/hr



D&E: MLV36 Decompression from 150 to 58 MPa at 0.8 MPa/hr

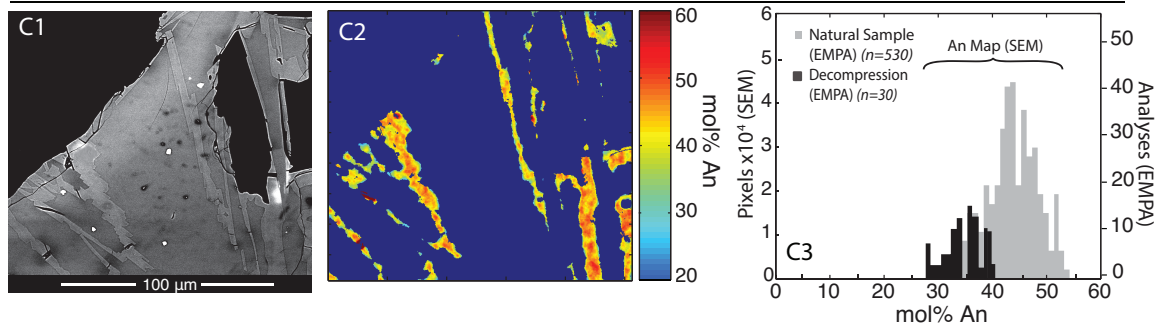


Figure 4.7: (a) Scanning electron microscope (SEM) (1) and Anorthite (An) maps (2) for the BSE Standard, (b) the isothermal (850°C) decompression experiment from 150 to 89 MPa at 0.8 MPa/hr, and (c) the isothermal (850°C) decompression experiment from 150 to 58 MPa at 0.8 MPa/hr. Images ending in 1 correspond to the SEM image, images ending in (2) are the An-maps processed using element maps and MatLab (see text), and those ending in C are the analyses of plagioclase from the electron microprobe, element maps, and those reported for the natural sample (Fig. 4.2b).

The experimental charge from the decompression experiment quenched at $P_{H_2O} = 58$ MPa contain a population of plagioclase crystals that span a similar range of composition as those quenched at $P_{H_2O} = 89$ MPa, except that they extend to more sodic compositions (An₅₀-An₂₅). The composition of crystals large enough to be quantitatively

analyzed with the microprobe range from An₄₀-An₂₇, whereas the element maps of the experimental charge capture plagioclase with compositions >An₄₅, as illustrated in Fig. 4.7B and C. The variation in the relative abundance of plagioclase compositions in each map reflects the small size of each map region relative to the size of the experimental charge overall. The observation that plagioclase in Fig. 4.7C closely follows the natural distribution of plagioclase compositions in MLV-36 demonstrates that isothermal decompression under H₂O fluid-saturated conditions at 850°C is capable of producing the observed range of plagioclase in the natural sample.

4.5 DISCUSSION

Two central questions motivated this experimental study. First, does the entire compositional range of plagioclase in each of the natural obsidians reflect phenocryst crystallization, or do some xenocrysts occur? Second, for those plagioclase crystals that are determined to be phenocrysts, did crystallization occur because of cooling and/or degassing during magma ascent? The phase-equilibrium experiments can be used to evaluate both questions, whereas the decompression experiments, along with textural evidence from the natural samples, provide additional insights into the second question.

What Proportion of the Plagioclase Crystals in the Natural Samples are Phenocrysts vs. Xenocrysts?

TEQ-34

TEQ-34 is the natural specimen with the widest compositional range of plagioclase phenocrysts, An₄₅-An₇, and all possible pairings of coexisting ilmenite and titanomagnetite give a temperature of 760 ± 16°C. The most calcic plagioclase grown in

the phase-equilibrium experiments is An₃₅ at 750°C and P_{H₂O}=300 MPa (7.1 wt% H₂O; Fig. 4.4). It is clear from Fig. 4.4 that the plagioclase-in curve occurs at P_{H₂O} > 300 MPa at 750°C, which requires that the near-liquidus plagioclase composition is more calcic than An₃₅ owing to the effect of increasing melt water concentration with P_{H₂O}. Also, Fig. 4.4 shows that a difference in P_{H₂O} of only 50 MPa at 750°C, from 300 to 250 MPa, leads to a relatively large change in the equilibrium plagioclase composition of >10 mol% An (An₃₅ to An₂₂). Therefore, it is fully expected that at P_{H₂O} = 350 MPa, which should be close to the plagioclase-in curve at 760°C, the equilibrium plagioclase is another 5-10 mol% An more calcic than An₃₅. The majority of the plagioclase phenocrysts observed in TEQ-34 (Fig. 4.2) have compositions ≤An₃₅, with only a small proportion with more calcic compositions (An₄₅₋₃₅). It is expected that these calcic compositions crystallize close to the plagioclase-in curve (P_{H₂O} >300 MPa) at 760°C and that they are present in the natural sample in low abundance because at small undercoolings (T_{plagioclase-in curve} – T_{melt}), both crystal growth rates and nucleation rates are low (Hammer & Rutherford, 2002; Couch *et al.*, 2003), a point that is explored in more detail below. Therefore, the evidence shows that all of the plagioclase crystals in TEQ-34 are plausible phenocrysts.

MLV-36

Plagioclase crystals that occur in the natural sample MLV-36 span a continuous range in composition, An₅₃₋₃₃, with a single core in one crystal that is ≥ An₆₀ and makes up <0.01% of the total sample (Fig. 4.2). All possible pairs of titanomagnetite and ilmenite give a temperature of 852 ± 12°C. The most calcic plagioclase grown in the phase-equilibrium experiments (Fig. 4.5) at 850°C is An₅₀ at P_{H₂O} = 100 MPa (4.1 wt%

H₂O), which is close to the most calcic plagioclase crystal observed in the continuous spread of compositions (An₅₃; Fig. 4.2). It is expected that plagioclase compositions slightly more calcic than An₅₀ (i.e., An₅₁₋₅₃) can crystallize from the melt at slightly higher P_{H₂O} and/or temperature. Therefore, based on the results of the phase equilibrium experiments (Fig. 4.5), the continuous spread of plagioclase compositions from An₅₃₋₃₃ could have crystallized from the liquid. In contrast, the An₆₀₋₆₃ composition found in a single core is inferred to be a xenocryst.

MLV-44

Plagioclase in MLV-44 spans a small range in composition, An₂₇₋₂₁, and all possible pairings of coexisting ilmenite and titanomagnetite from this sample give a temperature of 932 ± 15 °C (Fig. 4.2). Plagioclase crystals that grew in the phase equilibrium experiments span a similar range of composition (An₂₈₋₂₀) as those seen in the natural sample (Fig. 4.6). Therefore, the plagioclase crystals observed in MLV-44 are plausible phenocrysts.

Summary of phase-equilibrium experiments

The results of the phase-equilibrium experiments clearly demonstrate that nearly all the plagioclase crystals observed in the three natural obsidian samples could have grown from the liquid, with the exception of a single An₆₃₋₆₀ core in MLV-36 (< 0.01% of the sample), which is interpreted to be a xenocryst. The phase-equilibrium diagrams also show that remarkably small changes in P_{H₂O} (≤ 50 MPa) and/or temperature (≤ 50 °C) can lead to relatively large changes in plagioclase composition (>10 mol% An), suggesting that both degassing and cooling can produce a wide compositional range of

plagioclase phenocrysts. Before evaluating the relative importance of cooling and/or degassing in the three obsidian samples, the question of whether rapid degassing can lead to crystallization of *equilibrium* plagioclase compositions must first be addressed.

Degassing-Induced Crystallization of Equilibrium Plagioclase Compositions?

A comparison of the phase-equilibrium and decompression experiments performed on MLV-36 allows a test of whether *equilibrium* plagioclase compositions can crystallize during degassing, or whether there is a kinetic effect on the composition of plagioclase that is grown. From the phase-equilibrium diagram for MLV-36 (Fig. 4.5), it is seen that during decompression (0.8 MPa/hr) at 850°C, the equilibrium plagioclase composition expected to grow immediately after the plagioclase-in curve is crossed (at $P_{\text{H}_2\text{O}} = 105 \text{ MPa}$) $\sim \text{An}_{50}$. It is further expected that as $P_{\text{H}_2\text{O}}$ decreases during decompression, the composition of equilibrium plagioclase becomes increasingly sodic. Moreover, it is anticipated that in the quenched run products the most calcic plagioclase crystals that grew early in the decompression experiments will be preserved because of sluggish kinetics related to the CaAl-NaSi exchange reaction between calcic plagioclase and rhyolite melt (e.g., Morse & Nolan, 1984). From the SEM maps of the run products (Fig. 4.7), it is seen that plagioclase as calcic as An_{50} (red color) formed in both decompression experiments, albeit in low abundance and too small for microprobe analysis.

In the decompression experiment that quenched at $P_{\text{H}_2\text{O}} = 89 \text{ MPa}$, it is expected from the phase-equilibrium results that only plagioclase more calcic than An_{36} (equilibrium composition at $P_{\text{H}_2\text{O}} = 80 \text{ MPa}$; Fig. 4.5) should have crystallized. This is the case, as seen both in the SEM map and in microprobe analyses of plagioclase crystals

large enough to analyze (An₄₇₋₃₇). It is further expected that in the decompression experiment that quenched at P_{H₂O} = 58 MPa, plagioclase crystals more sodic than those observed in the experiment quenched to P_{H₂O} = 89 MPa should have grown. Again, this is the case, as seen from the microprobe analyses of plagioclase that range from An₄₀₋₂₇, extending into the compositional range predicted to form at P_{H₂O} <80 MPa (<An₃₆). Therefore, during the two decompression experiments performed at 0.8 MPa/hr, degassing-induced crystallization produced a range of *equilibrium* plagioclase compositions, in response to a progressive loss of dissolved water in the melt.

The evidence for equilibrium crystallization of plagioclase shows that equilibrium degassing of water from the melt must also have occurred, which is consistent with the experiments of Gardner *et al.* (1999). In that study, it was shown that equilibrium degassing of H₂O from high-silica (77 wt%) rhyolite melts occurs at decompression rates as high as 90 MPa/hr, which is an order of magnitude more rapid than those employed in this study (2.9 and 0.8 MPa/hr).

Diffusion Limited Growth Textures

Despite the demonstration that a range of *equilibrium* plagioclase compositions crystallized in the 0.8 MPa/hr decompression experiments (as a result of degassing), some of the plagioclase crystals in the run products display complex textures (Fig. 4.7). BSE images in Fig. 4.7 show that some plagioclase crystals are skeletal with melt interiors, others have faceted euhedral margins on one side and rounded margins on the other, whereas still other crystals display swallowtails. These complex textures are indicative of diffusion-limited crystal growth (Lofgren, 1974; Kirkpatrick, 1975; Roedder

et al., 2001; Shea & Hammer, 2013) and are expected to form when large undercoolings ($\Delta T = T_{\text{plagioclase-in curve}} - T_{\text{melt}}$; Fig. 4.8a) develop as a consequence of degassing.

The decompression experiment that ran from $P_{\text{H}_2\text{O}}$ of 150 to 89 MPa at a rate of 0.8 MPa/hour lasted 76 hours in total, of which approximately 18 hours was spent below the plagioclase-in curve (at $P_{\text{H}_2\text{O}} = \sim 105$ MPa). Immediately prior to quench, the magnitude of the undercooling is estimated to have been ~ 15 degrees (Fig. 4.5). Similarly, the decompression experiment that quenched at $P_{\text{H}_2\text{O}} = 58$ MPa, lasted 115 hours in total, of which approximately 57 hours were spent below the plagioclase-in curve. However, immediately prior to quench, the magnitude of undercooling is estimated to have been larger, namely ~ 50 degrees (Fig 4.5). In both decompression experiments, the plagioclase crystals that show the most pronounced diffusion limited growth textures are the most sodic compositions (An_{40-30} ; Fig. 4.7; Fig. 4.8a), namely those that grew at the largest undercooling immediately prior to quench.

Theoretical and experimental studies of diffusion-limited growth of crystals (e.g., Lofgren, 1974; Kirkpatrick, 1975; Roedder *et al.*, 2001; Couch *et al.*, 2003a,b; Shea & Hammer, 2013) demonstrate that skeletal and swallowtail textures develop in response to the depletion of mineral components in the melt phase immediately adjacent to a rapidly crystallizing mineral phase. Thus, it appears that it is the development of complex, rapid growth textures (e.g., skeletal and swallowtail), where crystal growth extends into melt regions where the plagioclase components are available, that allows nearly *equilibrium* plagioclase compositions to crystallize at large undercoolings.

Relative abundances and plagioclase zoning patterns

Another useful set of observations obtained from the decompression experiments is the relative abundance of calcic vs. sodic plagioclase in each run product, as well as the compositional zoning patterns seen among the plagioclase crystals. For example, in the two 0.8 MPa/hour decompression experiments, the most calcic plagioclase composition ($\sim\text{An}_{50}$) occurs in relatively low abundance compared to more sodic compositions ($\sim\text{An}_{40}$). This result is fully consistent with the well-established correlation between the degree of undercooling and both nucleation and crystal growth rates (e.g., Hammer & Rutherford, 2002; Couch *et al.*, 2003a).

In Fig. 4.8a, the degree of undercooling and the equilibrium plagioclase composition is shown for three $P_{\text{H}_2\text{O}}$ values for the decompression experiments at 850°C. At $P_{\text{H}_2\text{O}} = 100, 80$ and 60 MPa, the equilibrium plagioclase composition is $\text{An}_{50}, \text{An}_{36}$ and An_{25} , respectively, and the degree of undercooling is $\sim 5, \sim 25$ and ~ 50 degrees, respectively. The observation that plagioclase with compositions more calcic than An_{50} occurs in low abundances, both in the decompression experiments and in the MLV-36 natural sample (Fig. 4.8b), is consistent with the relationship between low degrees of undercooling and low nucleation and crystal growth rates (e.g., Hammer & Rutherford, 2002; Couch *et al.*, 2003). However, as the degree of undercooling increases, both nucleation rates and crystal growth rates increase, which causes the more sodic plagioclase compositions (e.g., $\sim\text{An}_{40}$) to occur in greater abundance, both in the decompression experimental run products and the natural sample (Fig. 4.8b).

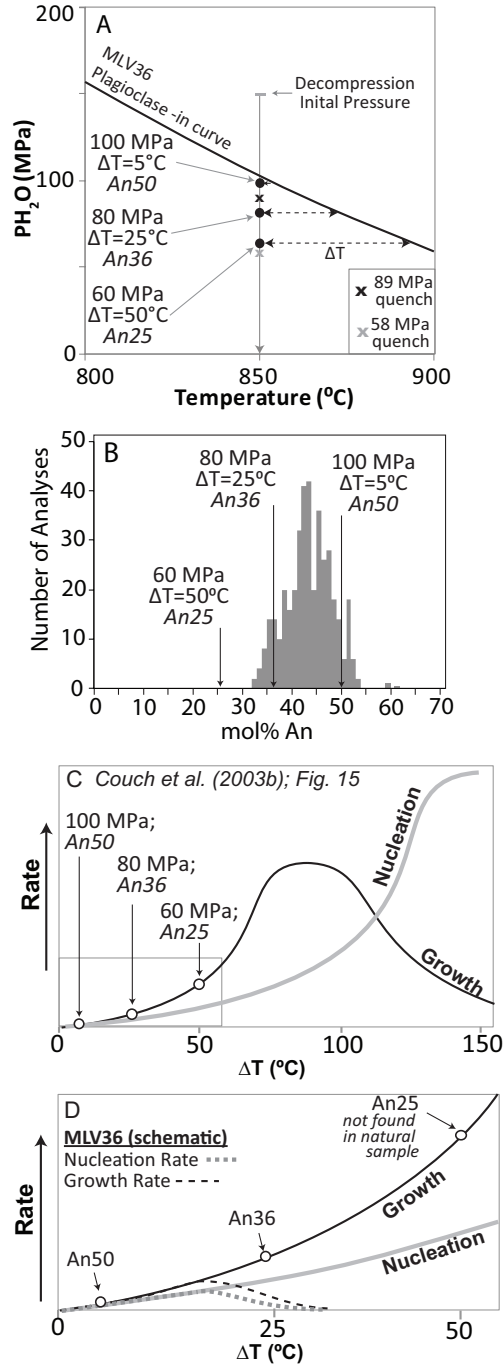


Figure 4.8: Panels a-d show the effects of degassing on crystal nucleation and growth. (a) The MLV36 plagioclase-in curve is shown with the experiments at 100, 80, and 60 MPa, along with plagioclase compositions that grew in phase equilibrium experiments (An50, An36, An25, respectively) and ΔT values ($T_{\text{in curve}} - T_{\text{experiment}}$). (b) Plagioclase grown in experiments and corresponding pressures and ΔT values are compared with the histogram of plagioclase found in the natural sample (Fig. 2b). Note that the natural samples have a smaller distribution than indicated by phase equilibria experiments. (c) The plagioclase compositions and undercoolings (ΔT values) are compared with the nucleation and growth rate curves presented by Couch *et al.* (2003b). (d) The relevant ΔT values from Couch *et al.* (2003b), a subset of Fig. 8c, are presented together the schematic nucleation and growth rate curves for the natural sample of MLV36. Curves are drawn based on the histogram of natural compositions; crystallization begins at \sim An50 ($\Delta T = 5^\circ\text{C}$) and plagioclase growth and nucleation ceases at \sim An36 ($\Delta T = 25^\circ\text{C}$).

Because it is not just crystal growth rate that increases with degree of undercooling, but also the nucleation rate (Fig. 4.8c), it is predicted that sodic plagioclase will not grow exclusively as rims on calcic cores, but will additionally nucleate directly from the melt when the equilibrium plagioclase is relatively more sodic (e.g., An₄₀). Thus, it is predicted that relatively unzoned plagioclase crystals of ~An₄₀ composition should form alongside other crystals that show compositional zoning from An₅₀₋₄₀. This variation is observed in the decompression experimental run products (Figs. 7) as well as in the natural sample of MLV-36 (Waters and Lange, 2013).

Overall plagioclase abundances: phase-equilibrium vs. decompression experiments

A final observation is that the overall abundance of plagioclase in the run products from the decompression experiments is consistently lower than the overall abundance of plagioclase found in the phase-equilibrium experiments quenched at similar P_{H₂O}-T conditions. For example, at 850°C and P_{H₂O} = 60 MPa, approximately 16% plagioclase crystallized in the phase-equilibrium experiment, whereas in the two decompression experiments quenched at P_{H₂O} = 58 MPa, approximately 11% plagioclase crystallized when the decompression rate was 0.8 MPa/hr and no plagioclase crystallized when the rate was 2.9 MPa/hr. This difference in overall abundance of crystallized plagioclase between phase-equilibrium experiments and decompression (degassing) experiments is also seen in the results from Couch *et al.* (2003a). In that study, the effects of undercooling driven by degassing are evaluated on plagioclase nucleation and growth rates during isothermal decompressions. Experiments of Couch *et al.* (2003b) were decompressed in eight nearly instantaneous drops in pressure from 160 MPa to four different final pressures (125, 100, 75 and 50 MPa). The difference between the

abundance of plagioclase grown during equilibrium experiments and decompression experiments is highlighted by the experiments quenched at 50 MPa. Plagioclase growth in equilibrium experiments at 50 MPa from Couch *et al.* (2003a) reaches 28 wt%, whereas plagioclase growth in the decompression experiment to 50 MPa is only 15 wt% (Couch *et al.*, 2003b), which is consistent with the observations from this study.

Another striking difference between the MLV-36 natural sample and the decompression experiment (0.8 MPa/hr) quenched at $P_{\text{H}_2\text{O}} = 58$ MPa is that plagioclase more sodic than An_{30} is not found in the natural sample, either as a phenocryst or microlite. In contrast, in the decompression run product, the abundance of sodic plagioclase (An_{40-27}) is relatively high, consistent with continued increases in crystal growth and nucleation rates as the degree of undercooling increases. A possible explanation for these differences in overall plagioclase abundances between the natural sample, the run products of the decompression experiments, and those from the phase-equilibrium experiments is the role that the *rate of degassing* plays in suppressing plagioclase nucleation.

Suppression of Plagioclase Nucleation and Crystal Growth with Rapid Degassing

From the decompression experiments performed at a rate of 2.9 MPa/hr, it is clear that plagioclase nucleation and crystal growth can be suppressed if degassing occurs at a sufficiently rapid rate. In these rapid decompression experiments, quenched at $P_{\text{H}_2\text{O}} = 89$ and 58 MPa, no crystals formed and only glass was found in the experimental charges. In the experiment that ran from $P_{\text{H}_2\text{O}} = 150$ to 89 MPa, at a rate of 2.9 MPa/hour, it is estimated that the sample spent around 4 hours below the plagioclase-in curve (at $P_{\text{H}_2\text{O}} = \sim 105$ MPa), which was apparently insufficiently long to allow nucleation and growth of

plagioclase. Similarly, in the experiment that ran from $P_{\text{H}_2\text{O}} = 150$ to 58 MPa, it is estimated that the sample spent an additional 11 hours traversing from $P_{\text{H}_2\text{O}} = 89$ to 58 MPa, which was also insufficient in duration to allow nucleation and growth of plagioclase. Since the decompression experiments that were performed at the slower rate of 0.8 MPa/hour did result in plagioclase crystallization, it is clear that the rate of decompression, which controls the rate of H_2O degassing from the melt, controls the suppression of plagioclase.

It is well known that crystal nucleation can be suppressed when a melt is cooled rapidly because of the corresponding rapid increase in melt viscosity, which correlates with an decrease in chemical diffusivity (e.g., Loomis, 1981; Brandeis & Jaupart, 1987). Similar to the effects of rapid cooling, rapid loss of dissolved water (during decompression of fluid-saturated melt) also causes a rapid increase in melt viscosity and decrease in chemical diffusivity, because of the strong effect that dissolved water has on melt viscosity (Zhang *et al.*, 2003; Hui and Zhang, 2007). Therefore, rapid degassing during decompression of fluid-saturated melt has the potential to suppress plagioclase nucleation and crystal growth rates, similar to the effects of rapid cooling, and may be the reason why the three natural obsidian samples in this study contain such sparse phenocrysts and hardly any microlites. The sparse abundance of phenocrysts in the natural samples provides the evidence that supports degassing as a mechanism to produced the observed phenocryst assemblages. Cooling of a magma at depth is largely due to conduction which is a slow process and may potentially take days to months, and the expected abundances of phenocrysts would be much greater than what is actually observed in the natural samples.

On a final note, it is not just the rate of degassing, or rate at which melt viscosity changes with time, that leads to the suppression of nucleation and growth of crystals in a magmatic liquid. Another critical factor is the initial value of melt viscosity when degassing (or cooling) begins. For example, it is well known that if two melts with different initial viscosity values (e.g., rhyolite and basalt) are both cooled over a range of rates, the melt with a higher initial melt viscosity will quench to a glass at a slower cooling rate than the melt with the lower melt viscosity. Therefore, in order to fully explore the effect of degassing rate on the suppression of plagioclase crystallization, it is necessary to monitor melt viscosity throughout the decompression experiments.

How increasing melt viscosity during rapid degassing leads to plagioclase suppression

The melt viscosities of the phase equilibrium experiments are shown in Table 4.4 and calculated from the viscosity model of Hui & Zhang (2007). The change in melt water concentration with decreasing $P_{\text{H}_2\text{O}}$ is calculated from the water solubility model of Liu *et al.* (2005). In MLV-36, plagioclase spans a range in composition from An₃₃-An₅₃ (Fig. 4.2b), which approximately corresponds to a drop in pressure (at 850°C) from ~100 MPa (An₅₀) to ~80 MPa (An₃₆), a change in dissolved melt H₂O content from 4.0 wt% to 3.5 wt%, and a change in melt viscosity from 4.55 to 4.85 log₁₀ Pa s, respectively. There is abundant evidence that crystal growth may occur at viscosities >4.85 log₁₀ Pa s, such as the low pressure experiments from this study on MLV-44 between 30-100 MPa or the low pressure experiments of Brugger & Hammer (2010), which crystallize plagioclase in an H₂O-saturated rhyolite liquid at viscosities as high as 7.34 log₁₀ Pa s (at 860°C and 5 MPa). Therefore, decompression rate must exert control over plagioclase nucleation and growth, by rapidly increasing melt viscosity and reducing melt component diffusivity. To

establish the role of decompression rate, or the rate of change in viscosity, on plagioclase nucleation and growth, the results of Martel & Schmidt (2003) are utilized in addition to results presented here.

The range of plagioclase in MLV-36 (Fig. 4.2) was grown over a range of melt H₂O contents (4.0-3.5 wt%) and viscosities (4.55-4.85 log₁₀ Pa s) and is readily compared to the high-pressure, multistep decompression experiments of Martel & Schmidt (2003). The isothermal (860°C) decompression experiments (shown in Fig. 4.9) are conducted over a fixed range of pressure (150-50 MPa), which corresponds to a range of H₂O contents (4.8-2.6 wt%), a range of plagioclase compositions (An₅₃-An₃₇) and a range of melt viscosities (4.20-5.28 log₁₀ Pa s), with rates ranging from 0.12-27,000 MPa/hr. The unusually rapid decompression rates correspond to experiments of Martel and Schmidt (2003) where pressures of experiments were dropped in steps of >100 MPa in time intervals of seconds. In multistep decompressions, pressure is dropped from an initial pressure (P_i) to a final pressure (P_f) in a series of effectively instantaneous pressure steps at regular time intervals, which results in an integrated decompression rate (Fig. 4.9). To adjust the decompression rate, the time between pressure step is varied. The decompression experiments of Martel & Schmidt (2003) have accompanying phase equilibrium experiments that provide the equilibrium plagioclase compositions at various pressures at the decompression run temperature. The data in Martel & Schmidt (2003) can be used to evaluate the effect of viscosity on crystal growth and nucleation rate because they report run temperatures, P_i, P_f, experiment duration, pressure step interval, melt composition, and the range of plagioclase compositions grown during decompression. By comparing the range of plagioclase compositions grown during a

decompression experiment to the range of plagioclase compositions predicted to grow based on phase equilibrium experiments over the same interval of pressure, any possible suppression of plagioclase growth can be identified.

The decompression experiments of Martel & Schmidt (2003) are evaluated with respect to their decompression rates (MPa/hr) and as a function of change in viscosity with time (\log_{10} Pa s/hr) (Fig. 4.9). Pressure steps where plagioclase crystallized (shown in light grey) are identified by comparing the range of plagioclase compositions grown in the decompression experiments with the plagioclase composition grown in phase equilibrium experiments. The pressure step that corresponds to the most sodic plagioclase reported is shown in grey with a black outline. Pressure steps where plagioclase is predicted to grow but is not observed based on the reported compositions are shown in black. In Fig. 4.9, experiments that crystallized the widest range of plagioclase compositions (mostly grey) are decompressed at slower rates. A second observation from Fig. 4.9 is that as decompression rate increases, or as rate of change of viscosity increases, plagioclase growth stops at higher pressures and lower viscosities.

Ideally, the decompression experiments of Martel & Schmidt (2003) could be used to estimate decompression rates of natural samples using the viscosity at which plagioclase nucleation and growth ceased. For example, two decompression experiments at 0.72 (experiment #D4) and 0.12 MPa/hr (experiment #D3) feature suppression of plagioclase crystallization at viscosities of 4.65 and 4.90 \log_{10} Pa s, respectively, which bound the viscosity at which plagioclase crystallization ceased in MLV-36 (the natural sample) (4.85 \log_{10} Pa s; Table 4.4). However, it is known from the decompression experiments that plagioclase in MLV-36 ceases at rates between 2.9 and 0.8 MPa/hr. The

discrepancy between the rates from the decompression experiments on MLV-36 and those bracketed by experiments D3 and D4 from Fig. 4.9 is likely due to the evaluation of the experiments of Martel & Schmidt (2003) in the context of decompression rate (MPa/hr) instead of the change in melt viscosity (\log_{10} Pa s/hr).

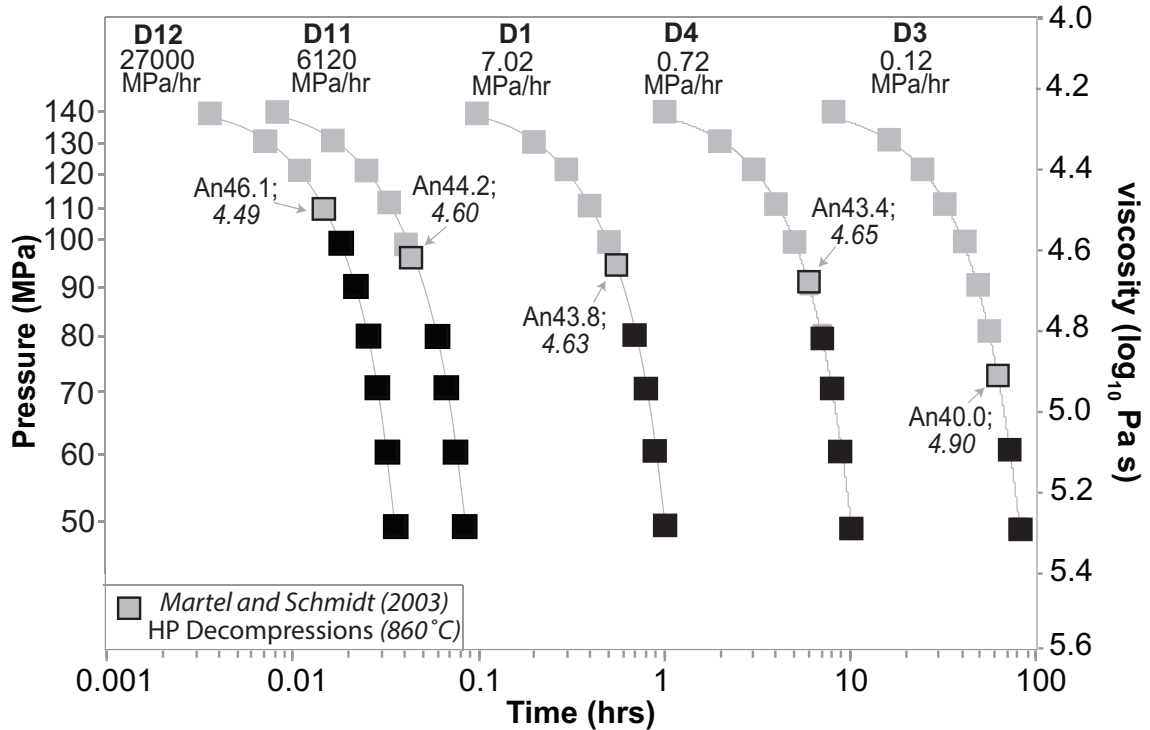


Figure 4.9: The high pressure decompression experiments of Martel & Schmidt (2003) are shown as a function of pressure (MPa) v. time (hours) and viscosity (\log_{10} Pa s) v. time (hours). Time is shown as a log scale so that experiments can easily be distinguished from each other. The experiment names (e.g. D12) as Martel & Schmidt (2003) report them are listed above each decompression path along with the corresponding rate. The pressure steps in the experiments that grew plagioclase, as indicated by the reported range of plagioclase compositions, are shown in grey. The pressure step corresponding to the most sodic plagioclase measured in the experiments is shown as a grey square with a bold black outline. Pressure steps that did not grow plagioclase are shown in black. As rate increases, plagioclase stops growing at higher pressures.

In Fig. 4.10, the pressures of the different experiments (i.e., D3, D4, etc; Fig. 4.9) that correspond to the suppression of plagioclase nucleation and growth (outlined in black) are shown as a function of their experimental viscosity (\log_{10} Pa s) and the rate of change of viscosity (\log_{10} Pa s/hr). There is an exponential relationship between the rate

of change of viscosity and the melt viscosity at which plagioclase nucleation and growth ceases. As the rate of change of viscosity increases (i.e., as decompression rate increases) in Fig. 4.10, the viscosity corresponding to the suppression of plagioclase crystallization decreases (i.e., lower viscosities, higher P_{H_2O}). The relationship between decompression rate, as a function of rate of change of viscosity, and the viscosity at which plagioclase crystallization ceases provide a basis for a speedometer.

Plagioclase Speedometry

In Fig. 4.10, the viscosity at which plagioclase growth ceases decreases as the rate of change of viscosity increases. The curve shown in Fig. 4.10 can be used to calculate the rate of change of viscosity that corresponds to the cessation of plagioclase growth. In the case of MLV-36, plagioclase stopped crystalizing at a viscosity of $4.85 \log_{10} \text{ Pa s}$, which corresponds to a rate of change of viscosity ($\Delta\eta/\Delta t$) of $0.03 \log_{10} \text{ Pa s/hr}$, based on the equation in Fig. 4.10. Once $\Delta\eta/\Delta t$ is obtained, a time may be calculated corresponding to the range of viscosity ($\Delta\eta$) over which plagioclase crystallized in the sample. For example, plagioclase began crystallizing in MLV-36 at an initial viscosity of $4.55 \log_{10} \text{ Pa s}$ and ceased at a final viscosity $4.85 \log_{10} \text{ Pa s}$, which corresponds to a $\Delta\eta$ value of $0.3 \log_{10} \text{ Pa s}$. The change in viscosity corresponding to plagioclase crystallization ($\Delta\eta$) and the rate of change in viscosity ($\Delta\eta/\Delta t$) can be used to calculate a time scale (Δt) over which plagioclase crystallized. Returning to MLV-36, the $\Delta\eta$ value of $0.3 \log_{10} \text{ Pa s}$ and the $\Delta\eta/\Delta t$ value of $0.03 \log_{10} \text{ Pa s/hr}$ result in a time of 11.25 hours over which plagioclase in MLV-36 crystallized. Plagioclase in MLV-36 crystallized over a change in P_{H_2O} from ~ 100 to $\sim 80 \text{ MPa}$. With a known time of 11.25 hours, the average decompression rate for the duration of plagioclase crystallization in MLV-36 can be

calculated (20 MPa/11.25 hours) and is 1.80 MPa/hr, under pure H₂O fluid saturated conditions, which is in good agreement with the decompression experiments conducted in this study at 2.9 MPa/hr and 0.8 MPa/hr. These decompression rates, however, are based on pure H₂O fluid saturation, and it is expected that at least some CO₂ was present in these magmas, which would indicate a mixed H₂O-CO₂ fluid phase during degassing. The addition of CO₂ to the system shifts all mineral-liquid equilibria to higher total pressures and therefore the decompression rates inferred for the natural samples are faster than those calculated here.

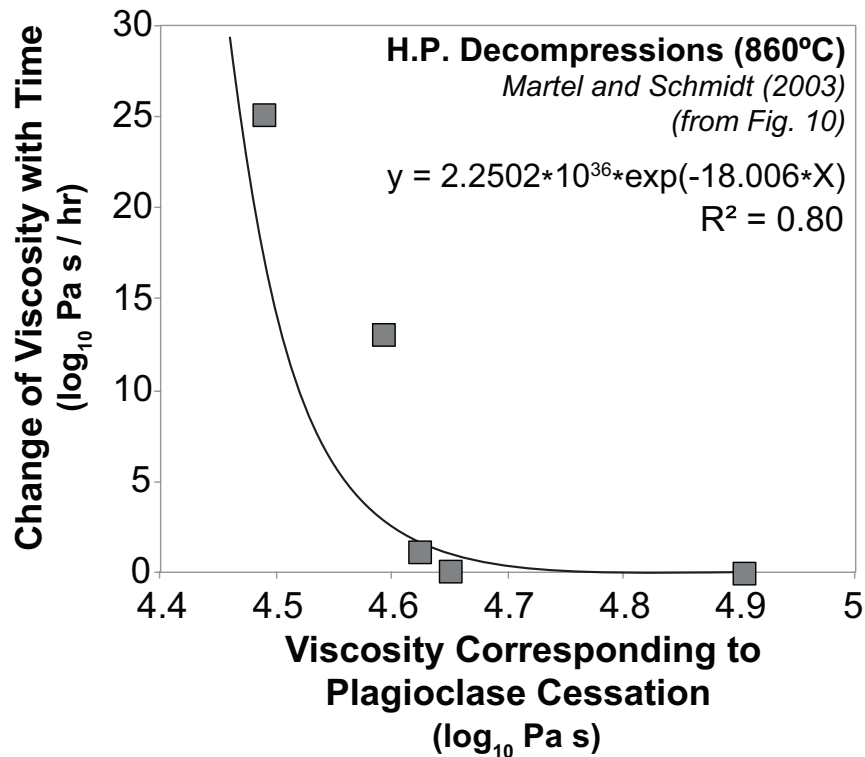


Figure 4.10: The experiments of Martel & Schmidt (2003) that correspond to the suppression of plagioclase nucleation and growth (outlined in black in Fig. 10) are shown as a function of their experimental viscosity (\log_{10} Pa s) and the rate of change of viscosity (\log_{10} Pa s/hr). There is an exponential correlation between the rate of change of viscosity and the viscosity at which plagioclase growth ceases.

5.6 CONCLUSIONS

Several key conclusions can be drawn from the experiments on three obsidian samples (67, 73 and 75 wt% SiO₂) performed in this study. First and foremost, the phase-equilibrium results clearly demonstrate that the wide compositional range (≤ 38 mol% An) of plagioclase crystals in the three crystal-poor ($< 3\%$) obsidian samples are all plausible phenocrysts. These experimental data further demonstrate that remarkably small variations in temperature (≤ 50 °C) and/or $P_{\text{H}_2\text{O}}$ (≤ 50 MPa) can lead to large changes in plagioclase compositions (> 10 mol%). Second, the decompression experiments under fluid-saturated conditions show that at a decompression rate of 0.8 MPa($P_{\text{H}_2\text{O}}$)/hr, a continuum of changing *equilibrium* plagioclase compositions crystallized from the melt as degassing progressed. Moreover, these plagioclase crystals often display diffusion-limited, rapid growth textures (swallowtail and skeletal), owing to the large undercooling that develops during degassing. The occurrence of diffusion-limited growth textures on plagioclase crystals with equilibrium compositions implies that crystals with these rapid-growth textures in natural samples cannot be assumed to represent disequilibrium compositions. Third, the degassing experiments performed at the rapid rate of 2.9 MPa($P_{\text{H}_2\text{O}}$)/hr, led to experimental run products with 100% glass. It is inferred that it is the rapid increase in melt viscosity (and decrease in chemical diffusivity) that accompanies rapid loss of dissolved water during degassing that leads to the suppression of plagioclase nucleation and growth, similar to the effects of rapid cooling. By comparing the data from this experimental study with those from the literature, the degassing rate at which plagioclase nucleation is suppressed is found to be a function of the initial viscosity of the melt phase. Melts with higher initial viscosities

require lower degassing rates in order to quench to a glass, which is probably why most obsidian samples are rhyolitic in composition. The relationship between melt viscosity and degassing rate is used to develop a plagioclase speedometer that is applicable to rhyolite. Finally, it is concluded that a wide compositional range (≤ 38 mol% An) of plagioclase in obsidian samples that contain fewer than 3% plagioclase overall can only have formed by degassing-induced crystallization. Conductive cooling of magma in a crustal chamber is far too slow to explain such a wide compositional range, combined with such a low overall plagioclase abundance.

4.7 REFERENCES

- Andrews B.J. & Gardner J.E. (2010) Effects of caldera collapse on magma decompression rate: An example from the 1800 ^{14}C yr BP eruption of Ksudach Volcano, Kamchatka, Russia. *Journal of Volcanology and Geothermal Research* 198, 205-216
- Bacon, C.R. & Hirschman, M.M. (1988) Mg/Mn partitioning as a test for equilibrium between coexisting Fe-Ti oxides. *American Mineralogist* 73, 57-61
- Baker, D.R. & Watson, E.B. (1988) Diffusion of major and trace elements in compositionally complex Cl- and F-bearing silicate melts. *Journal of Non-Crystalline Solids* 102, 62-70
- Baker, D.R. (1991) Interdiffusion of hydrous dacitic and rhyolitic melts and the efficacy of rhyolite contamination of dacitic enclaves. *Contributions to Mineralogy and Petrology* 1-6, 462-473
- Blundy, J. & Cashman, K. (2001) Ascent-driven crystallisation of dacite magmas at Mount St Helens, 1980–1986. *Contributions to Mineralogy and Petrology* 140, 631-650
- Blundy, J. & Cashman, K. (2005) Rapid decompression-driven crystallization recorded by melt inclusions from Mount St. Helens volcano. *Geology* 33, 793-796

- Brugger & Hammer, J.E. (2010) Crystallization kinetics in continuous decompression experiments: implications for interpreting natural magma ascent processes. *Journal of Petrology* 51, 1941-1965
- Carmichael, I.S.E. (1977) High-Temperature Properties of Silicate Liquids: Applications to the Equilibration and Ascent of Basic Magma. *Philosophical transactions of the Royal Society of London. Series A: Mathematical, physical, and engineering sciences* 286, 373-431
- Cashman, K.V. (1992) Groundmass crystallization of Mount St Helens dacite, 1980-1986 - a tool for interpreting shallow magmatic processes. *Contributions to Mineralogy and Petrology* 109, 431-449
- Castro, A., (2001) Plagioclase morphologies in assimilation experiments: Implications for disequilibrium melting in the generation of granodiorite rocks. *Mineralogy and Petrology*, 71:31-49.
- Chase, M.W. (1998) NIST-JANAF thermochemical tables, fourth edition. *J Phys Chem Ref Data*, Monograph Springer: Heidelberg 9
- Couch, S., Harford, C.L., Sparks, R.S.J., Carroll M.R. (2003a) Experimental constraints on the conditions of formation of highly calcic plagioclase microlites at the Soufriere Hills Volcano, Montserrat. *J Petrol* 44: 1455-1475
- Couch, S., Sparks, R.S.J., Carroll, M.R. (2003b) The kinetics of degassing-induced crystallization at Soufriere Hills Volcano, Montserrat. *J Petrol* 44:1477-1502
- Crabtree S.M., & Lange R.A. (2011) Complex Phenocryst Textures and Zoning Patterns in Andesites and Dacites: Evidence of Degassing-Induced Rapid Crystallization? *J Petrol* 52:3-38
- Donnelly-Nolan, J.M., Grove, T.L., Lanphere, M.A., Champion, D. E., Ramsey, D.W. (2008) Eruptive history and tectonic setting of Medicine Lake Volcano, a large rear-arc volcano in the southern Cascades. *Journal of Volcanology and Geothermal Research* 177, 313-328
- Frey H.M., & Lange R.A. (2011) Phenocryst complexity in andesites and dacites from the Tequila volcanic field, Mexico: resolving the effects of degassing vs. magma mixing. *Contrib Mineral Petrol* 162, 415-445
- Gardner, J.E., Rutherford, M., Carey, S., & Sigurdsson, J. (1995) Experimental constraints on pre-eruptive water contents and changing magma storage prior to explosive eruptions of mount St Helens volcano. *Bulletin of Volcanology* 57, 1-17

- Gardner, J.E., Hilton, M., & Carrol, M.R. (1999) Experimental constraints on degassing of magma: isothermal bubble growth during continuous decompression from high pressure. *Earth and Planetary Science Letters* 168, 201–218
- Gardner, J.E. & Castro, J.M. (2008) Did magma ascent rate control the explosive-effusive transition at the Inyo volcanic chain, California? *Geology* 36, 279-282
- Geshwind, C.H. & Rutherford, M. (1992) Cummingtonite and the evolution of the Mount St. Helens (Washington) magma system: An experimental study. *Geology* 20, 1011-1014
- Geshwind, C.H. & Rutherford, M. (1995) Crystallization of microlites during magma ascent: the fluid mechanics of 1980–1986 eruptions at Mount St Helens. *Bulletin of Volcanology* 57, 356-370
- Ghiorso, M., & Evans, B.W. (2008) Thermodynamics of rhombohedral oxide solid solutions and a revision of the Fe-Ti two-oxide geothermometer and oxygen barometer. *Am J Sci* 308, 957-1039
- Grose, T.L.T., Saucedo, G.J., & Wagner, D.L., (1989) The Walker Lane in Northeastern California. *Eos* 70, 1362
- Hammer, J.E., Cashman, K.V., Hoblitt, R.P., & Newman, S. (1999) Degassing and microlite crystallization during pre-climactic events of the 1991 eruption of Mt. Pinatubo, Philippines. *Bulletin of Volcanology*. 60, 355-380
- Hammer J.E. & Rutherford M.J. (2002) An experimental study of the kinetics of decompression-induced crystallization in silicic melt. *J Geophys Res* 107(B1): 2021
- Hui, N. & Zhang, Y. (2007) Toward a general viscosity equation for natural anhydrous and hydrous silicate melts. *Geochimica et Cosmochimica Acta* 71, 403-416
- Kohn S. C., Dupree R. & Smith M. E. (1989) A multinuclear magnetic resonance study of the structure of hydrous albite glasses. *Geochimica et Cosmochimica Acta* 53, 2925–2935.
- Lange R.A., Frey H.M. & Hector J. (2009) A thermodynamic model for the plagioclase-liquid hygrometer/thermometer. *Am Mineral* 94:494-506
- Larsen, J.F. (2005) Experimental study of plagioclase rim growth around anorthite seed crystals in rhyodacitic melt. *American Mineralogist* 90, 417-427
- Larsen, J.F. (2006) Rhyodacite magma storage conditions prior to the 3430 yBP caldera-forming eruption of Aniakchak volcano, Alaska. *Contributions to Mineralogy and Petrology*. 152, 523-540

- Lewis-Kenedi, C. B., Lange, R. A., Hall, C. M. & Delgado Granados, H. (2005). The eruptive history of the Tequila volcanic field, western Mexico. *Bulletin of Volcanology* 67, 391-414
- Liu Y, Zhang Y, Behrens H (2005) Solubility of H₂O in rhyolitic melts at low pressure and a new empirical model for mixed H₂O CO₂ solubility in rhyolitic melts. *Journal of Volcanology and Geothermal Research* 143, 219-235
- Loomis T.P. (1981) An investigation of disequilibrium growth processes of plagioclase in the system anorthite-albite-water by methods of numerical simulation. *Contributions Mineralogy Petrology* 81, 230-239
- Luhr, J.F. (1990) Experimental phase relations of water- and sulfur-saturated arc magmas and the 1982 eruptions of El Chichón volcano. *Journal of Petrology*, 31, 1071-1114
- Martel, C. & Schmidt, B.C. (2003) Decompression experiments as an insight into ascent rates of silicic magmas. *Contrib Mineral Petrol* 144, 397-415
- Martel, C. (2006) Basalt-inherited microlites in silicic magmas: Evidence from Mount Pelée (Martinique, French West Indies). *Geology* 34, 905-908
- Martel, C. (2012) Eruption dynamics inferred from microlite crystallization experiments: Application to Plinian and dome-forming eruptions of Mt Pelée (Martinique, Lesser Antilles). *Journal of Petrology* 53, 699-725
- Morse, S.A. & Nolan, K.M. (1984) Origin of strongly reversed rims on plagioclase in cumulates. *Earth and Planetary Science Letters* 68, 485-498
- Nakamura, M. & Shimakita, S. (1998). Dissolution origin and syn-entrapment compositional change of melt inclusion in plagioclase. *Earth and Planetary Science Letters* 161, 119-133
- Ni H. & Zhang Y. (2008) H₂O diffusion models in rhyolitic melt with new high pressure data. *Chemical Geology* 250, 68–78
- Ni, H., Xu, Z. & Zhang, Y. (2013) Hydroxyl and molecular H₂O diffusivity in a haploandesitic melt. *Geochimica et al Cosmochimica Acta*. 103, 36-48
- Ownby, S.E., Lange, R.A., Hall, C.M., and Delgado-Granados, H. (2011) Origin of andesite in the deep crust and eruption rates in the Tancitaro-Nueva Italia region of the central Mexican arc. *GSA Bulletin*. 123, 274-294
- Perugini, D., Busá, T., Poli, G., & Nazzareni, S. (2003) The role of chaotic dynamics and flow fields in the development of disequilibrium textures in volcanic rocks. *Journal of Petrology*. 44, 733-756
- Stolper, E. (1982a) The speciation of water in silicate melts. *Geochemica et Cosmochimica Acta* 46, 2609-2620

- Stolper, E. (1982b) Water in silicate-glasses-an infrared spectroscopic study. *Contribution to Mineralogy and Petrology* 81, 1-17
- Tomiyama, A., Takahashi, E., Furukawa, N., & Suzuki, T. (2010) Depth and Evolution of a Silicic Magma Chamber: Melting Experiments on a Low-K Rhyolite from Usu Volcano, Japan. *Journal of Petrology* 51, 1333-1354
- Venzky, D.Y. & Rutherford, M.J. (1999) Petrology and Fe-Ti oxide reequilibration of the 1991 Mount Unzen mixed magma. *Journal of Volcanology and Geothermal Research* 89, 213-230
- Waters, L.E. & Lange, R.A. (2013) Crystal-poor, multiply saturated rhyolite (obsidians) from the Cascade and Mexican arcs: Evidence of degassing-induced crystallization of phenocrysts. *Contributions to Mineralogy and Petrology*
- Xue, X. & Kanzaki M. (2004) Dissolution mechanisms of water in depolymerized silicate melts: constraints from ^1H and ^{29}Si NMR spectroscopy and ab initio calculations. *Geochimica et Cosmochimica Acta* 68, 5027–5057.
- Zhang, Y. & Behrens, H. (2000) H_2O diffusion in rhyolitic melts and glasses. *Chemical Geology* 169, 243–262
- Zhang Y., Stolper E. M. & Wasserburg G. J. (1991) Diffusion of water in rhyolitic glasses. *Geochimica et Cosmochimica Acta* 55, 441-456
- Zhang Y., & Ni, H. (2010) Diffusion of H, C, and O components in Silicate Melts. *Reviews in Mineralogy and Geochemistry* 72, 171-225
- Zhang, Y., Ni, H., & Chen, Y. (2010) Diffusion Data in Silicate Melts. *Reviews in Mineralogy and Geochemistry* 72, 311-408